THERMAL CONDUCTIVITY AND SINTERING CHARACTERISTS OF PLASMA SPRAYED DYSPROSIA-YTTRIA-ZIRCONIA THERMAL BARRIER COATINGS

by

STEVEN YUAN JUN WANG

B.A.Sc., The University of British Columbia (Vancouver), 2003

A THESIS SUBMITTED IN PARTIAL FULFILLMENT OF
THE REQUIREMENT FOR THE DEGREE OF

MASTER OF APPLIED SCIENCE

in

THE FACULTY OF GRADUATE STUDIES

(Materials Engineering)

THE UNIVERSITY OF BRITISH COLUMBIA

(Vancouver)

April 7, 2009

Abstract

Yttria-stabilized zirconia has long been the favoured refractory material for demanding applications such as thermal barrier coatings on turbine components. Its low thermal conductivity, relatively high thermal expansion coefficient, and good fracture toughness are most useful parameters when acute thermal cycles are considered. In recent years however, the demand for higher turbine operating temperatures has led to novel and innovative research in improving the thermal conductivity and sintering resistance of thermal barrier coatings. Rare-earth doped zirconia, rare-earth zirconates, and lanthanum hexa-aluminate have all been proposed as candidate materials for the next generation of thermal barrier coatings. Drawn from research conducted during 2003-2005, this study focuses on dysprosia as a ternary dopant to yttria-stabilized zirconia, examining the relationship of dopant content with overall thermal conductivity and sintering behaviour under cyclic thermal loading between room temperature and 1100°C. Air plasma spray deposition technique was employed for coatings deposition. Based on existing published works, this study is prefaced with four hypotheses: 1. increasing levels of dysprosia would likely result in lower overall thermal conductivity; 2. best improvement occurs at about 10 mol% total dopant (Dy + Y); 3. addition of dysprosia is also likely to increase sintering resistance during thermal cycling, since Dy cation radius is larger than Zr; 4. higher dopant concentrations, between 10 mol% and 50 mol%, should increasingly lead to shorter coating life under thermal cycling. As-sprayed coating heat capacity, thermal diffusivity, and porosity were measured by differential scanning calorimetry, laser flash method, and image analyses, respectively. Post-cycle coating porosity levels were compared against data for as-sprayed coatings. A theoretical model for estimating the thermal conductivity of plasma sprayed zirconia coatings was derived and constructed from previous works by other researchers. Experimental data and theoretical model presented in this study offer positive confirmations for the hypotheses, with the exceptions that the greatest reduction in thermal conductivity was seen at 15 mol% total dopant and that increased levels of dysprosia did not result in continued reductions in thermal conductivity. Literature data suggests long range ordering of oxygen vacancies could be a contributing factor in this trend.

Table of Contents

List of Tables

List of Figures

List of Symbols and Abbreviations

f_A – absorption edge frequency

a^3 – average atomic volume

N_A – Avogadro's number

k_B – Boltzmann's constant

ρ – density

ω_D – Debye frequency

γ^2 – Grüneisen anharmonicity parameter

m – mass (of sample)

a_m^3 – molecular volume

h – Planck's constant

n – refractive index

μ – shear modulus

c_p – specific heat

σ – standard deviation

σ_{SB} – Stefan-Boltzmann's constant

λ – thermal conductivity

λ_l – wavelength

λ_{abs} – absorption wavelength

α – thermal diffusivity

$\overline{x_n}$ – mean value of sample lot n

AS – agglomerated and sintered type

APS – air plasma spray

DF – degree(s) of freedom

DSC – differential scanning calorimetry

DY-YSZ – dysprosia - yttria stabilized zirconia

EB-PVD – electron beam physical vapour deposition

EDS – energy dispersion spectroscopy

HOSP – hollow sphere type powder

ID – inner diameter

MW – molecular weight or mass

OD – outer diameter

PS – plasma spray

SEM – scanning electron microscope

TBC – thermal barrier coating

TGO – thermally grown oxide

YSZ – yttria stabilized zirconia

XRD – x-ray diffraction

Acknowledgements

The author would like to thank the following people, whose valuable assistance made this research possible:

Dr. Roger C. Reed and Dr. Tom Troczynski, for their continued support throughout this project, both financially and intellectually.

Dr. Ainul Akhtar, Rudy Cardeno, Ross McLeod, Carl Ng, and Serge Milaire, for all their work in setting up and maintaining the equipment used in this project at UBC AMPEL building.

Mary Mager and Dr. Mati Raudsepp (UBC EOSC), for their assistance with SEM and XRD, respectively.

Mario Lamontagne (NRC-IMI) and Dong-Il Shin, for their assistance with laser flash and DSC measurements.

Dr. Richard S. Bellows at Solar Turbines Inc. for his assistance in supplying CMSX-11B single crystal material for this research.

C. Donald Wilcox, S. Brent Dove, W. Doss McDavid, and David B. Greer at the Department of Dental Diagnostic Science at The University of Texas Health Science Center, San Antonio, Texas, for developing and providing ImageTool.

CHAPTER I – Introduction

Zirconia has been the subject of intense research for several decades now, mainly due to its impressive thermal, mechanical, electrical, and optical properties when doped with tri- or tetra-valent ions.[1,2,3,4] Many researchers found that these dopants stabilized the tetragonal and cubic phases of zirconia. In particular, yttria-stabilized zirconia (YSZ) has found wide use in fields such as thermal barrier coatings (TBCs) and solid oxide fuel cells (SOFCs).[5,6] Deposition techniques such as plasma spraying and electron beam assisted physical vapour deposition (EB-PVD) are widely used in the aviation industry. TBC systems generally consist of the substrate (Ni- or Co-alloys), a bond coat (some form of Pt-NiAl or MCrAlY, where M is Ni, Co, etc.), and a top coat (ZrO_2-based ceramic). Other additives and/or functionally-graded materials may be included, as per design requirements. The details of the TBC system and its historical development have been covered by Nicholls and will not be repeated here.[5] Since many factors affect the performance of TBCs, it is useful to define two major selection parameters upon which a novel material can be chosen for further study. Some of the factors include thermal conductivity, thermal expansion coefficient, coating stiffness, sintering rate, erosion rate, and oxygen diffusivity, all of which are dependent on microstructure and chemical composition. In particular, thermal conductivity can dictate engine efficiency and weight savings, while sintering rate, along with alumina growth at the bond coat-top coat boundary, primarily determine coating lifetime under cyclic thermal loading.[5,7] These two key attributes are further explored in section 2.3 and 2.4.

Recently, the demand in aero engine applications has been for higher performing ceramic coatings with lower thermal conductivities and improved thermal-cycling performance. Research in this area is novel and exciting. It promises to improve thermal conductivity and sintering behaviour of aero engine TBCs, which could lead to higher operating temperatures (e.g. peak operating temperature >1200°C). This would translate into definite cost savings for the aviation industry in terms of fuel consumption and maintenance. During the research period (2003-2005) undertaken in this study, rare-earth doped zirconia, rare-earth zirconates, and lanthanum hexaaluminate have been proposed as potential candidates in recent papers.[8,9,10] Dy_2O_3-Y_2O_3-ZrO_2, henceforth denoted as Dy-YSZ, was chosen for deposition, in this research, using air plasma spray (APS) with five (5) different compositions. Material selection was based on experimental data from literature and theoretical arguments, which are elaborated upon

further in section 2.3. The author proposes that, similar to other trivalent rare-earth dopants, increasing levels of Dy atoms introduces additional point defects and oxygen vacancies, thus reducing the bulk thermal conductivity. The author also expects that the greatest reduction in thermal conductivity to occur at about 10 mol% of total dopant, based on existing works by Zhu and Miller. Its larger mass and atomic radius, in comparison to Zr, also contributes to improving sintering resistance. Higher concentrations of Dy are expected to lead to decreased stability under cyclic thermal loading, which had been shown in other rare-earth TBC systems by Zhu and Miller.

In this work, Dy-YSZ feedstock, in the form of agglomerated and sintered powder, was examined and verified with EDS and XRD for chemistry and phase composition. Similar techniques were employed in evaluating the as-sprayed coatings, where loss of dysprosia during APS was a concern. Thermal diffusivity and heat capacity of as-sprayed coatings were measured by laser flash and differential scanning calorimetry (DSC), respectively. Porosity levels in as-sprayed coatings were measured utilizing image analysis software, and subsequently the thermal conductivities were calculated with a simple formula. Theoretical explanations and a comprehensive model for the observed thermal conductivity trend were derived and constructed from previous works by Paul G. Klemens, Kevin W. Schilichting, and James C. Maxwell.

Round bar specimens were coated with Dy-YSZ and thermally cycled between room temperature and 1100°C with (43) minute intervals, for up to seven (7) days. Visual observations of coatings were made immediately post-cycle, followed by porosity measurements by image analysis. Trends in coating performance and sintering resistance were then established.

CHAPTER II – Technical and Theoretical Background

Due to the number of technical and theoretical considerations required in the characterization of thermal conductivity and sintering resistance of Dy-YSZ TBCs, a review of crucial experimental techniques, literature data, and relevant heat transfer theories is presented in the following sections. Experimental techniques include plasma spray deposition method, the laser flash method for determining thermal diffusivity, differential scanning calorimetry for determining specific heat, and quantitative phase analysis by x-ray diffraction and Rietveld refinement. Literature review covers data for near-dense and porous TBC ceramics, as well as sintering and thermal cycling behaviour. A thermal conductivity prediction model is constructed from published literature, primarily based on the work of Paul G. Klemens. It considers the intrinsic thermal conductivity of zirconia, effects of point defects such as substitutional atoms and oxygen vacancies, effect of grain boundaries, effects of porosity and cracks, and the contribution from radiation.

2.1 Zirconia and Thermal Barrier Coatings in Aero Turbines

The operating temperature of gas-turbine engines has steadily increased since the 1970s, driven by the desire for higher thermal efficiency and lower emissions. The peak temperatures in modern jet engines approach 1200°C, and in land-based turbines where more aggressive environments are encountered, the temperatures are now around 900°C. This increase has been made possible by new materials, improved cooling designs, better manufacturing processes, and the adoption of corrosion-resistant and thermally-insulating coatings. For example, the nickel-based superalloys used in the hot sections of the jet turbine have progressed from having no internal cooling to being actively cooled without coatings, finally to being coated and cooled. The superalloy material was initially wrought and later replaced by cast, then directionally-solidified, and finally single-crystal alloys. Owing to rhenium additions and γ' phase optimizations, current fourth-generation single-crystal superalloys designed for jet engines can operate at about 1050°C but still requires a TBC system for insulation and protection from oxidation of the substrate. Conversely the demands on land-based turbines are quite different, where concern of corrosion due to contaminants in the fuel is paramount.[5]

TBC systems for jet engines generally consist of the substrate (Ni- or Co-alloys), a bond coat in the form of Pt-NiAl or MCrAlY, where M is Ni, Co, etc., and a top coat of zirconia-based ceramic (e.g. YSZ) that is in direct contact with combustion gasses. Other additives and/or functionally-graded materials may be included in the coating, as per design requirements. The functions of each component can be described as follows:[5]

- Substrate serves as the infrastructure; examples include turbine blades, guide vanes, nozzle, etc.
- Bond coat assists in adherence between the top coat and substrate, and prevents oxygen penetration; thickness is generally in the range of 100 μm.
- Top coat works in conjunction with the cooling system to form a through-thickness temperature gradient of up to 150°C; thickness is in the range of 150-250 μm.

The bond coat MCrAlY materials were developed while considering factors such as oxidation and ductility. Stabilized zirconia is favoured for the top coat since it has relatively high fracture toughness (in the order of 10 $MPa \cdot m^{0.5}$), high thermal expansion coefficient (up to 11 x 10^{-6} $°C^{-1}$), and low bulk thermal conductivity (1-3 $W \cdot m^{-1} \cdot K^{-1}$).[11] However, zirconia is a good conductor of oxygen at high temperatures. At temperatures above 900°C, a thin layer of alumina forms between bond coat and top coat, and in an ideal situation this thermally-grown oxide (TGO) would stop further oxidation. In reality, due to the thermal strains experienced by the substrate and coatings, continued growth of TGO occurs due to formation of cracks.[11] This phenomenon, combined with sintering of top coat during service, leads to the failure of TBCs by spallation, where the top coat cracks and is ejected from the bond coat.[11] Rapid oxidation of the bond coat will then be possible, resulting in an increase of exposed surface area and damage to the substrate.

There has been interest in rare-earth oxide doped zirconia for some time now, and a number of papers on this subject have been reviewed. A summary is available in section 2.3. The current research focuses on evaluating the possibilities for improving the thermal conductivity, cyclic thermal loading, and sintering resistance aspects of TBCs by using rare-earth oxide doped YSZ. Thus corrosion processes were not covered in detail. A NiCrAlY type bond coat was used in all experiments.

2.2 Thermal Spray

The two current favoured coating deposition techniques are plasma spray (air, shrouded, or vacuum) and electron-beam assisted physical vapour deposition (EB-PVD). EB-PVD is an atomistic process and produces a unique columnar structure in the coating, such that many through-thickness or transverse discontinuities exist. This microstructure is suitable for areas where higher strain is encountered, such as on turbine blades. However the columnar structure leads to higher thermal conductivities (~2x) than those found in typical plasma-sprayed TBCs.[5] The current research does not involve EB-PVD and instead concentrates on the plasma spray (PS) process.

Although the PS process inherently has relatively high variability when compared to EB-PVD, PS continues to be the principal deposition process for TBCs on stationary components. PS is a technique whereby a stream of gasses such as argon, nitrogen, and hydrogen is converted into plasma via the application of an electrical potential across a set of anodes and cathodes in the gun or torch. For example, the equipment used in this research is typically operated with amperage of 100-250A per cathode and total power output of 70-150kW. The material to be coated is fed into the plasma stream in the form of a powder, and the particles are accelerated to supersonic velocities toward the substrate. The process can be done in air, or the plasma stream can be shrouded by inert gasses, or the assembly can be sealed and evacuated. For materials which can be oxidized in air, such as metals, shrouded or vacuum PS is desired.[5] PS coatings generally consist of layers of solidified splats or pancake structures, which is a result of the enormous cooling rate found near the substrate surface (~10^{-6} ºC/s). The coating microstructure is laminar, contains voids, and features many discontinuities or micro-cracks parallel to the surface of substrate. Thus heat flow through the coating encounters numerous micro-defects, greatly reducing the thermal conductivity. For instance, the bulk zirconia thermal conductivity can be reduced by two-fold through APS. However, the lack of transverse cracks results in higher stiffness as compared to EB-PVD, and thus APS coatings are used on static and low-strain components.

2.3 Thermal Conductivity, Porosity, and Sintering Behaviour of TBCs

Generally, near-dense TBC ceramics have thermal conductivities of 1.0-2.0 $W \cdot m^{-1} \cdot K^{-1}$ over the temperature range of interest (see section 2.3.1). In comparison, thermal conductivities of porous TBC ceramics such as those deposited by plasma spray or EB-PVD are in the range of 0.5-1.3 $W \cdot m^{-1} \cdot K^{-1}$ for a reduction in the order of 50% or more (see section 2.3.2). For plasma sprayed coatings this is mostly attributed to the presence of both rounded pores as well as microcracks parallel to the substrate, however improper processing can lead to higher than expected thermal conductivity. When such porous ceramics are sintered, the zirconia-rare-earth binary systems act in a similar fashion to YSZ in that they densify to an appreciable degree. Zirconia with two or three trivalent dopants, however, appear to resist sintering rather well.

This literature review found that in order to reduce thermal conductivity and improve sintering resistance, it is useful to consider:[8,12]

1) Using substitutional dopants with large atomic mass and cation radius differences with respect to zirconium atoms
2) Binary zirconia-rare-earth systems may not be sufficient in achieving both objectives
3) Ternary or higher order zirconia-yttria-rare-earth systems are desirable

Data is lacking in the literature for plasma sprayed $(Gd,Nd,Dy)_2O_3$-Y_2O_3-ZrO_2 where thermal conductivity and sintering resistance are correlated with both microstructure and dopant concentration. Table 1 summarizes some parameters of interest for these materials.

The author proposes that further studies on thermal conductivity and sintering resistance be conducted on the Y_2O_3-Dy_2O_3-ZrO_2 system in the zirconia rich region. The higher atomic mass of Dy may lead to the formation of more immobile defects which are desirable under sintering conditions. More specifically, ZrO_2 with 5 mol% Y_2O_3 and 0-20 mol% of Dy_2O_3 would be an interesting area to examine. Oxygen vacancies are expected to play a role in reducing thermal conductivity. Higher levels of Dy_2O_3 would eventually lead to poorer performance under cyclical thermal load, as the ceramic becomes more brittle.

Table 1: Atomic parameters for Zr, Y, Dy, Gd, Nd

Element	Atomic Number	Ionic Radius (Shannon, 8-coordinated) [pm]	Atomic Mass	ΔM	ΔR
Zr	40	98	91.224	0	0
Dy	66	116.7	162.5	+71.28	+18.7
Gd	64	119.3	157.23	+66.01	+21.3
Nd	60	124.9	144.24	+53.02	+26.9
Y	39	115.9	88.906	-2.32	+17.9

2.3.1 Thermal Conductivity Data for Near-Dense TBC Ceramics

The near-dense ceramics were in the forms of sintered pellets and/or hot pressed parts.

Reference values of 3.0-2.3 $W \cdot m^{-1} \cdot K^{-1}$ at 25-700 ºC respectively were presented by Wu *et al.* for 100% dense 7wt% YSZ[9] (all thermal conductivity values henceforth in section 2.3.x will use the units $W \cdot m^{-1} \cdot K^{-1}$). Schlichting *et al.* reported 3.1-2.4 at 25-1000ºC for fully dense 3 mol% YSZ (5.36 wt%).[13] In another paper, these workers reported 1.75-2.0 between 23-1000ºC for dense 8 mol% YSZ (13.7 wt%).[14] For nanocrystalline 5.8 wt% YSZ, Raghavan *et al.* reported 2.8-2.5 between 100-1000ºC for 99% dense samples, 2.3-2.7 at 90% dense, and 1.0-1.6 at 63% dense.[15] In the same paper, they showed that 96% dense 8 wt% nanocrystalline YSZ has thermal conductivity values of 2.0-2.1 between 100-800ºC and 98% dense 15 wt% YSZ is at 2.0-2.15 in the same temperature range. In single crystal studies at room temperature, Bisson *et al.* found that the thermal conductivity is approximately 2.85 for 5 mol% YSZ, 2.2 for 10 mol%, 2.7 for 15 mol%, and 2.8 for 20 mol%.[16] In another single crystal study, Mévrel *et al.* found that 4.2 mol% YSZ has thermal conductivity in the range of 2.6-2.1 between 25-1100ºC, while 8.9 mol% YSZ is in the range of 1.9-2.0 in the same temperature range.[17]

For rare-earth zirconates, specifically $Gd_2Zr_2O_7$, Suresh *et al.* reported 1.8-1.4 at 700-1400K[18] at 90.5% dense, Wu *et al.* presented 2.0-1.6 at 25-700ºC respectively[9] for 96% dense samples, while Lehmann *et al.* showed that at 100-400ºC the thermal conductivities were 1.5-1.3 for >95% dense samples.[19] Thus the available data suggests that thermal conductivity for near-dense $Gd_2Zr_2O_7$ is about 2.0 at room temperature and as low as 1.3 at moderate temperatures. In these

same papers, Lehmann *et al.* showed that thermal conductivity for $La_2Zr_2O_7$ was 2.0-1.55 at 200-900ºC for >95% dense samples, and Suresh *et al.* reported 2.3-1.6 at 700-1400K at 91.6% dense. Also, Vassen *et al.* reported 2.0-1.5 at 200-900ºC for >95% dense samples.[20] For $Nd_2Zr_2O_7$, Lehmann *et al.* reported 1.4-1.25 at 25-800ºC while Wu *et al.* presented 2.1-1.6 at 25-600ºC for 94% dense samples. For ternary zirconates such as $La_{1.4}Gd_{0.6}Zr_2O_7$, Lehmann *et al.* reported 1.2-0.9 between 25-1200ºC. For $La_{1.7}Dy_{0.3}Zr_2O_7$, these workers presented values of 1.3-2.0 between 25-1200ºC, and for $La_{1.4}Nd_{0.6}Zr_2O_7$, 1.15-2.0 between 25-1200ºC. Therefore, it can be said with some certainty that near-dense rare-earth zirconates have thermal conductivity values of 0.9-2.0 in the temperature range of interest (room temperature to 1400ºC).

For zirconia-rich rare-earth-doped zirconia, Wu *et al.* showed in another paper that 10 mol% Gd_2O_3-ZrO_2 has values of 2.0-2.5 at 25-700ºC while 30 mol% Gd_2O_3-ZrO_2 is 1.4-1.5 at 25-700ºC.[21]

2.3.2 Thermal Conductivity Data for Porous TBC Ceramics

Porous TBC ceramics in this case refers to those deposited by plasma spray (PS) or electron-beam physical vapour deposition (EB-PVD), unless otherwise stated. One needs to be aware that although a porosity value may be given for TBC coatings, it is more difficult to ascertain what fraction of the overall porosity is composed of inter-lamellae cracks or spherical pores and therefore these values are not usually given.

Reference values of 0.8-1.0 for standard TBC materials such as PS 8 wt% YSZ at 250μm thick has been reported by Nicholls *et al.* and a Rolls-Royce patent.[22,23] Furthermore, Siegel and Spuckler referred to commonly used values of 0.8-1.0 for thermal conductivity of PS coatings.[24] Kulkarni *et al.* examined PS 7.33 wt% YSZ using agglomerated + sintered (AS) and hollow sphere (HOSP) type powders. In as-sprayed coatings, they found that AS at 18% porosity had thermal conductivity value of 0.9, while HOSP at 13% porosity was around 0.6. They attributed the difference to lower amount of inter-lamellae cracks in the AS coating.[25] Brandt *et al.* found that PS 7 wt% YSZ with 9% porosity had thermal conductivity value of around 1, and 20 wt% YSZ with 20% porosity was about 0.4.[26] Wang *et al.* examined PS 6-8 wt% YSZ using fused and crushed, HOSP, sol-gel, and sintered types of powders. They found that the as-sprayed

coatings had thermal conductivities of 0.9-1.0, except that coatings derived from HOSP had a lower value of 0.65.[27]

For $La_2Zr_2O_7$, Vassen *et al.* reported values of 1.0-1.3 at 1000ºC for 20% porous material and possibly lower for PS zirconates, however no values were given.[20] For 8-17% porous PS lanthanum hexaaluminates such as $LaMgAl_{11}O_{19}$, Friedrich *et al.* reported values of 1.2-2.0 at 100-1200ºC.[28] For zirconia-rich rare-earth-doped zirconia, Hamacha *et al.* calculated values of 3.3 and 3.8 at 600ºC for 9 wt% Dy_2O_3-ZrO_2 and 9 wt% Yb_2O_3-ZrO_2, respectively.[29] However these values are much higher than expected and the authors stated that they were "uncharacteristic". Excessively large powder sizes and poor melting were indicated as possible causes. In contrast, Zhu and Miller reported values of 0.5-1.1 at 1316ºC for 180-250 μm thick PS YSZ-(Nd,Gd)-Yb coatings.[8] Specific chemistries were not provided however the optimal total dopant concentration with regard to reducing thermal conductivity appeared to be 10 mol%. Matsumoto *et al.* reported thermal conductivity values of around 1 for PS 93% dense 4 mol% YSZ + 5 mol% La_2O_3 at room temperature.[30] Nicholls *et al.* showed that it was possible to reduce the thermal conductivity of EB-PVD YSZ to as low as 0.88 by doping with 4 mol% of Gd.[22] Zhu and Miller also reported values as low as 0.84 for EB-PVD YSZ-(Nd,Gd)-Yb coatings.[8] These results establish an upper limit for desired thermal conductivity of advanced PS TBC coatings, where values of less than 0.9 are needed to be competitive.

2.3.3 Sintering Efficiency of Oxides with Additives

The efficiency of additives in assisting the sintering of oxides can be written as per Luskin:[12]

$$K_{eff} = \frac{\Delta F'_{add}}{\Delta F'_{b}} \left(\frac{|\Delta r|}{r_b} \right)^{-1} \qquad (1)$$

where $\Delta F' = \frac{\Delta F}{mZr}$ and ΔF is the free energy of oxide formation, m is the number of metal atoms in the oxide, Z is the cation charge, r is the cation radius, $\frac{|\Delta r|}{r_b}$ is the fractional difference between solute and solvent cation radii. Therefore to reduce sintering rate a solute with lower $\Delta F'$ and larger cation radius is preferable (as is the case in thermal conductivity). Numerical

data is not as plentiful in the literature compared with thermal conductivity but some qualitative statements will be made in the following section.

2.3.4 Sintering and Thermal Cycling of TBC Ceramics

Since TBC coatings have porosities in the range of 10-20 vol%, it is expected that during service at 1100-1200ºC that some degree of sintering will occur. This leads to stiffening and, in conjunction with the growth of the alumina layer (TGO) between the top and bond coats, can increase the probability of coating failure due to spallation.[5,11]

Wang *et al.* thermal cycled PS 6-8 wt% YSZ coatings deposited using fused and crushed, HOSP, sol-gel, and sintered powders. The cycle hot time was 30 minutes at 1150ºC with 15 minute cool down time to room temperature, repeated 10 times. They found very little sintering activity with the respective before and after porosity values, as follows:[27]

	Fused & Crushed	HOSP	Sol-Gel	Sintered
Before	7.4%	10.8%	13.3%	14.1%
After	7.2%	11.9%	11.2%	14.4%

Unfortunately based on these results, one cannot make conclusive statements regarding the degree of sintering since some reported porosity levels increased after sintering, and is counter-intuitive.

Vassen *et al.* reported that porous $La_2Zr_2O_7$ of unknown initial porosity sintered only to 58-67% of theoretical density at 1600-1650ºC after "long dwell times".[20] This suggests that lanthanum zirconate resists sintering fairly well.

Gadow and Lischka showed that lanthanum hexaaluminates may have sinter shrinkage as little as 0.03% even after long times (~40 hours) at 1300ºC, compared with typical YSZ where sintering results in 15-20% shrinkage.[10]

For 9 wt% Dy_2O_3-ZrO_2 and 9wt% Yb_2O_3-ZrO_2, Hamacha *et al.* reported microcrack curing and formation of interlamellar contact after thermal cycling at 1100ºC. This is expected since these

binary systems are similar to YSZ. On the other hand, in the system PS 90 mol% Nd_2O_3-Y_2O_3-ZrO_2, Akopov claimed that while there was grain growth, the microcracked structure was retained even after 1000hr at 1000ºC.[31] Further, Zhu and Miller claimed that their PS 94 mol% YSZ-(Gd,Nd)-Yb coating was capable of surviving up to 300 cycles with maximum temperature of 1163ºC with little grain growth.[8] However higher dopant concentrations usually resulted in poorer performance (at 10 mol% total dopant the lifetime was reduced by 2/3). The thermal cycles used by Zhu and Miller involved 45 minute hot time and 15 minute cooling time in a tube furnace, and the failure criterion was having delamination or spallation regions greater than 20% of the total area. EB-PVD coatings in this case generally fared better as expected, due to their unique columnar structure.

2.4 Thermal Conductivity Theory for Porous Zirconia-based TBCs

Much theoretical investigation in this area has been carried out by Paul G. Klemens from the University of Connecticut and other workers. The following section summarizes the necessary background and equations for building a simple model to understand the thermal conductivity behaviour of stabilized zirconia where the total dopant concentration is at most 10 mol%. For concentrations of $10 < c < 50$ mol%, it is thought that the increased long-range ordering of oxygen vacancies reduces their scattering effectiveness and therefore raises the thermal conductivity.[16] Phonon theory cannot account for this effect and although they are not considered here, numerical methods such as molecular dynamics simulation can be employed for that purpose.

2.4.1 Intrinsic Thermal Conductivity of Dense Zirconia

When thermal conductivity is a result of energy transport by mobile carriers such as lattice waves with a range of frequencies ω (radian/s), then it can be expressed as:[32]

$$\lambda = \frac{1}{3}\int_0^{\omega_m} C(\omega) l(\omega) v d\omega \qquad (2)$$

where C is the vibrational volumetric specific heat ($J \cdot kg^{-1} \cdot K^{-1}$), l the mean free path (m), and v the velocity (m/s).

The types of interactions lattice waves can undergo include anharmonic energy transfer between groups of three waves, and scattering due to point defects, boundaries, and strain fields. In a solid where the basic structural unit has N atoms of varying mass, then lattice waves can be composed of optical and acoustic modes. Optical modes correspond to the movement of individual atoms with molecular groups, while acoustic modes refer to the motion of molecules. It is assumed that the high group velocities from molecular motion contribute the most to heat transport.[32] It is also assumed that the crystal structure is cubic. The Debye frequency for a monoatomic lattice, where the group velocity is assumed to be constant, is then:[21]

$$\omega_D^3 = \frac{6\pi^2 v^3}{a^3} \tag{3}$$

and

$$a^3 = \frac{MW}{N_A N \rho} \tag{4}$$

$$a_m^3 = a^3 N \tag{5}$$

where a_m^3 and a^3 are in m^3, MW is in kg, and ρ is in kg/m^3. For zirconia, MW is 0.1232 kg/mol, ρ is 5845 kg/m^3, and a^3 is 1.167×10^{-29} m^3.[16,17]

The vibrational volumetric specific heat, or the contribution from acoustic lattice waves to the specific heat per unit volume, can be expressed as follows where $\omega \leq \omega_m$:[33]

$$C(\omega) = \frac{9k_B}{a_m^3 \omega_m^3} \omega^2 \tag{6}$$

The mean free path of phonons is temperature dependent and can be reduced by imperfections in the lattice. The intrinsic reciprocal mean free path, in the limit of high temperatures, can be approximated as:[33]

$$\frac{1}{l_i(\omega, T)} = A\omega^2 T \approx \frac{2\gamma^2 k_B}{\mu a^3 v \omega_m} \omega^2 T \tag{7}$$

and the upper frequency limit of acoustic modes is:[32]

$$\omega_m = \omega_D N^{-1/3} \tag{8}$$

where γ^2 is in the range of 3.0 to 4.0 for most oxides.[21] Here μ and the group velocity are given by:

$$v = \sqrt{\frac{\mu}{\rho}} \tag{9}$$

For zirconia, μ can be taken as 53 GPa and thus v is 3011.24 m/s.[21]

If one uses the expressions for C and l_i, and integrating from 0 to ω_m, one finds that the intrinsic thermal conductivity is inversely proportional to absolute temperature:

$$\lambda_i = BT^{-1} = \frac{3\mu v^2}{2\gamma^2 \omega_D N^{2/3}} T^{-1} \tag{10}$$

However it has been shown that at elevated temperatures, the unit cell imposes a lower limit on the intrinsic thermal conductivity. Therefore, a temperature T_0 can be defined where the mean free path at ω_m reaches a lower limit l_0 :[21]

$$l_0 = \frac{a^3 BN}{3vT_0 k_B} \tag{11}$$

and at $T > T_0$, the intrinsic thermal conductivity becomes:

$$\lambda_{i,(\min)} = \chi \frac{3\mu v^2}{2\gamma^2 \omega_D N^{2/3}} \left[\frac{2}{3} \left(\frac{T_0}{T} \right)^{1/2} + \frac{T}{3T_0} \right] T^{-1} \tag{12}$$

Here χ is the data fit parameter used by Wu *et al*.

2.4.2 Point Defect Effects in Zirconia

In stabilized zirconia where the dopant metal ion is not tetravalent, point defects exist in the lattice in the forms of substitutional atoms, oxygen vacancies, and strain fields. When point defects are present in the lattice, they scatter phonons as the fourth power of frequency so that they contribute as:

$$\frac{1}{l_p(\omega)} = A\omega^4 \tag{13}$$

When added to the intrinsic reciprocal mean free path and defining $l_i(\omega_0, T) = l_p(\omega_0)$, l becomes:[34]

$$\frac{1}{l(\omega, T)} = \frac{1 + (\omega / \omega_0)^2}{l_i(\omega, T)} \tag{14}$$

After integrating from 0 to ω_m, one finds that the reduction of thermal conductivity due to point defects is:

$$\delta\lambda_{pd} = \lambda_i\left[1-\left(\frac{\omega_0}{\omega_m}\right)\tan^{-1}\left(\frac{\omega_m}{\omega_0}\right)\right] \tag{15}$$

and

$$\frac{\omega_0^2}{\omega_m^2} = \psi\frac{4\gamma^2 N k_B T}{3\pi\mu a^3} \tag{16}$$

Here ψ is the data fit parameter used by Wu *et al*.

For substitutional atoms of differing mass, one can write l_p as:[33]

$$\frac{1}{l_p(\omega)} = \frac{a^3\omega^4}{4\pi v^4}c\left(\frac{\Delta M}{\overline{M}}\right)^2 = A\omega^4 \tag{17}$$

where the term $c\left(\frac{\Delta M}{\overline{M}}\right)^2$ accounts for the difference in mass between the host atoms, impurity atoms, and oxygen vacancies (if applicable). For a ternary system where as an example, the trivalent dopants are yttria and dysprosia, one can write:

$$c\left(\frac{\Delta M}{\overline{M}}\right)^2 = x\left(\frac{\Delta M}{\overline{M}}\right)_{Dy}^2 + y\left(\frac{\Delta M}{\overline{M}}\right)_{Y}^2 + \left(\frac{x+y}{2}\right)\left(\frac{\Delta M_{Ovac}}{\overline{M}}\right)^2 \tag{18}$$

where x and y are dopant mole fractions, M is atomic mass, and $\overline{M}$ is the average atomic mass in a unit cell:

$$\overline{M} = \frac{\overline{M}_{cation} + (2-0.5x-0.5y)M_O}{3-0.5x-0.5y} \tag{19}$$

$$\overline{M}_{cation} = xM_{Dy} + yM_Y + (1-x-y)M_{Zr} \tag{20}$$

The other terms can be written as follows:

$$\left(\frac{\Delta M_{Ovac}}{\overline{M}}\right)^2 = \left(-2-\frac{M_O}{\overline{M}}\right)^2 \tag{21}$$

$$\left(\frac{\Delta M}{\overline{M}}\right)_{Dy}^2 = \left(\overline{M}\left(\frac{1}{M_{Dy}}-\frac{1}{M_{Zr}}\right)\right)^2 \tag{22}$$

$$\left(\frac{\Delta M}{\overline{M}}\right)_Y^2 = \left(\frac{M_Y - M_{Zr}}{\overline{M}}\right)^2 \tag{23}$$

Note that since Dy is more massive than Zr, it moves in resistance to the lattice.[21] Also the value of 2 appears in the term for oxygen vacancies since the number of bonds broken at vacancy sites is twice the number of bonds per atom. Consequently, the major contributing factor in the term $c\left(\frac{\Delta M}{\overline{M}}\right)^2$ is the presence of oxygen vacancies.

2.4.3 Extended Boundary Effects

For grain boundaries with a mean free path D, one can define ω_B such that $l_i(\omega_B, T) = D$ and find:[33]

$$\delta\lambda_{GB} = \lambda_i\left(\frac{\omega_B}{\omega_m}\right)\tan^{-1}\left(\frac{\omega_m}{\omega_B}\right) \tag{24}$$

$$\frac{\omega_B^2}{\omega_m^2} = \frac{\mu a^3 v}{2\gamma^2 k_B T \omega_m D} \tag{25}$$

2.4.4 Radiation Contribution to Thermal Conductivity in Zirconia

Radiation becomes important at high temperatures, and it has been reported that contribution from the radiative component of thermal conductivity is around 10% at 1250ºC.[22] Zirconia is transparent to frequencies below the absorption edge $f_A = \frac{k_B \Theta_A}{h}$ and absorbent to those above. Thus for a layer thickness L (m) and near-equilibrium conditions, one can write the radiative component of thermal conductivity as:[34]

$$\lambda_{R,dense} = \frac{4\sigma_{SB} n^2 L T^3}{J_4(\Theta_0 / T)} J_4(\Theta_A / T) \tag{26}$$

where J_4 is

$$J_4(Z) = \int_0^Z \frac{x^4 e^x}{\left(e^x - 1\right)^2} dx \tag{27}$$

and for very high frequencies,

$$J_4(\Theta_0 / T) = 25.9758 \tag{28}$$

Here Θ and T are in Kelvins. The J function has been tabulated and can be found in the Tables of Transport Integrals.[35] This description of the radiative component of thermal conductivity may not readily apply to operating conditions found in a turbine engine, where radiation passing through TBC may not attain equilibrium. However these equations most likely apply to thermal conductivity measurements using laser flash, where near-equilibrium conditions are expected.[32]

2.4.5 Effects of Porosity and Cracks on Thermal Conductivity

For spherical pores, approximations based on Maxwell's work have resulted in a couple of equations which give an maximum and minimum limit for the reduction of thermal conductivity due to porosity.[13,36] Firstly, Maxwell found for a spherical inclusion in a cube of unit volume:

$$\frac{\lambda_{mix}}{\lambda} = \frac{1 + 2\frac{\lambda}{\lambda_{inc}} - 2f\left(\frac{\lambda}{\lambda_{inc}} - 1\right)}{1 + 2\frac{\lambda}{\lambda_{inc}} + f\left(\frac{\lambda}{\lambda_{inc}} - 1\right)} \tag{29}$$

where f is the inclusion volume fraction. For pores containing air, $\frac{\lambda}{\lambda_{inc}} \to \infty$, thus:

$$\frac{\delta\lambda_{p,porous}}{\lambda_{p,dense}} \approx \frac{3}{2} f \tag{30}$$

In another treatment, Schilichting *et al.* arrived at:

$$\frac{\delta\lambda_{p,porous}}{\lambda_{p,dense}} = \frac{4}{3} f \tag{31}$$

When considering radiation, the presence of porosity reduces the dielectric constant (n^2) of the material. In a heterogeneous medium, the effective values of n^2 and λ are very much related. Thus for $n_{inc}^2 = 1$, Schilichting *et al.* gave a similar set of equations as to the two above for effects on radiative component of thermal conductivity:

$$\frac{\delta\lambda_{R,porous}}{\lambda_{R,dense}} \approx \frac{3}{2} f\left(\frac{n^2 - 1}{n^2 + 0.5}\right) \tag{32}$$

and

$$\frac{\delta\lambda_{R,porous}}{\lambda_{R,dense}} \approx f\frac{n^2-1}{n^2}\left(1+\frac{1}{3}\frac{n^2-1}{n^2}\right) \tag{33}$$

This work will consider the average value of $\delta\lambda_{R,porous}$ between these two equations above (32 and 33).

For non-spherical discontinuities such as cracks, a unidirectional heat flux derived model for short fibre composites can be used since it involves only the geometric shape and orientation of fibres.[37] H. Hatta and M. Taya found that in a 3D volume with completely random distribution of ellipsoidal fibres (or in this case representing cracks), the effective thermal conductivity is

$$\lambda_{cracks} = \lambda_m\left[1-\frac{f(\lambda_m-\lambda_{inc})[(\lambda_{inc}-\lambda_m)(2S_{33}-S_{11})+3\lambda_m]}{3(\lambda_{inc}-\lambda_m)^2(1-f)S_{11}S_{33}+\lambda_m(\lambda_{inc}-\lambda_m)R+3\lambda_m^2}\right] = \lambda_m\Pi \tag{34}$$

where λ_m and λ_{inc} are thermal conductivities of the matrix and inclusion, f is the volume fraction of inclusions, and

$$R = 3(S_{11}+S_{33})-f(2S_{11}+S_{33}) \tag{35}$$

If inter-splat cracks such as those found in PS zirconia can be assumed to be penny-shaped ellipsoids where a is the semiaxis and a_1 and a_2 lie perpendicular to the direction of heat flow, then:[37]

$$(a_1 = a_2) >> a_3 \tag{36}$$

$$S_{11} = S_{22} = \frac{\pi a_3}{4a_1} \tag{37}$$

$$S_{33} = 1-\frac{\pi a_3}{2a_1} \tag{38}$$

2.4.6 Overall Thermal Conductivity

Now it is possible to describe the overall thermal conductivity for cubic zirconia stabilized with non-tetravalent dopant metal ions of maximum total concentration of 10 mol%, thickness L, and grain size D. Firstly, from equations 30-33, the reduction in thermal conductivity due to spherical pores is

$$\delta\lambda_{pores} = \delta\lambda_{p,porous} + \delta\lambda_{R,porous} \tag{39}$$

Drawing upon equations 34-38, the reduction due to penny-shaped ellipsoidal cracks is

$$\delta\lambda_{cracks} = \lambda_{p,dense}(1-\Pi) \tag{40}$$

and for the fully dense material where only the intrinsic thermal conductivity and lattice defects are considered, equations 12 and 15-25 can be re-written as

$$\lambda_{p,dense} = \lambda_i - \delta\lambda_{pd} - \delta\lambda_{GB} \tag{41}$$

Finally, by including equations 26-28, the overall thermal conductivity is

$$\lambda = \lambda_{p,dense} + \lambda_R - \delta\lambda_{cracks} - \delta\lambda_{pores} \tag{42}$$

2.5 X-ray Diffraction and Rietveld Refinement

X-ray diffraction is a well-known technique which probes the crystal structures of materials. It takes advantage of the fact that x-ray wavelengths are in the range of 1-100 nm, essentially the same magnitude as interatomic spacing in crystalline materials. Thus crystal lattices serve as diffraction grates when subjected to incident x-rays, such as those produced when high energy electrons impact a target material (Cu, Mo, etc). Max von Laue and later William L. Bragg were leading figures in this field, and the practical Bragg's law describes the condition where constructive interference between atomic planes result in intense Bragg peaks in the diffraction pattern.

$$n\lambda_l = 2d\sin\theta \tag{43}$$

As the incident angle θ increases, the successive n-th ordered reflections from a Bragg plane (*h,k,l*) are *nh,nk,nl*. These Miller indices can also be combined with Bragg's law to produce selection rules for specific types of lattice structures, which gives allowed and forbidden reflections. In short, the Bragg peak positions relate directly to unit cell parameters, and peak intensities relate to atomic number (Z) and atomic arrangement.[38]

Since the early twentieth century, systematic analysis and recording of XRD data for thousands of crystals have enabled massive databases to be referenced at will. One example is the database organized by The International Centre for Diffraction Data (ICDD). Modern X-ray diffractometers are typically fully automated with computerized controls and access to ICDD,

allowing for data collection and analysis to be performed relatively quickly. Through peak comparison, assisted by software, one can identify the phases present in a sample. Further operations are then possible, such as quantitative phase analysis by Rietveld refinement.

With the identity of phases and their crystal structures available, the Rietveld method compares the experimental pattern to a calculated pattern which models individual peak shape and width, as well as background level. The difference or residual is then minimized through least-squares refinement:[38]

$$R = \sum \frac{\left(y_i - y_{ci}\right)^2}{y_i} \tag{44}$$

where y_i is the observed intensity at the i^{th} step and y_{ci} is the calculated intensity at the i^{th} step, summed over all data points. The relative mass fraction of each phase can then be estimated by:[38]

$$W_r = \frac{S_r \left(Z \cdot MW \cdot V\right)_r}{\sum S_t \left(Z \cdot MW \cdot V\right)_t} \tag{45}$$

where W_r is the relative mass fraction of phase r in a mixture of t phases, S is the scale factor derived from Rietveld refinement, Z is the number of formula units per unit cell and V is volume of unit cell ($Å^3$).

2.6 Laser Flash Method for Determining Thermal Diffusivity

The laser flash method has been widely used in determining thermal diffusivity of materials, including zirconia.[17,21] The basic principle is that the infrared detector aimed at the back surface of a sample will record a temperature rise after the front surface is illuminated with one laser pulse. Typically the sample is kept in an evacuated chamber, and certain configurations allow for cryogenic or high temperature conditions. Sample size can range from Ø6-25 mm (disc shape) and 0.02-4 mm thick. The laser pulse duration and energy, as well as the infrared detector signal, are now typically acquired and analyzed via software. YAG or CO_2 lasers are typically employed.

Assuming that the laser pulse fits the front surface of a disc sample uniformly and that the disc is an uniform cylinder, the resulting thermal gradient is one-dimensional. Assuming the sample is

not transparent in the range of laser frequency and does not lose heat, then the heat conduction solution under ideal conditions can be written as:[39,40]

$$\Delta T = \Delta T_m \left[1 + 2\sum_{n=1}^{\infty} (-1)^n \exp\left(\frac{-n^2 \pi^2 \alpha t}{L^2} \right) \right] \tag{46}$$

where L is sample thickness, ΔT is observed temperature rise, ΔT_m is maximum observed temperature, and t is time after pulse heating. By setting $\Delta T/\Delta T_m = 0.5 = t_{1/2}$, or the time taken for back surface temperature to rise to half of maximum value, the above solution can be simplified to the Parker equation:[41]

$$\alpha = \frac{0.139 L^2}{t_{1/2}} \tag{47}$$

Note that in this form, the thermal diffusivity is very sensitive to the sample thickness. For plasma sprayed coatings, which typically have rough surface finishes, the degree of error could be in the range of ±5-10%.

2.7 Differential Scanning Calorimetry for Determining Specific Heat

The DSC technique is practical for determining heat, transition temperatures, enthalpic recoveries, etc. DSC equipment can comprise of two (2) containers with controlled atmospheres, one of which serves as the baseline. A standard, such as sapphire, and then the sample are heated from an isothermal zone T_0, linearly, to a second isothermal zone T_1. From the baseline, the DSC signal between sample and standard can be compared to obtain the specific heat of interest. The evaluation of specific heat is relatively straightforward:[42]

$$c_p = \frac{1}{m} \frac{\partial H / \partial t}{\partial T / \partial t} \tag{48}$$

where $\partial T/\partial t$ is the heating rate and is a controlled parameter, and $\partial H/\partial t$ is the DSC signal. The precision of this technique is typically ±3%, and can be controlled to ±1% with good laboratory practice.

CHAPTER III – Experimental Setup and Methodology

3.1 Dysprosia-Yttria-Zirconia Powder

One (1) 25lb batch of 5 mol% Y_2O_3-ZrO_2 powder and four (4) 25lb batches of Dy-YSZ powders were received from Saint-Gobain Ceramic Materials (Worcester, MA, USA), and henceforth they will be labeled as 5YSZ, Dy-5, Dy-10, Dy-15, and Dy-20 based on their theoretical molar dopant content. The powders were of the agglomerated and sintered (AS) type with manufacturer's report showing that 90% of powder particle size is ≤109.3 μm. The mean sizes are between 54.21 and 69.91 μm, with Dy-15 having slightly larger sizes than any other grade of powder. Manufacturer's size distribution was determined by laser diffraction particle size analyzer Microtrac SRA-150 (Microtrac Inc., Montgomeryville, PA, USA), and the results are summarized in Table 3. AS powder is typically prepared by "spray-drying", i.e. injecting the slurry precursor (e.g. 15 vol% solids) against a stream of heated air (e.g. 150°C), where the liquid phase is mostly removed and the solids coalesce to form spherical powders (sometimes also elongated or pancake shapes). Individual powders at this point are still composed of discrete granules. The dried powders are then again heated at a low temperature (e.g. 250°C) to remove the binder and sintered at around 1050°C. Sufficient sintering time would allow mass transfer between granules to form solid powders.[43,44]

In order to confirm the chemical composition, a small amount of powder was randomly sampled from each grade and mounted using Cold Cure epoxy. Each mounted specimen was then polished to 3 μm using diamond solution on fine cloth until the powder was exposed sufficiently for SEM imaging. All samples were examined in SEM under variable pressure mode, which eliminates the need for an electrically conductive coating and greatly simplifies sample evaluation. SEM (Hitachi S-3000N, Rexdale, Ontario, Canada) and EDS/ZAF (Quartz XOne, Vancouver, BC, Canada) analyses parameters are summarized in Table 4 and representative SEM micrographs are shown in Figure 1. EDS data collection was conducted in area mode for bulk chemistries and at relatively low magnifications (70x – 120x). Areas with high concentration of powder particles were chosen, an example is shown in Figure 1 (Dy-10 at 120x). Minimum of (10) readings per sample at random locations were collected, and summarized EDS/ZAF findings are presented in Figure 2. Table 2 summarizes chemical compositions as reported by the manufacturer. The two major impurities were included for completeness.

The AS powder particles were composed of granules from sub-micron to <10 μm in size, and neck formation due to sintering are clearly visible. It appears that all grades of powder were in the partially sintered condition.

It was noted that Dy_2O_3 content in Dy-5 and Dy-20 powders differed from theoretical specification (the target) by >1 mol%. The precision of Dy_2O_3 content in Dy-15 and Dy-20 powders was considerably lower (>2x) than any other grade of powder. This could have been a result from production variability, because Dy-15 and Dy-20 were ordered in June 2004 while 5YSZ, Dy-5, and Dy-10 were ordered in March 2004.

All grades of powders were examined by XRD (Siemens Bruker AXS D5000 Diffractometer, Karlsruhe, Germany) to determine phases present. All samples were ground by hand into fine powder form (<10 μm) using a mortar and ethanol. Grinding time was approximately 30 minutes for each sample. Ethanol was then removed by using a heating lamp. The dried powder was manually packed into a plate-shaped sample holder containing a 2.0 x 2.4 x 0.1 cm cavity. The exposed surface was made as flat, texture-less, and smooth as humanly possible using glass slides. Parameters for XRD analyses are summarized in Table 5. Measured XRD spectra are shown in Figure 3.

Since no characteristic peaks for Y or Dy oxides were observed, but peak shift with increasing dopant concentration was observed, it can be concluded that all dopants are in solid solution with zirconia. Based on this knowledge, Rietveld refinement was performed on all spectra since there were only three (3) phases expected for zirconia: monoclinic, tetragonal, and cubic. The estimated phase distribution is shown in Table 6.

It was observed that the primary phases in all powders were cubic and monoclinic. Some literature data suggested that at least for $YO_{1.5}$+ZrO_2, where $YO_{1.5}$ mol% <57.14, the phases M+C are thermodynamically stable below 393°C.[45] The phase composition is expected to change after APS processing since powder melting will occur in the plasma plume.

Table 2: Powder manufacturer's chemical analyses versus analyses by SEM/EDS (ZAF)

Powder Type		Composition by SEM/EDS (ZAF)		Manufacturer's Analysis
		mol %	wt %	wt %
YSZ AG	Y_2O_3	5.31	9.32	9.05
	ZrO_2			88.2
	Dy_2O_3	0	0	0
	SiO_2			0.46
	Hf_2O_3			1.76
Dy-5	Y_2O_3	4.59	7.15	6.85
	ZrO_2			77.9
	Dy_2O_3	6.82	17.50	12.68
	SiO_2			0.40
	Hf_2O_3			1.61
Dy-10	Y_2O_3	4.76	6.99	6.98
	ZrO_2			67.35
	Dy_2O_3	10.26	24.85	23.44
	SiO_2			0.36
	Hf_2O_3			1.41
Dy-15	Y_2O_3	4.24	5.80	6.12
	ZrO_2			60.17
	Dy_2O_3	14.97	33.69	31.79
	SiO_2			0.31
	Hf_2O_3			1.24
Dy-20	Y_2O_3	5.14	6.75	6.68
	ZrO_2			51.98
	Dy_2O_3	17.37	37.73	39.66
	SiO_2			0.26
	Hf_2O_3			1.08

Table 3: Manufacturer's report on powder size distribution

Powder Type	Min Size (μm)	Max Size (μm)	Distribution	(μm)
YSZ AG	15	176	d10	26.78
			d50	54.61
			d90	92.84
			Mean	57.61
Dy-5	15	176	d10	27.08
			d50	53.21
			d90	90.00
			Mean	56.29
Dy-10	15	176	d10	32.19
			d50	64.94
			d90	102.40
			Mean	56.29
Dy-15	15	176	d10	28.63
			d50	69.48
			d90	109.30
			Mean	69.91
Dy-20	15	176	d10	16.60
			d50	53.22
			d90	91.79
			Mean	54.21

Table 4: SEM/EDS parameters

Operation Mode	Voltage (kV)	Working Distance (mm)	EDS Mode	EDS Live Time (s)	Equipment Relative Error (%)
Variable Pressure	20	15	Area	100	5

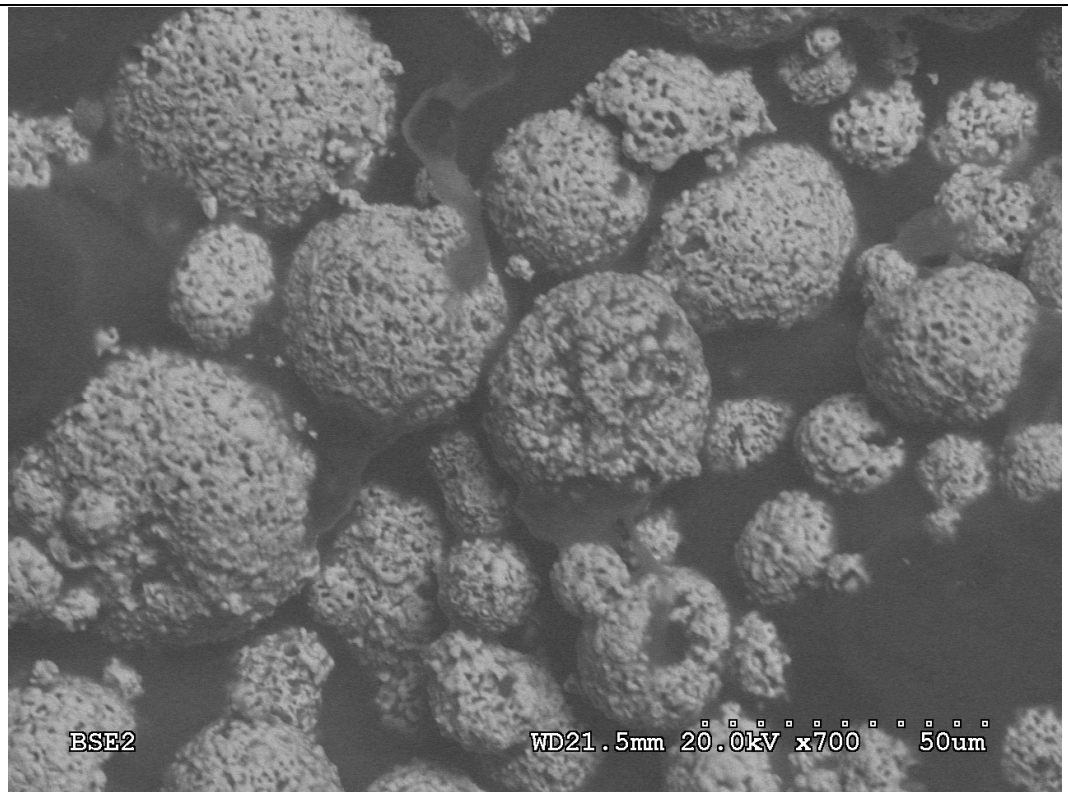

5YSZ

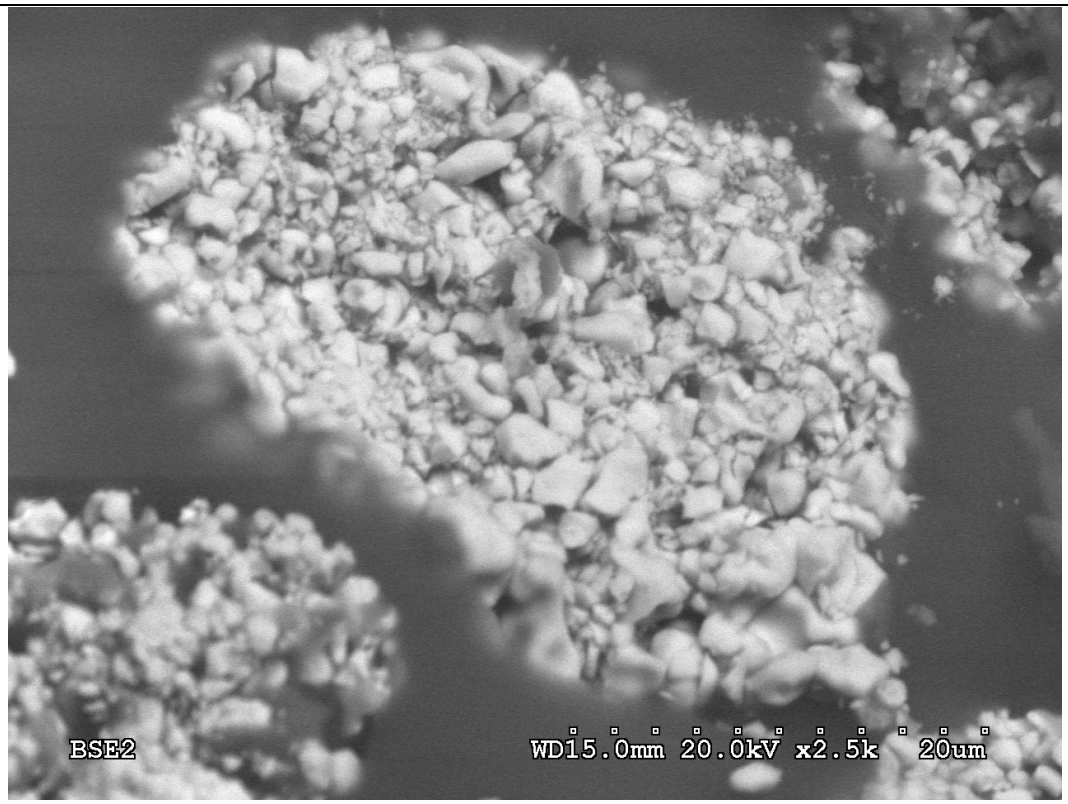

5YSZ

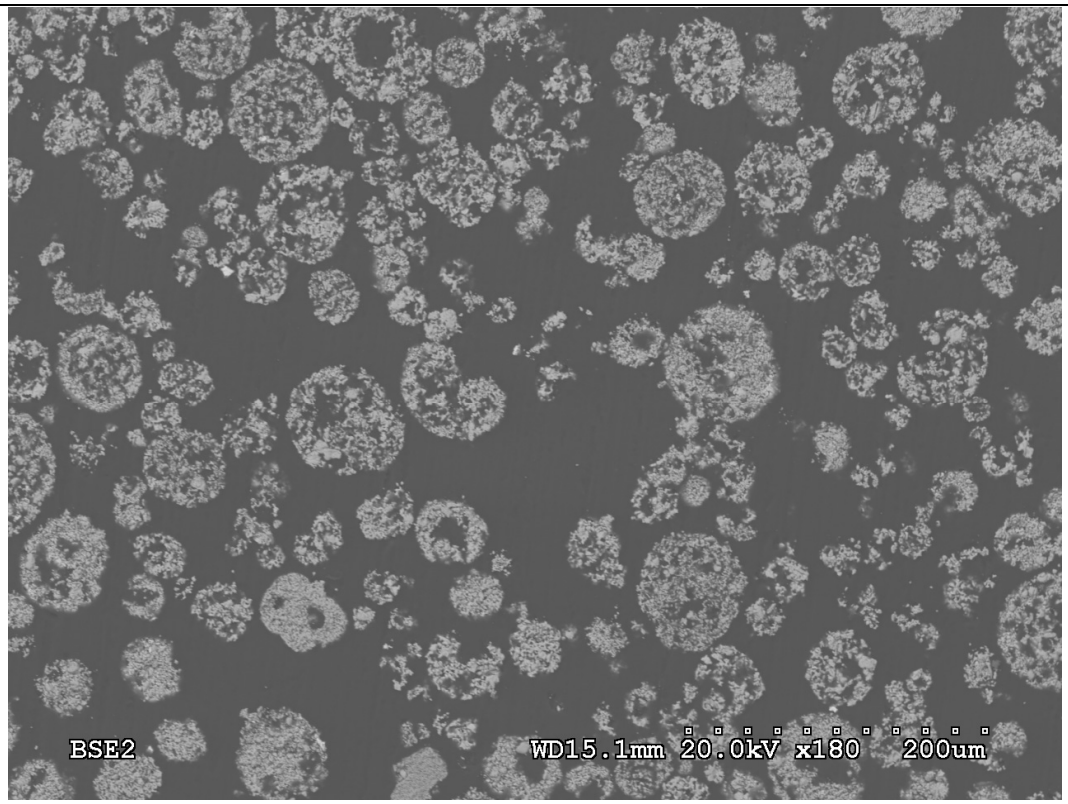

Dy-5

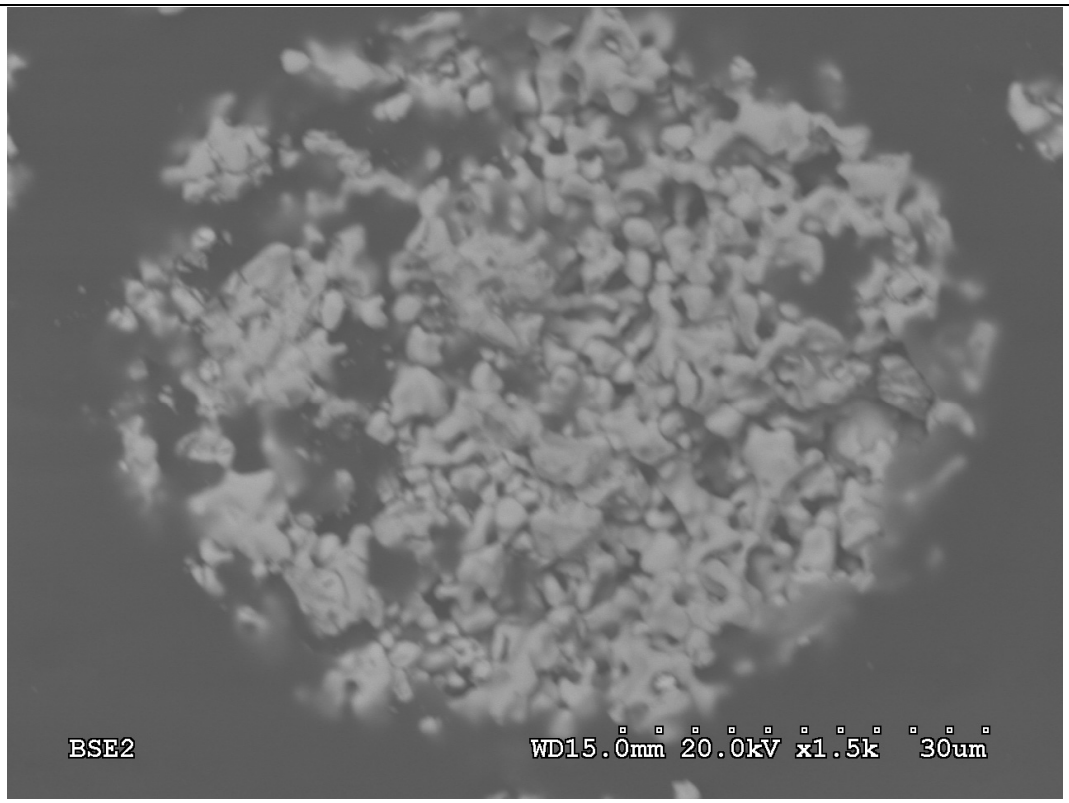

Dy-5

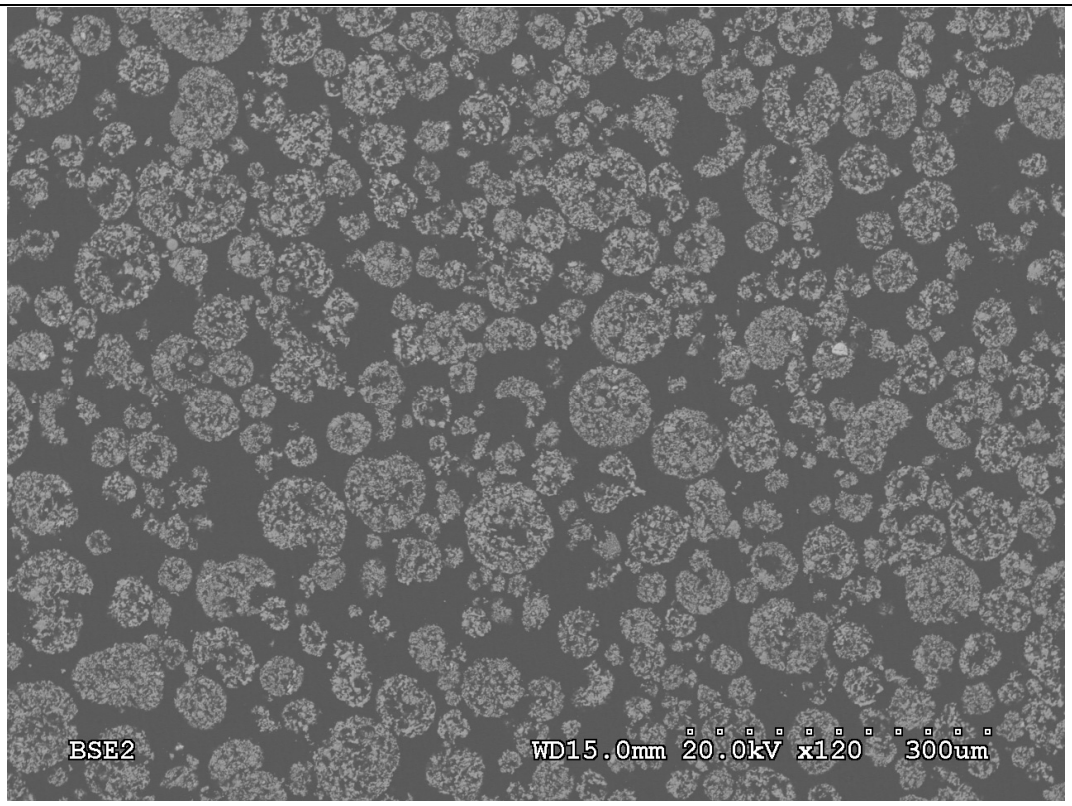

Dy-10

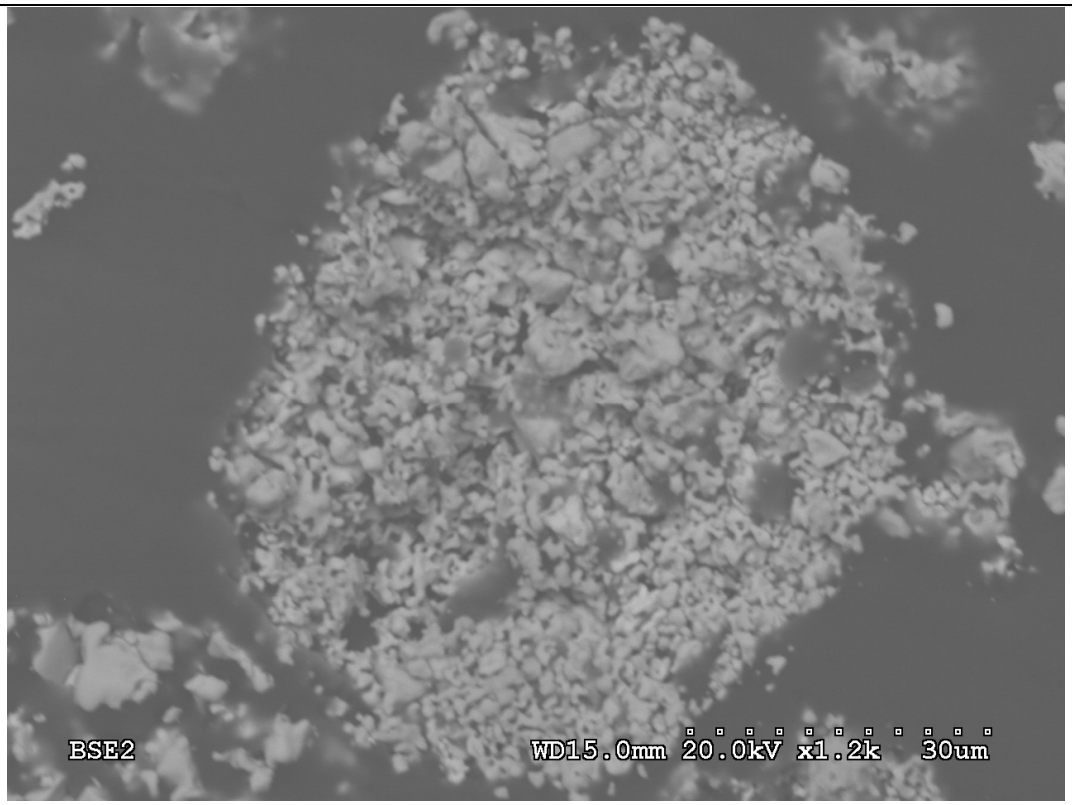

Dy-10

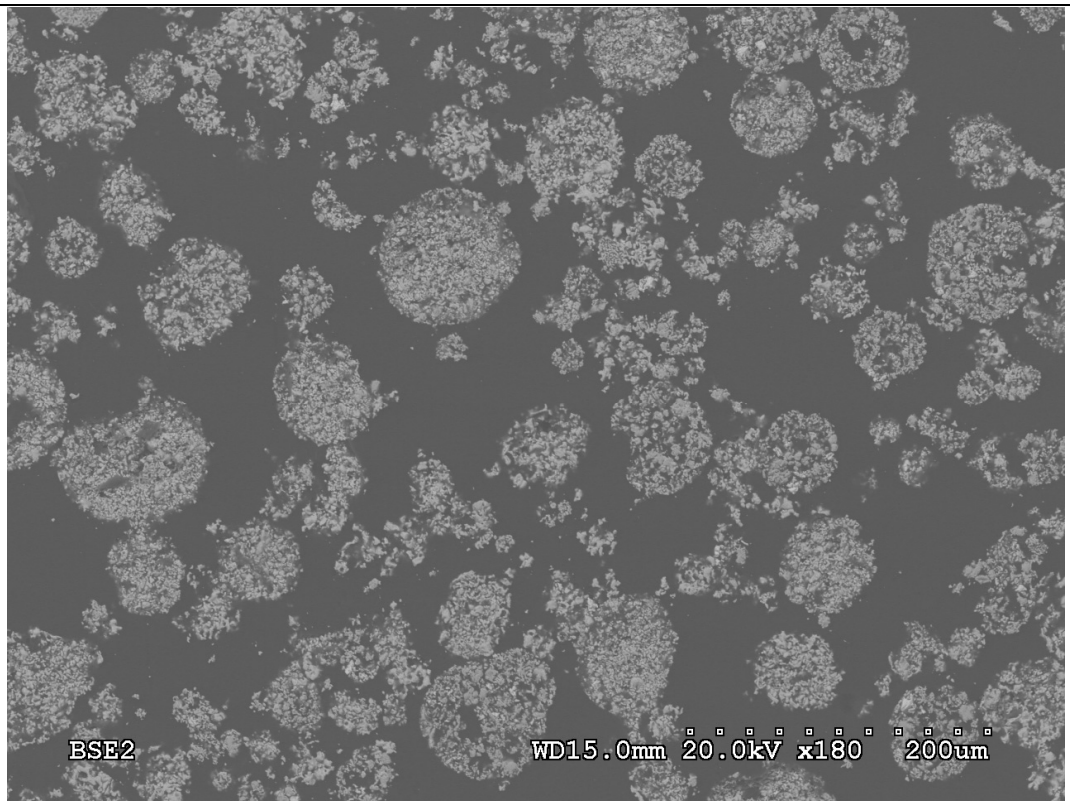

Dy-15

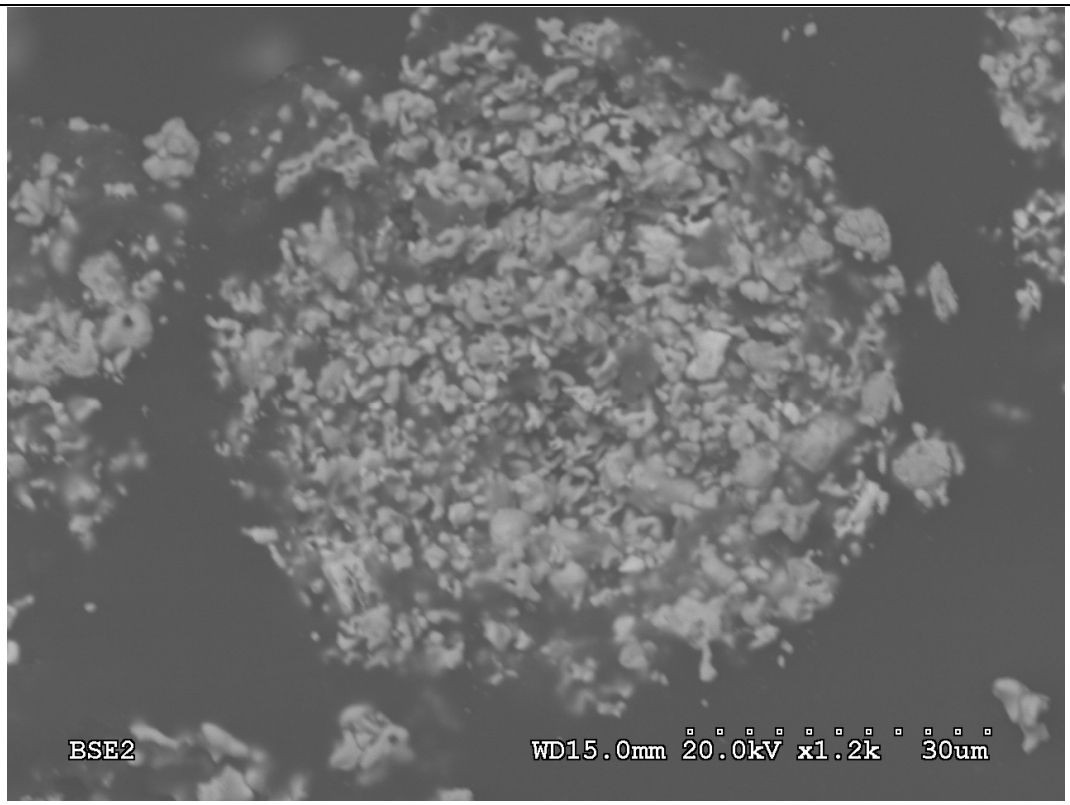

Dy-15

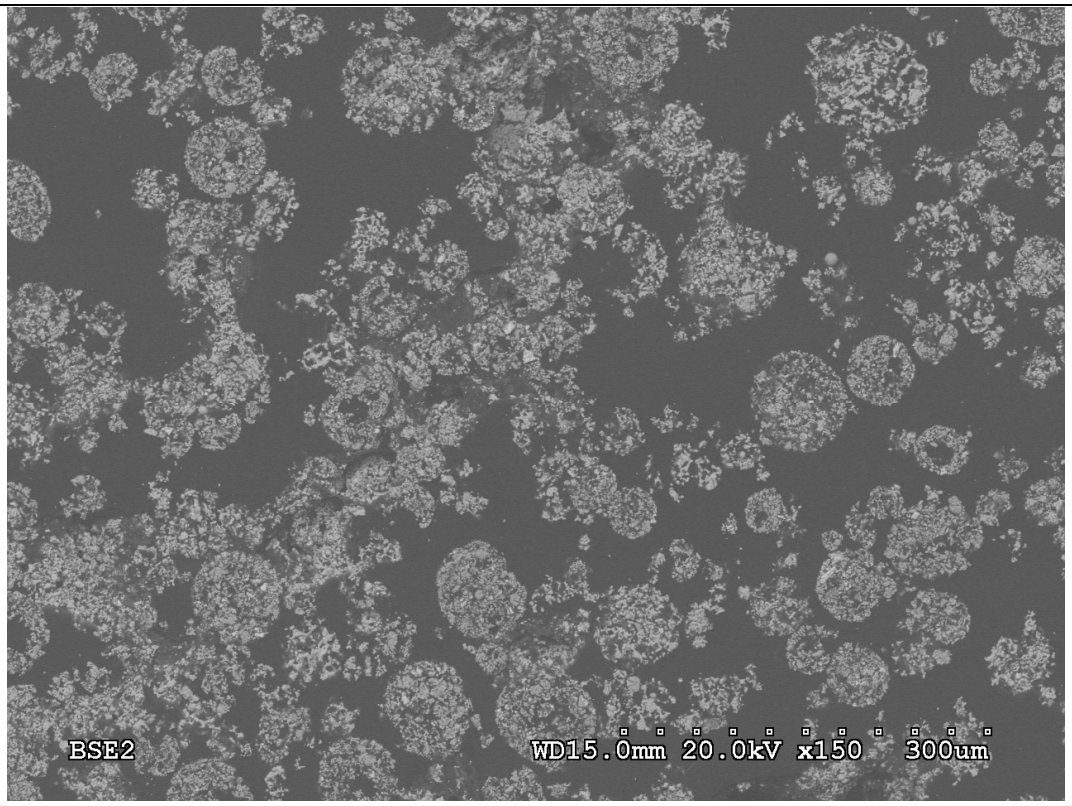

Dy-20

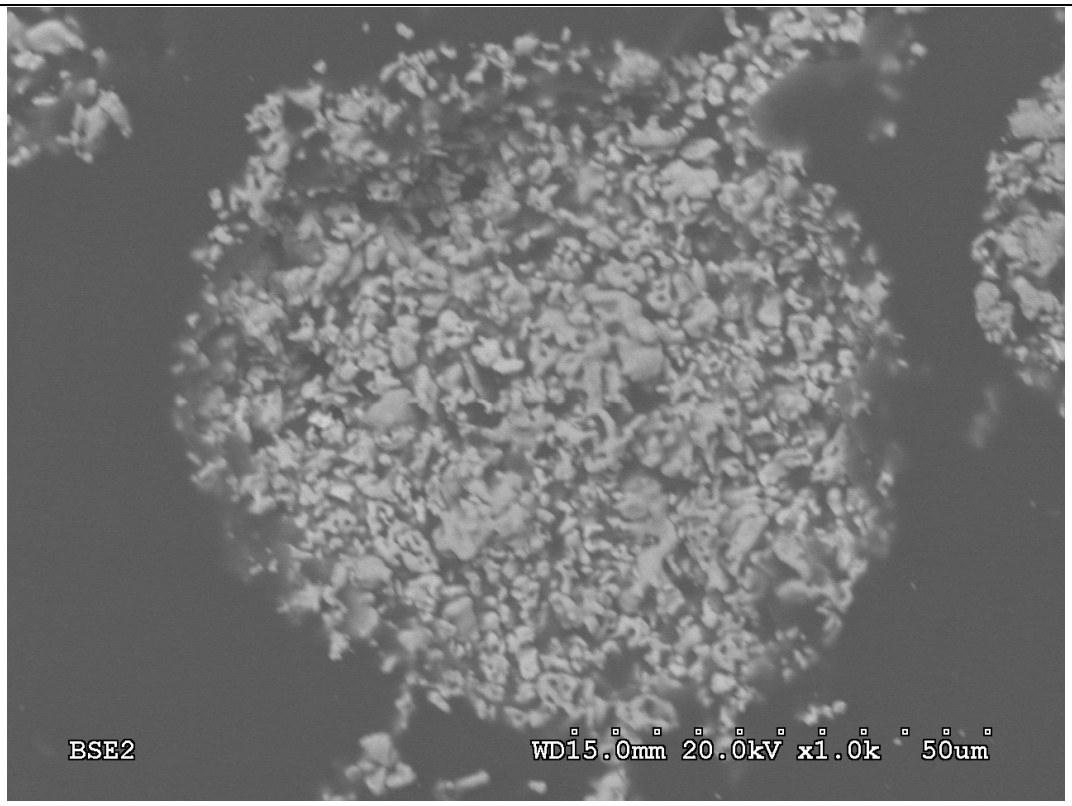

Dy-20

Figure 1: SEM BSE micrographs of as-received powder mounted in epoxy and polished

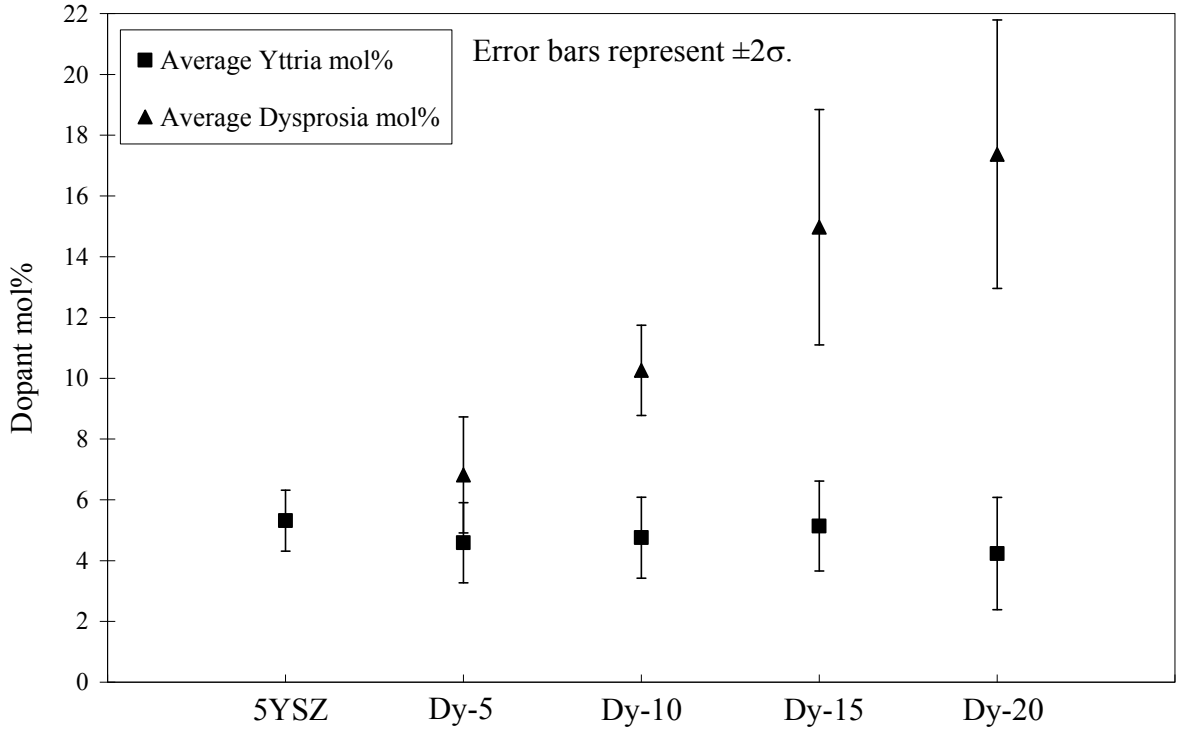

Figure 2: As-received powder chemistry determination by SEM/EDS (ZAF)

Table 5: XRD parameters

X-ray Type	Current (mA)	Voltage (kV)	RS Width (mm)	FDS Angle (º)	Primary Soller Slit (º)	Scan Range (2θ)	Scan Speed (º2θ/s)	Equipment Relative Error (%)
Cu-Kα	30	40	0.6	1	2.3	23-146	0.04/2	2

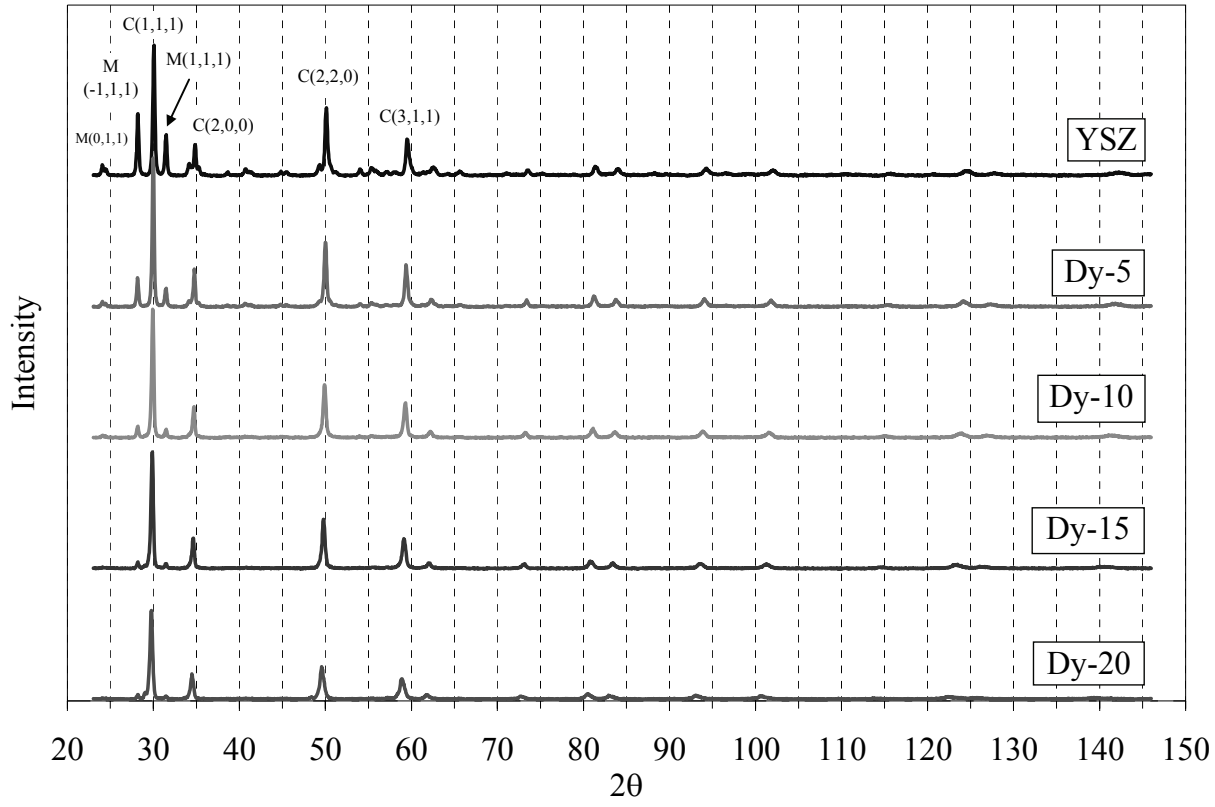

Figure 3: XRD spectra of as-received powders with major peaks labelled (M = monoclinic, T = tetragonal, C = cubic)

Table 6: XRD Rietveld refinement estimate for phases present in as-received powders

Phase(s) Present	5YSZ	Dy-5	Dy-10	Dy-15	Dy-20
Rietveld Estimate	48.2% M 51.8% C	27.4% M 72.6% C	13.6% M 86.4% C	7.2% M 0.5% T 92.3% C	4.7% M 1.6% T 93.7% C

(Zirconia: M = monoclinic, T = tetragonal, C = cubic)

3.2 Plasma Spray Equipment and Parameters

To produce TBCs, NiCrAlY (Carpenter Powder Products, Bridgeville, PA) and Dy-YSZ powders were fed through the APS system (Axial III Model 600, Northwest Mettech Co., North Vancouver, BC, Canada). The typical equipment setup is illustrated in Figure 4. Multiple plate-shaped specimens (25.4 mm wide x 127 mm long) can be affixed to the outer diameter of

specimen holder, while rod-shaped specimens (Ø7.9 mm x 127 mm long) can only be secured at the top of the holder, one piece per run. All plate-shaped specimens were cut from mild steel flat bar. Two (2) types of Ni-based rod specimens were utilized: a superalloy with unknown pedigree (Table 7), and CMSX-11B single crystals (Table 8) provided by Solar Turbines Inc. The chemistries of both Ni-based substrates were determined by SEM/EDS based on one spectrum each, thus they should be treated as preliminary references only. CMSX-11B crystals were received in Ø12.7 x 203 mm section and were then cut down to required size by EDM. These rod specimens were in the solution annealed condition, and they were given a triple ageing process to develop γ' phase prior to coating process (5 hours at 1120-1130°C, 24 hours at 865-870°C, 30 hours at 670-680°C). The substrate material was not a primary concern of this study.

The Axial III plasma torch contains three (3) sets of anode/cathode pairs, gas lines, and water cooling lines. In effect, during operation the torch utilizes three (3) plasma plumes, which surrounds the central powder injection line, to melt and propel the feedstock toward specimens. Typical operational parameters are summarized in Table 9 and 10. Powder feed rate targets were calibrated by utilizing carrier gas and powder of interest to fill a sealed container, which rests on a digital scale. The rates of change in mass were timed with stopwatch and the typical targets are shown in Table 10. All substrates were sand blasted prior to coating (silica sand). Sand blasting cleans the surface of any residual oil-based substances and increases surface roughness to facilitate improved adhesion with bond coat.

Table 7: Chemical composition of Ni-based superalloy in wt% (rod specimens for June 9, 2004 – October 6, 2005)

Aluminum	Silicon	Chromium	Cobalt	Nickel	Molybdenum	Tantalum	Tungsten
4.79	2.38	6.77	1.29	62.42	4.00	9.77	6.28

Table 8: Chemical composition of CMSX-11B single crystals in wt% (rod specimens for October 12, 2005 – October 18, 2005)

Aluminum	Silicon	Chromium	Cobalt	Nickel	Molybdenum	Titanium	Tungsten
3.44	3.42*	11.40	5.55	59.98	0.48	3.98	5.69

(* Silicon level was much higher than manufacturer's certification of <0.010; contamination from polishing is possible.)

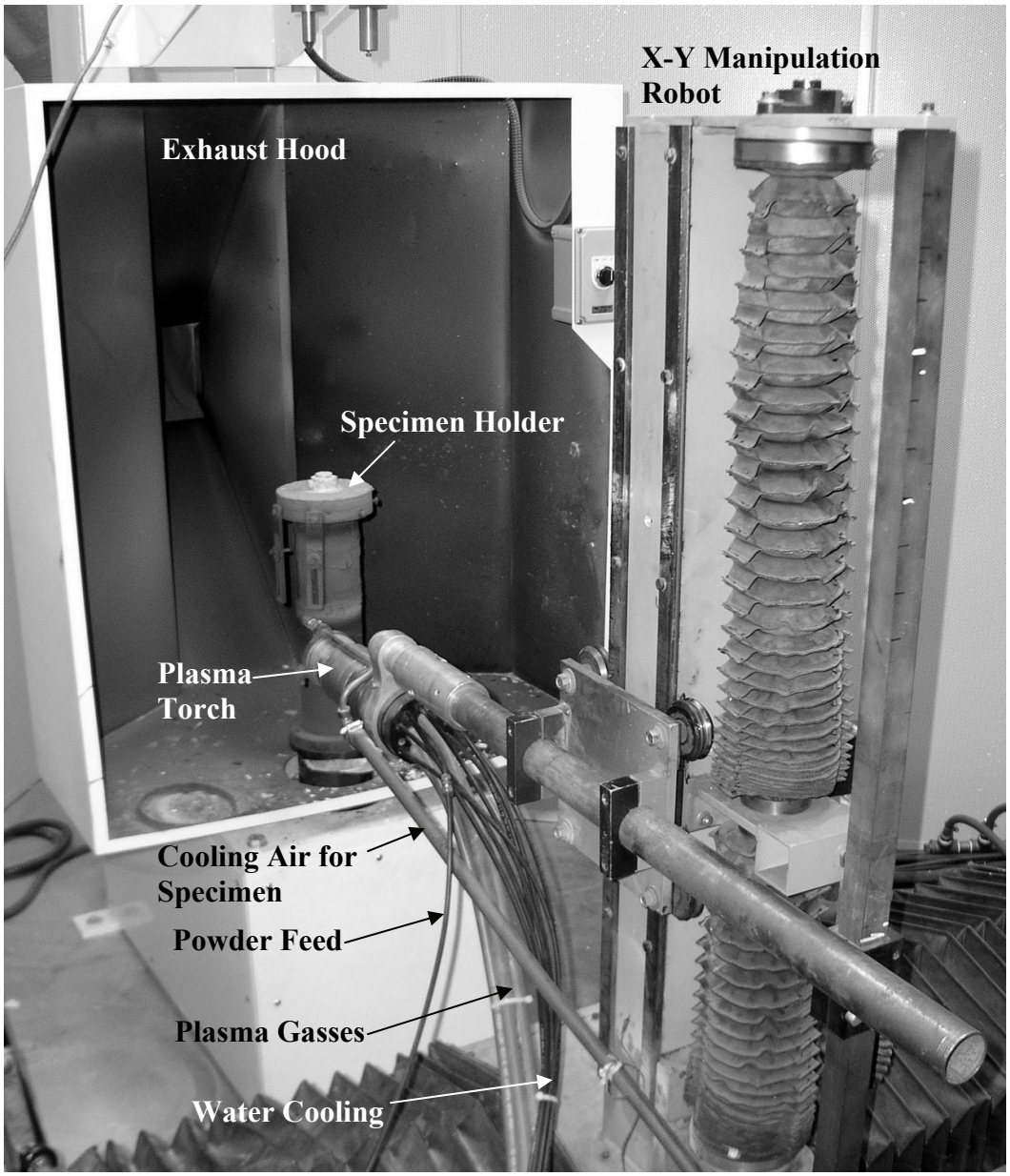

Figure 4: Plasma spray equipment setup

Table 9: Typical parameters for APS (Axial III)

Coating Material	% Hydrogen	% Nitrogen	% Argon	Plasma Gas Flowrate (L/min)
Dy-YSZ	25	75	0	150
NiCrAlY	20	10	70	250

Coating Material	Carrier Gas Flowrate (L/min)	Current (A)	Voltage (V)	Nozzle Size (in)	Standoff Distance (mm)
Dy-YSZ	10	240	166	0.5	150
NiCrAlY	12	230	144	0.5	150

Table 10: APS parameters for different specimens

Specimen Type	RPM	Y Traverse Speed (mm/s)	NiCrAlY Feed Rate Target (g/min)	Dy-YSZ Feed Rate Target (g/min)
Rod	480	48.05	10	15
Plate	572	57.2	80	60

3.3 Laser Flash and Differential Scanning Calorimetry Parameters

Dy-YSZ coating specimens for determination of thermal diffusivity and specific heat were deposited onto aluminium buttons (Ø8 mm). They were subsequently detached easily due to large difference in thermal contraction rate between coating and substrate, and also the relatively smooth surface finish of the buttons (as machined). The typical thickness was in the range of 300-500 μm. Specimens were sent to the National Research Council – Industrial Materials Institute (Boucherville, QC, Canada) for thermal diffusivity evaluation at room temperature. Specimens for thermal diffusivity determination require sub-micron layers of sputtered graphite prior to testing. This extends from the fact that zirconia is essentially transparent to radiation with wavelengths of <5 μm at room temperature, and YAG lasers typically operate with wavelengths of 1-2 μm.[11,46] For DSC (TA Instruments, Q-1000, New Castle, DE, USA) measurements, the standard reference material was sapphire. Equipment and operational parameters are summarized in Tables 11 and 12.

Table 11: Laser flash equipment and parameters

Laser Type	Pulse Energy (J)	Pulse Duration (μs)	Signal Detector Type	Signal Digitization	Sample Thickness (μm)
YAG (IMI Custom Built)	0.8	70	InSb	Nicolet 440 Scope	300-500

Table 12: DSC parameters for TAI Q-1000

Method	Mode	Purge Gas	Sampling Interval	Heating Rate (°C/minute)	Sample Thickness (μm)
Direct C_p	T4P	Nitrogen	1 second/pt	20	300-500

3.4 Thermal Cycling Equipment and Parameters

A customized thermal cycling vertical tube furnace had to be constructed for this research project, as no suitable equipment was available. Figure 5 presents a quick reference of the major components, while Figure 7 shows the specimens at rest position. An unused furnace power supply was upgraded with PLC and connected to a vertical tube furnace as shown. The alumina tube was 77.5 cm long, 5.75 cm in ID, and 3.5 mm thick. Furnace hot zone was approximately 15 cm in height, vertically centered with respect to furnace body. Each opening of the alumina tube was secured to the furnace body mechanically and these fixtures were water cooled. A type S thermocouple 40 cm in length was secured from the top of alumina tube and centered geometrically. The thermocouple was connected to an analog chart recorder through a cold junction compensator. Set point for the furnace was 1187°C, and its internal thermocouple was located at the center of hot zone, in contact with the OD of alumina tube.

Immediately next to the furnace is the vertical movement arm, which was modified with a sample holder apparatus and limit switches for automated control. The automated movement controller was built with internal timers and the stroke timing was such that the full cycle time was 43 minutes. Full cycle time is defined as the length of time from initiation of sample insertion into the furnace (up-stroke), to completion of sample withdraw ending at rest position (down-stroke). Traverse distance was 31 cm, with up-stroke and down-stroke times of 2 minutes

each. Hot zone residence time was 18 minutes, and cool down time at rest position was 21 minutes.

The sample holder apparatus consisted of 5 steel rods, equally spaced and located at positions which fit into the alumina tube. Each rod was connected to a gear and motor system at the base which turned the rods at 10 RPM. This motorized unit was water cooled as shown in Figure 5 (bottom right). Located directly above each steel rod is the quartz tube (Ø8 mm ID by 35-38 cm long), which holds coated specimens at the appropriate height. The clearance between quartz tube and alumina tube ID wall was generally small (1-2 mm). Each quartz tube was cut from longer stock by hand, and any remaining fine cracks were sealed by heating with oxygen-acetylene torch. Instabilities still remain in that the thermal cycle temperatures are consistent with cristobalite formation, and the rapid temperature change can shock the quartz. Indeed most quartz tubes showed signs of cracking after thermal cycling, with complete breakdown being infrequent (1 of 15 samples).

A typical thermal cycle temperature profile is shown in Figure 6. Upon full load sample insertion, the furnace air temperature can drop to 970°C. Recovery time is typically about 13 minutes. It should be noted that the experimental setup as described above do not include internal cooling for the sample substrates, unlike structural components found in turbines.

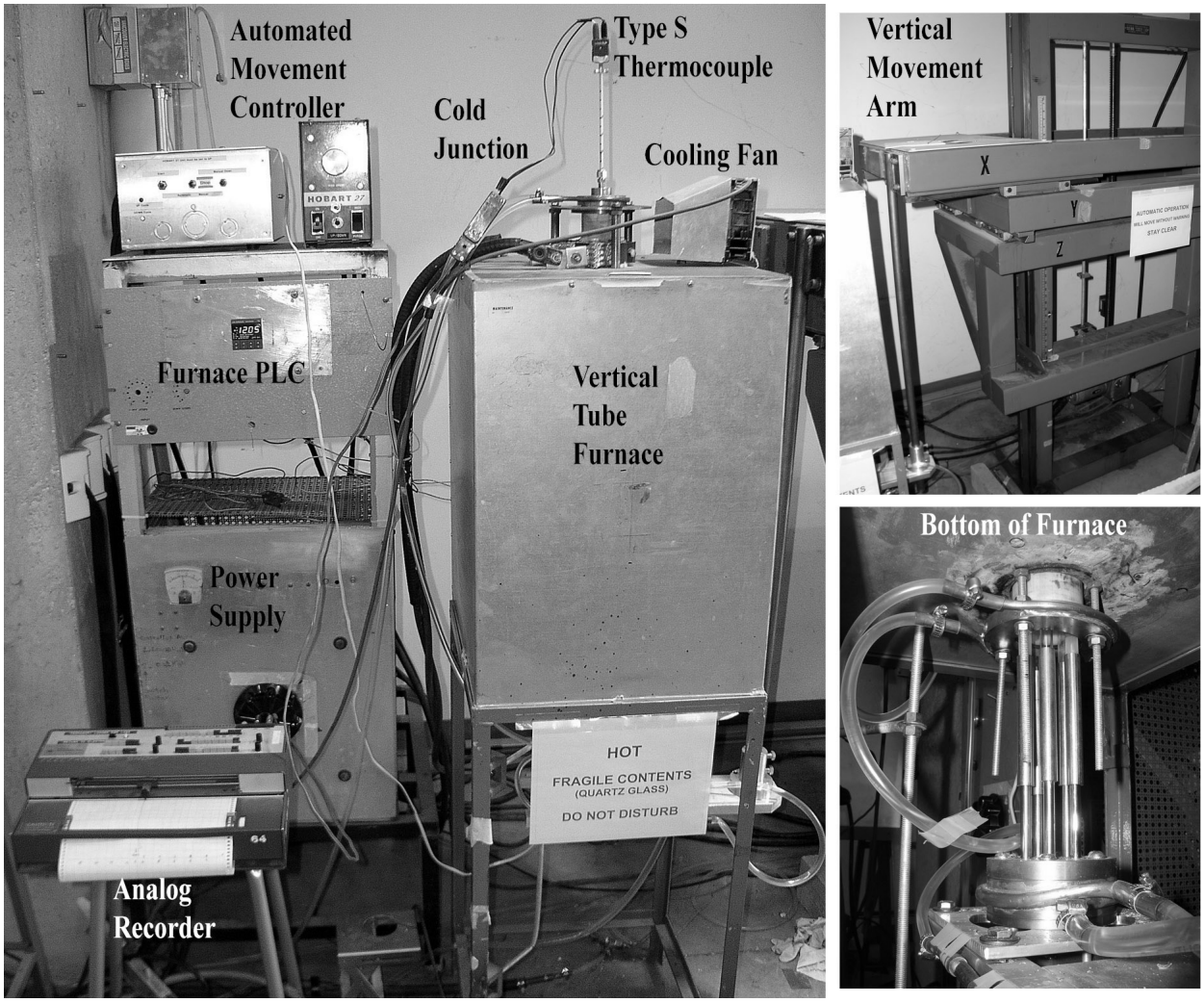

Figure 5: Customized thermal cycling vertical tube furnace (with descriptions)

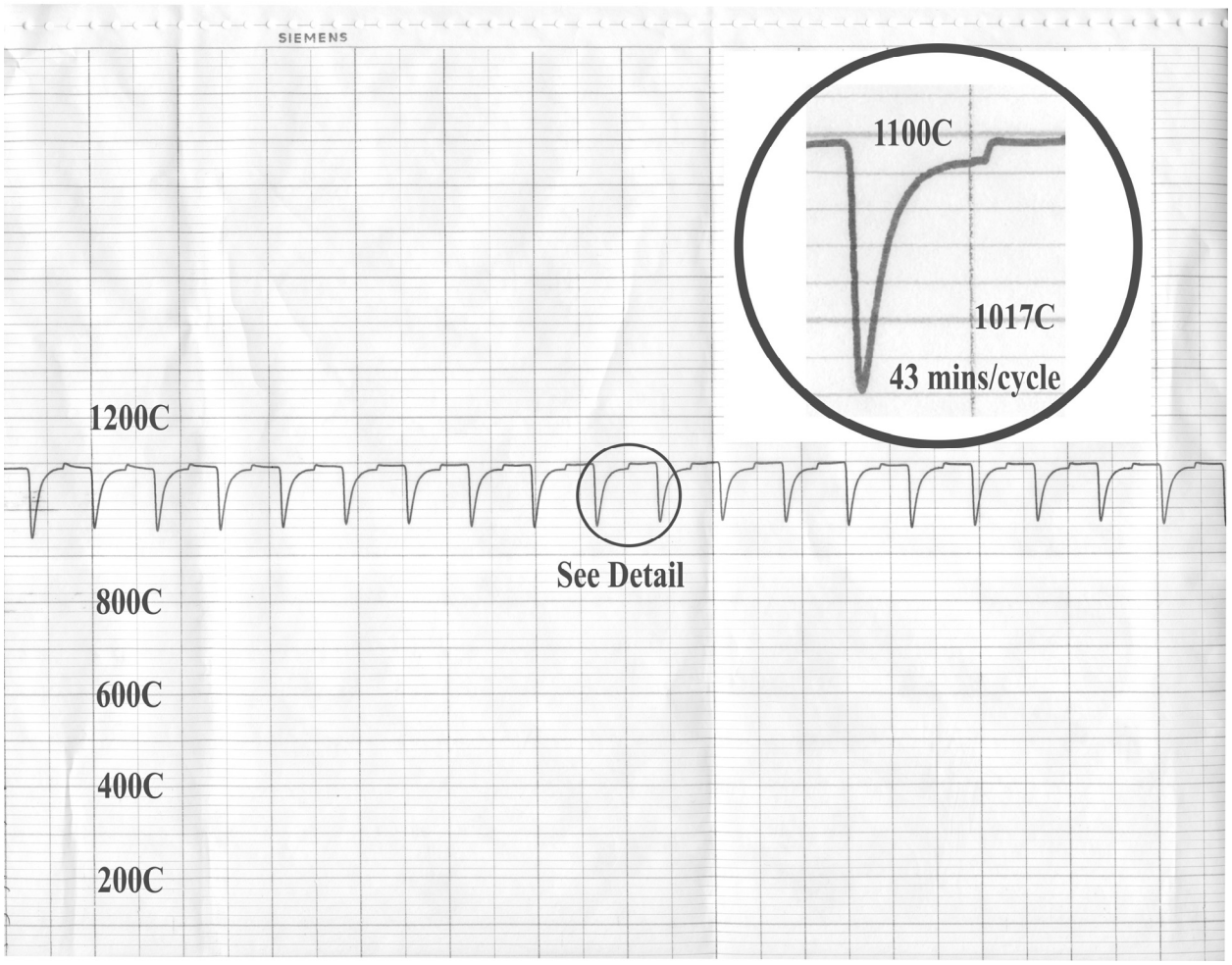

Figure 6: Typical temperature profile from thermal cycle trials

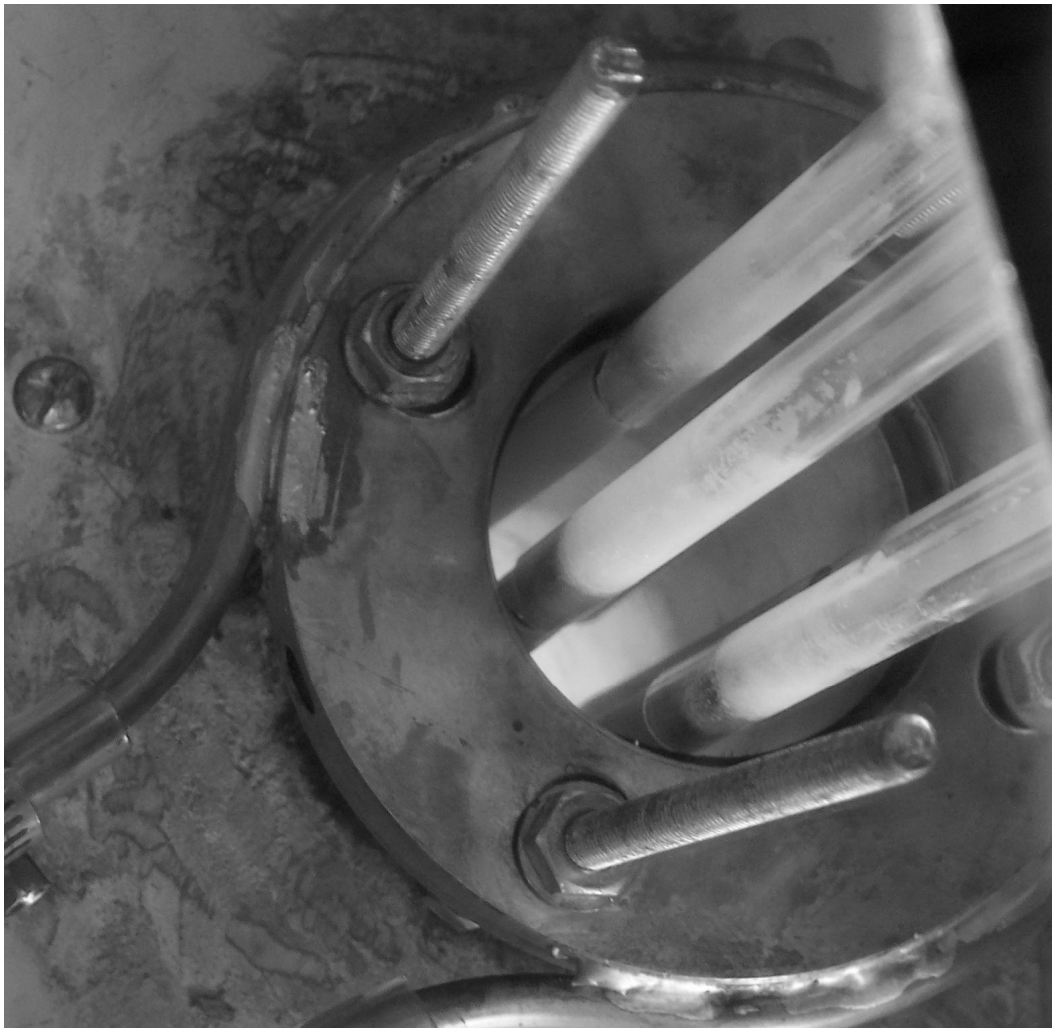

Figure 7: Bottom view of tube furnace, showing active thermal cycle with specimens at rest position

3.5 Image Analysis Software and Parameters For Porosity Determination

The image analysis software used in the current research is ImageTool version 3.0 final, developed by C. Donald Wilcox, S. Brent Dove, W. Doss McDavid, and David B. Greer at the Department of Dental Diagnostic Science at The University of Texas Health Science Center, San Antonio, Texas, USA. Images were acquired by SEM under back scatter mode and at a magnification of 180-300x, depending on coating thickness. As-captured images are grayscale and sized at 1280x960 pixels. Ten (10) images were acquired for each sample at random locations. Each image was then cropped to 870 pixels in height in order to remove text from SEM, such as magnification and kV value. Next, the threshold function in ImageTool was used

to convert all pixels into black or white by setting upper and lower limits as 100 and 0, respectively. This forces all pixels with intensities greater than 100 to become black, and all other intensities to become white (see Figure 8). The resulting images were then analyzed by ImageTool (Analyze Object command) and objects matching the search parameters were outlined. In this case the objects are black pixels representing porosity. Each object's area was recorded and exported into a spreadsheet. A summary of parameters is shown in Table 13. Note that for thermally cycled coatings, the threshold limits were different from as-sprayed coatings due to two (2) factors. First, the porosity level and size were smaller. Second, the amount of useful area available for image analysis was less, since the higher coating brittleness led to frequent damage during cutting and polishing. These factors necessitated higher magnifications (600-1500x) and thus the images were generally brighter.

Since there are thousands of objects per image, this process was automated through the use of scripts. The total pixel area of porosity was then be compared against the pixel area of each image (1280x870 pixels), and an average value over ten (10) images was determined. The volume percent porosity determined by this method assumes that pores and cracks are 2D entities, thus it is likely to be a conservative estimate. In addition, this method is influenced by subjectivity of the software user, where thresholding is particularly affected.

Table 13: ImageTool parameters for image analysis

Image Type	Image Size	Threshold Limits	Minimum Object Size	Data Reporting
Grayscale	1280x870 pixels	0-100 (As-sprayed) 0-155 (Cycled)	2 pixels	Each object area; export to Excel

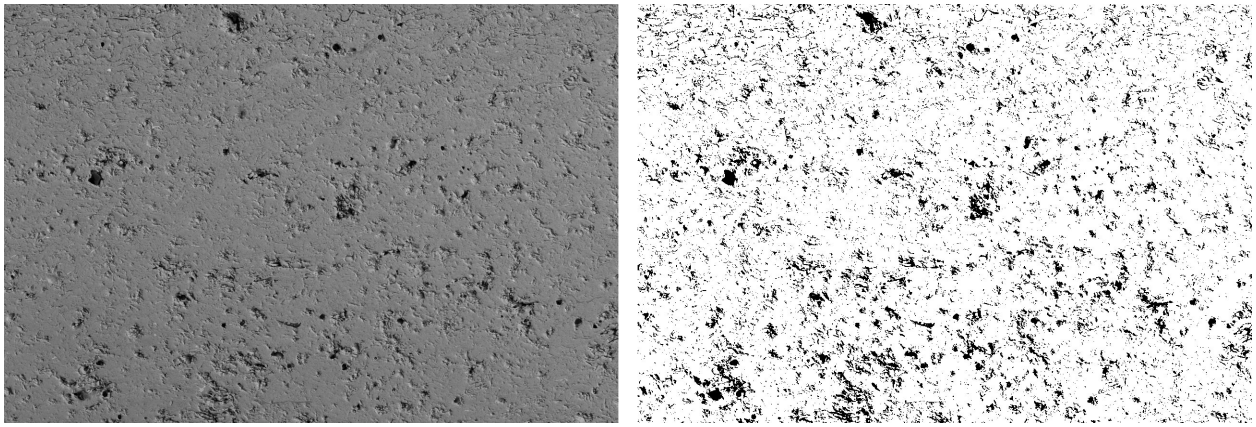

Figure 8: Dy-5 coating - SEM (BSE) at 180x magnification at left; thresholded at right

CHAPTER IV – Experimental Data, Model, and Discussion

4.1 Chemistries Of and Phases Present in As-sprayed Coatings

The four (4) Dy-YSZ powders were deposited onto rod specimens on June 9, 2004, while 5YSZ was later deposited onto a plate specimen on November 29, 2004. The powder manufacturer had to replace the original 5YSZ material as it was not supplied to requirements, thus causing the delay. The original 5YSZ material (hollow spheres) was not employed in this study.

The coated specimens were mounted in Cold Cure epoxy, sectioned, and polished with 3 μm diamond solution on fine cloth. Representative micrographs of each coating are shown in Figure 9. The same chemistry analysis procedure as for powders was followed, and ten (10) areal readings were collected for each coating at random locations. The results are illustrated in Figure 10. Compared with powders, the largest differences in mean values were observed for Dy_2O_3 in Dy-5 and Y_2O_3 in Dy-20, with -0.92 mol% and -0.95 mol% respectively. Histograms for these two coatings and their respective powders are shown in Figures 11-14. The distribution of data was much tighter than those seen in powders: here 2σ was between 0.18-0.46, compared with 1.00-4.42 for powders. Statistical tests for determining whether two mean values from two data sets are significantly different, such as Student's t-test (equations 49-50), cannot be performed since the data variance differs greatly. The F-test for variance (equations 51-52) was highly significant ($p = 0.01$ or 99% confidence) for these data sets. Thus the primary driver for lower mean values of yttria or dysprosia was more likely melting and homogenization during APS, with actual loss of dopant material possibly acting as a secondary cause.

$$t = \frac{\overline{x_1} - \overline{x_2}}{\sqrt{\frac{\sigma_1^2}{n_1} + \frac{\sigma_2^2}{n_2}}} \tag{49}$$

$$DF = \frac{\left(\frac{\sigma_1^2}{n_1} + \frac{\sigma_2^2}{n_2}\right)^2}{\frac{\sigma_1^4}{n_1^2(n_1 - 1)} + \frac{\sigma_2^4}{n_2^2(n_2 - 1)}} \tag{50}$$

$$F = \frac{\sigma_1^2}{\sigma_2^2} \tag{51}$$

$$DF = n_1 - 1, n_2 - 1 \tag{52}$$

For XRD and Rietveld refinement, the remaining coatings were mechanically chipped off of the substrates and again, the same sample preparation procedure as for powders was followed. Due to sample contamination from NiCrAlY bond coat, the empty peaks function was used to filter out known peaks for bond coat. The remainder of peaks were analyzed by Rietveld refinement and the results are summarized in Table 14. The difference in phase composition between Table 6 and 14 is due to remelting and rapid solidification during APS. Full cubic phase for all Dy-YSZ coatings was expected, since Y_2O_3-ZrO_2 and Dy_2O_3-ZrO_2 binary phase diagrams predict cubic phase stability between 10 mol% and 40 mol% dopant.[47,48]

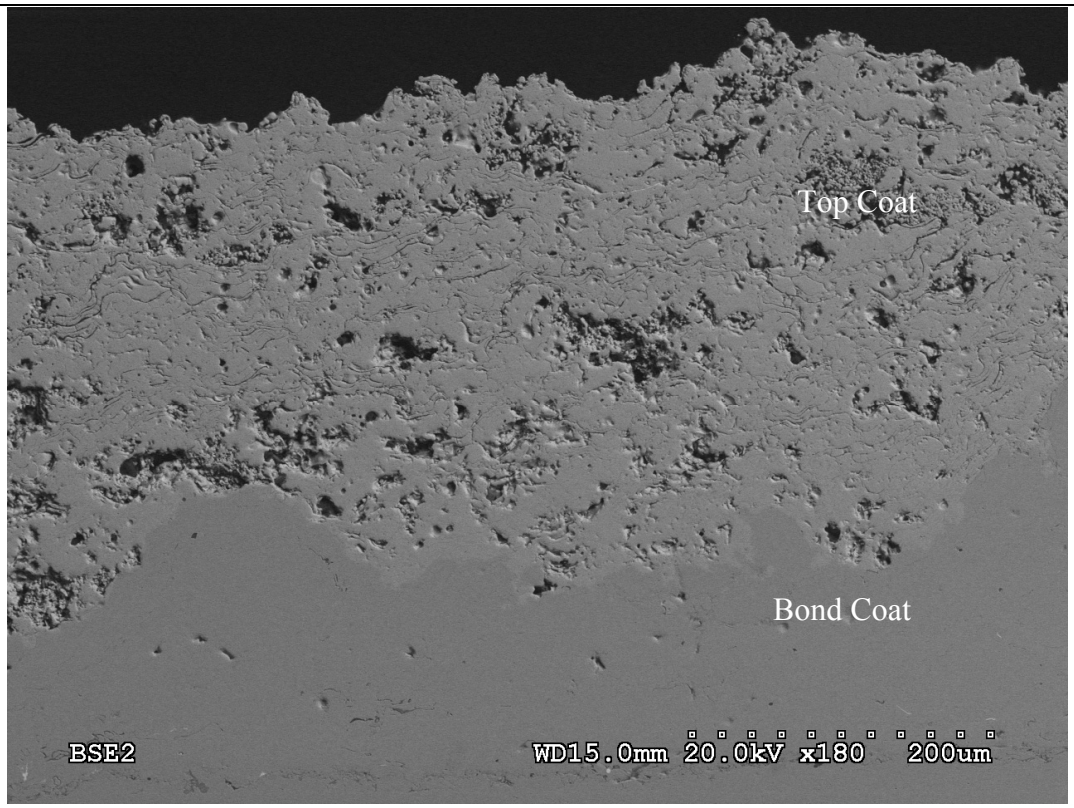
Top Coat
Bond Coat
BSE2
WD15.0mm 20.0kV x180 200um

5YSZ

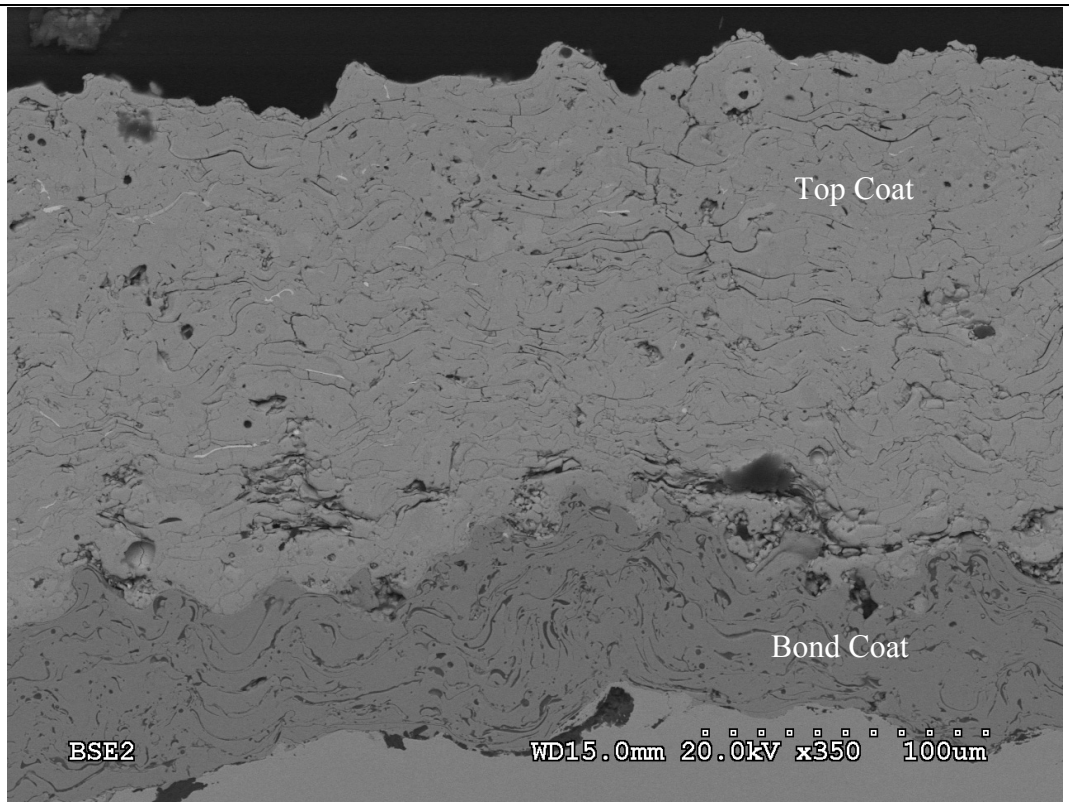
Top Coat
Bond Coat
BSE2
WD15.0mm 20.0kV x350 100um

Dy-5

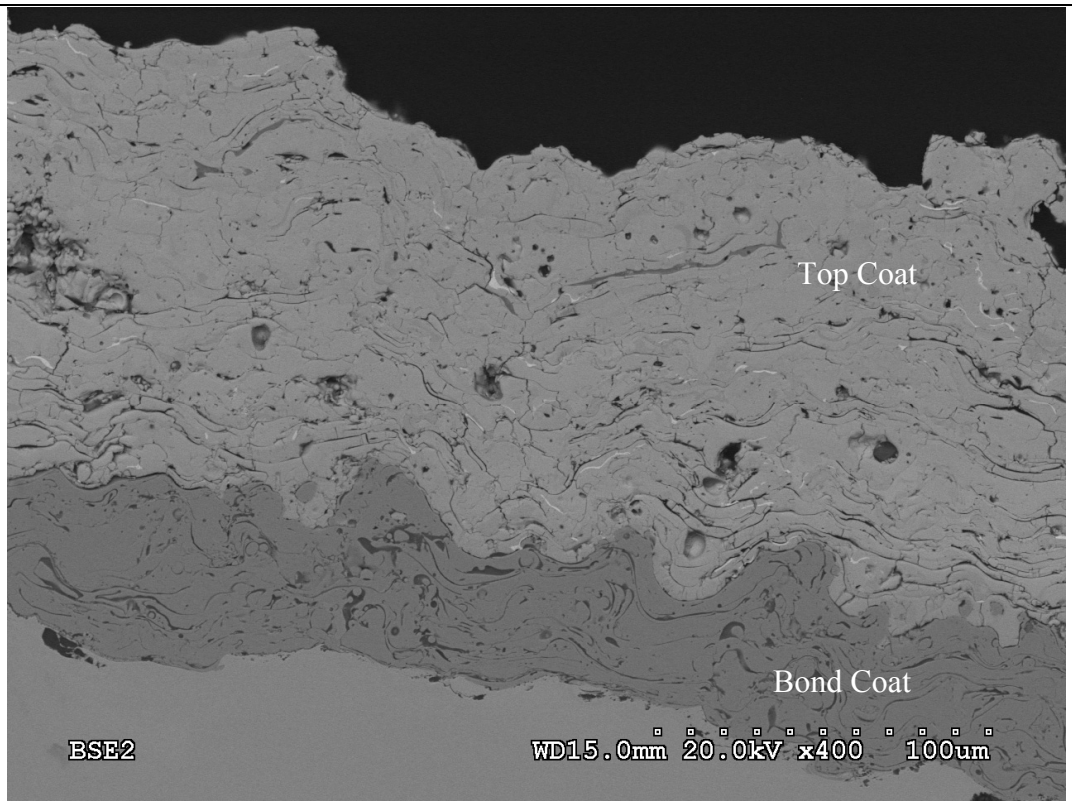
Top Coat
Bond Coat
BSE2
WD15.0mm 20.0kV x400 100um

Dy-10

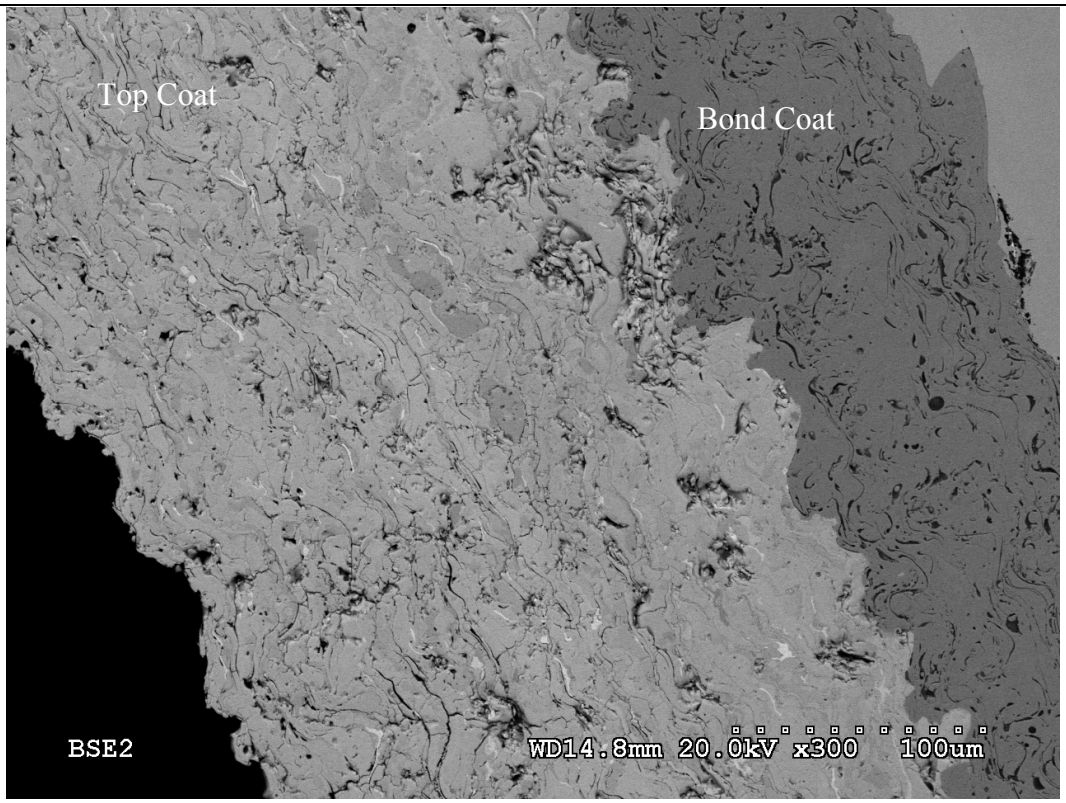
Top Coat
Bond Coat
BSE2
WD14.8mm 20.0kV x300 100um

Dy-15

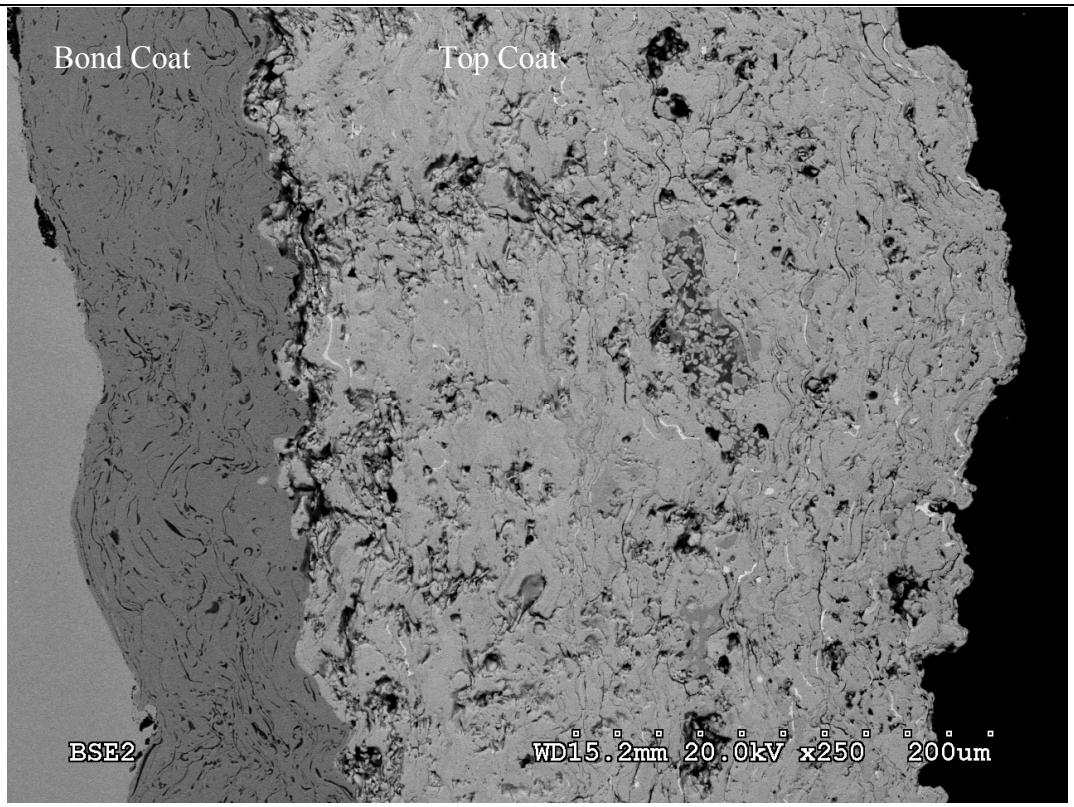

Dy-20

Figure 9: SEM BSE micrographs of as-sprayed coatings mounted in epoxy and polished; light porous layer is TBC, dark porous layer is NiCrAlY, and solid grey layer is substrate

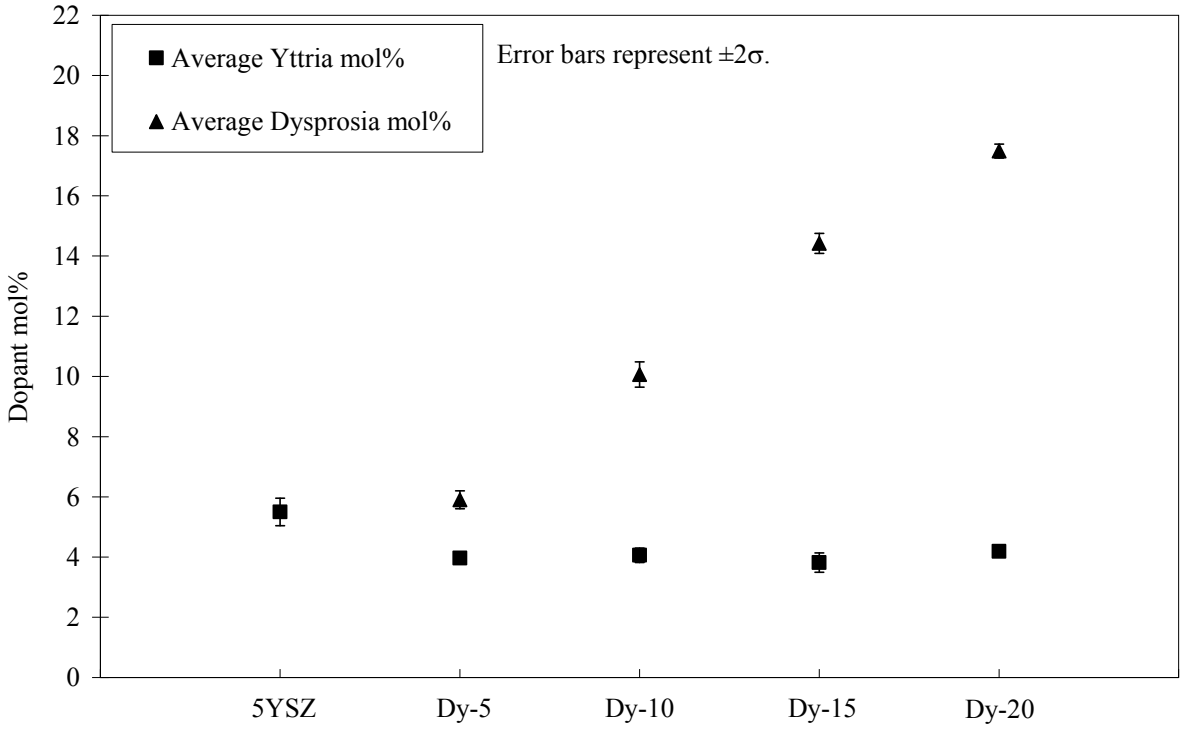

Figure 10: As-sprayed coating chemistry determination by SEM/EDS (ZAF)

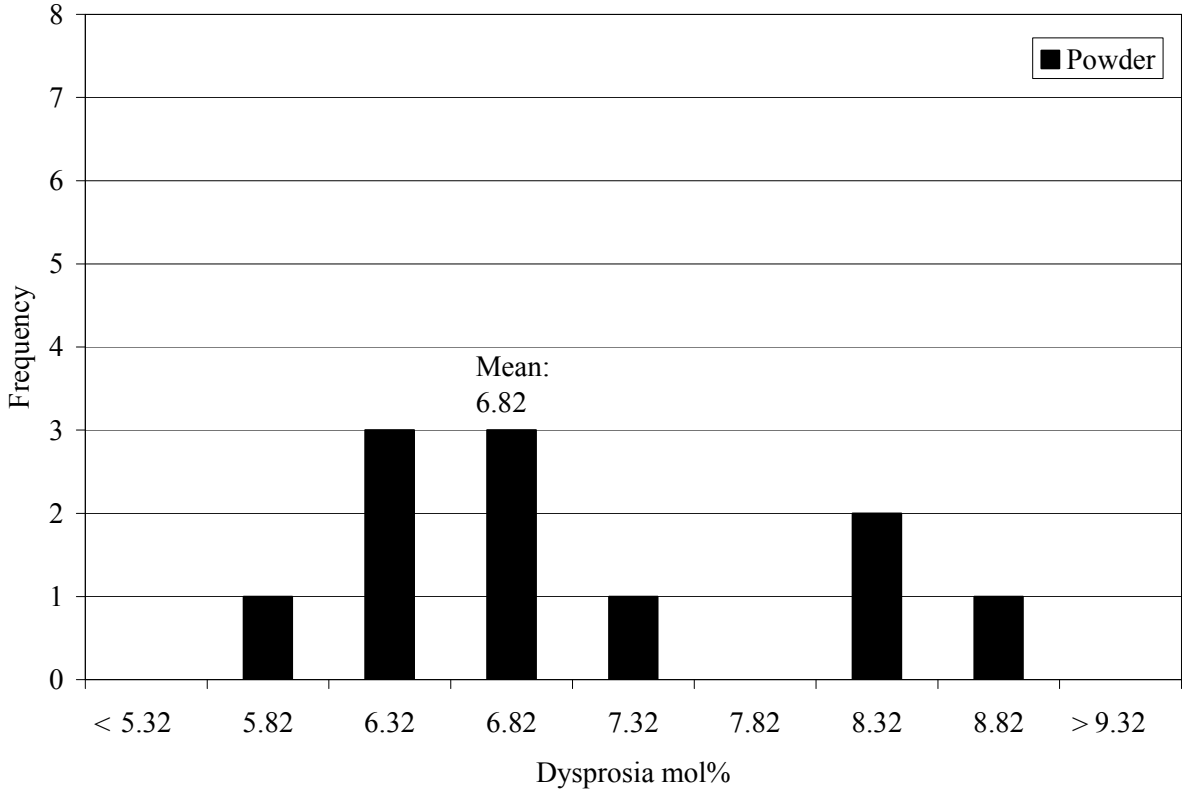

Figure 11: Chemical analysis histogram for Dy_2O_3 in Dy-5 powder; each column represents cumulative frequency in the preceding interval (e.g. column 6.32 contains data for the range 5.83-6.32)

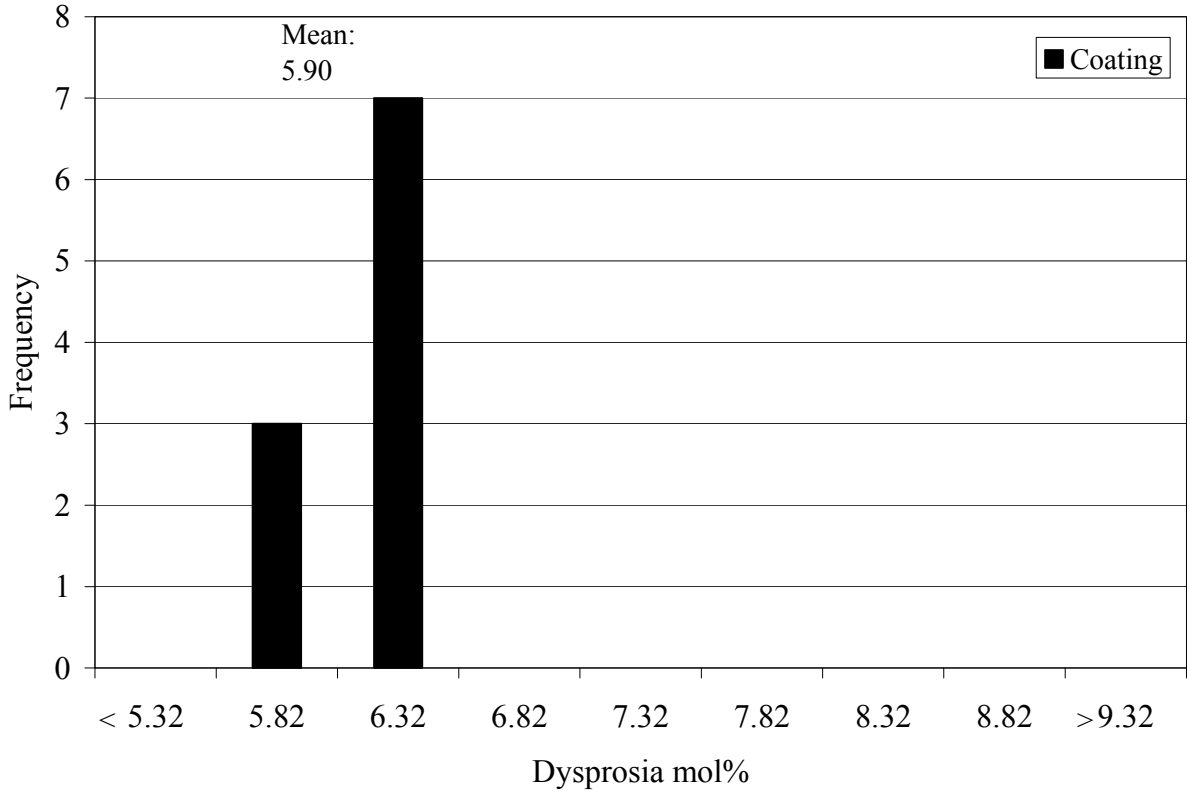

Figure 12: Chemical analysis histogram for Dy2O3 in Dy-5 coating; each column represents cumulative frequency in the preceding interval (e.g. column 6.32 contains data for the range 5.83-6.32)

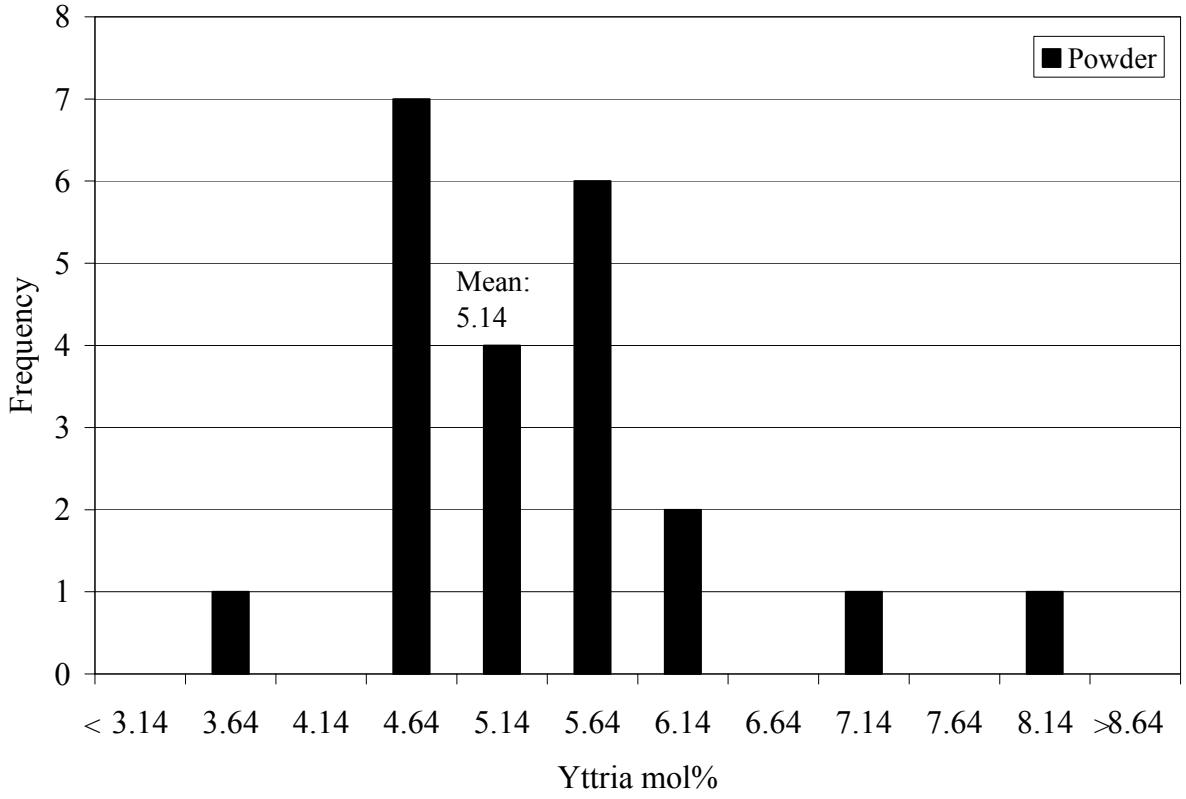

Figure 13: Chemical analysis histogram for Y_2O_3 in Dy-20 powder; each column represents cumulative frequency in the preceding interval (e.g. column 4.64 contains data for the range 4.15-4.64)

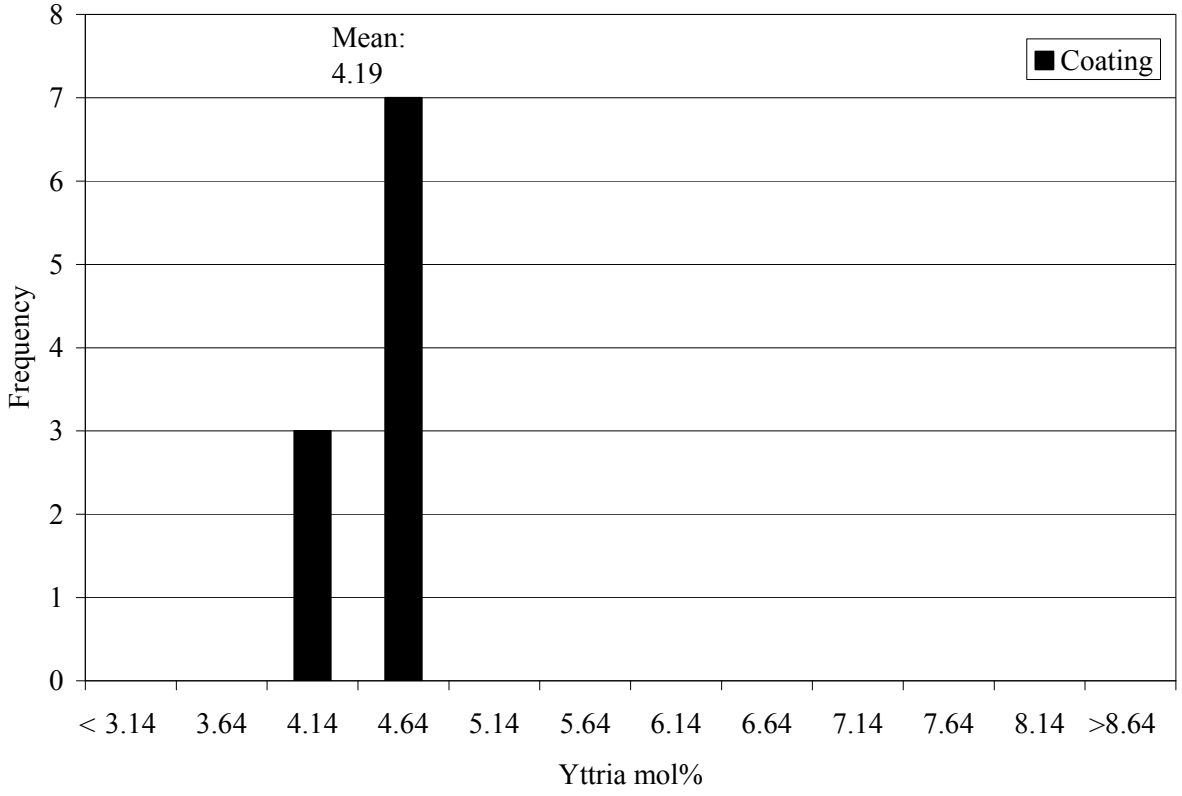

Figure 14: Chemical analysis histogram for Y_2O_3 in Dy-20 coating; each column represents cumulative frequency in the preceding interval (e.g. column 4.64 contains data for the range 4.15-4.64)

Table 14: XRD Rietveld refinement estimate for phases present in as-sprayed coatings

Phase(s) Present	5YSZ	Dy-5	Dy-10	Dy-15	Dy-20
Rietveld Estimate	4.6% M 81.7% T 13.7% C	100% C	100% C	100% C	100% C

(Zirconia: M = monoclinic, T = tetragonal, C = cubic)

4.2 Porosity Levels in As-sprayed Coatings

The image analysis procedure as outlined in section 3.5 was applied to five (5) batches of coatings, dated Feb. 22, Apr. 4, Apr. 25, Jul. 21, and Aug. 4, 2005. Strictly speaking, the porosity levels measured by image analysis are areal fractions. The current research assumes

that this is a reasonable estimate of volume fraction of porosity, given that a sufficiently large sample size was collected. Bias is still expected due to the anisotropic crack morphology and that all images were taken in the transverse direction. A total of fifty (50) experimental data points were compiled for each material, and whereas Figures 15-19 separate them into batches, Figure 20 shows the overall averages as well as 2x standard deviations for the entire data set. The relatively large variance in porosity data can be attributed to the uncertainties and variability of the APS process and irregular coating microstructures (as seen in Figure 9). The APS variables include particle velocity, the degree of melting, particle size, substrate impact angle, etc. However, 5YSZ generally seems to be more porous than the other four (4) coatings (mean of 14.1% vs. 8.5-10.9%). The implication could be that more superheat is available to Dy-YSZ particles arriving at the substrate, resulting in higher densification. This effect could be caused by a common phenomenon in ceramics and slags, where a ternary or higher order system exhibits low melting temperature eutectic(s). Since a ternary phase diagram for Dy_2O_3-Y_2O_3-ZrO_2 at solidus/liquidus temperatures was not available, the author speculates that based on binary phase diagrams, the melting points of Dy-YSZ may be lower than 2750°C.[47,48] The similarity of powder production method and particle size distributions between 5YSZ and Dy-YSZ seems to rule out these two factors.

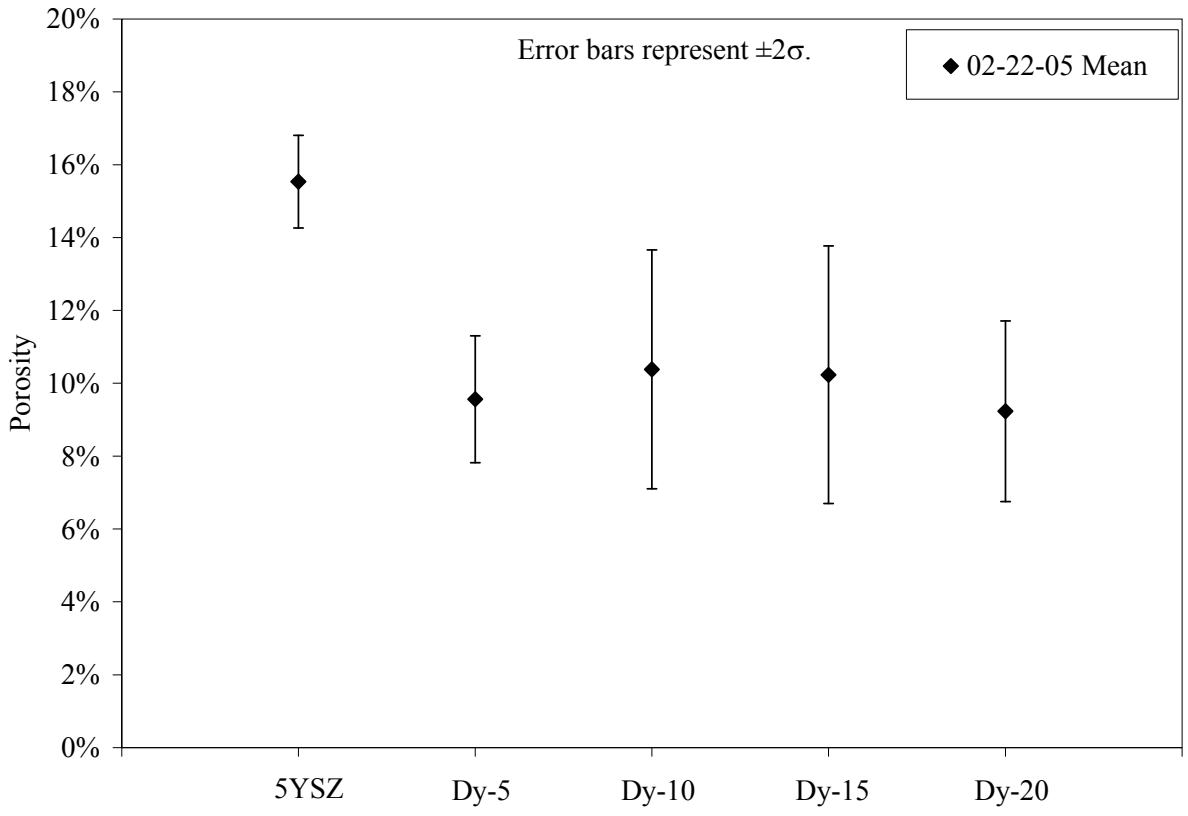

Figure 15: Measured porosity levels in as-sprayed coatings from batch 02-22-05

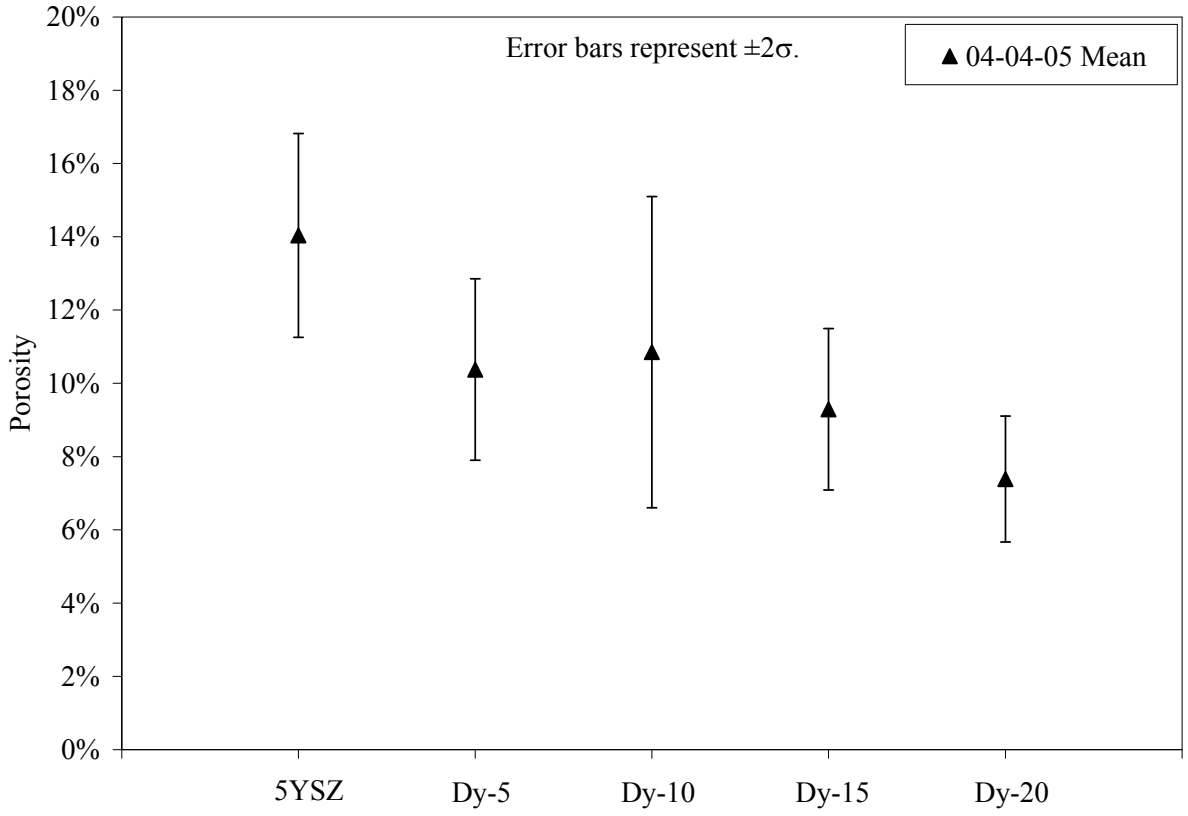

Figure 16: Measured porosity levels in as-sprayed coatings from batch 04-04-05

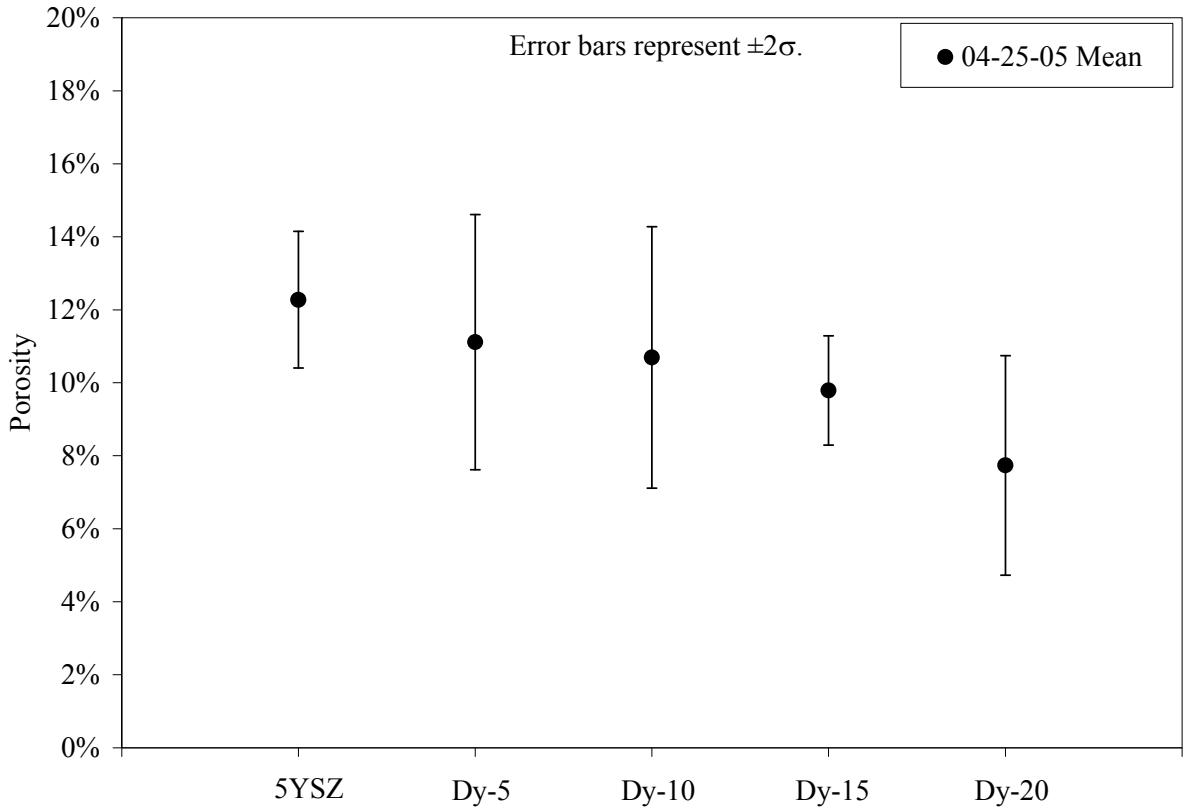

Figure 17: Measured porosity levels in as-sprayed coatings from batch 04-25-05

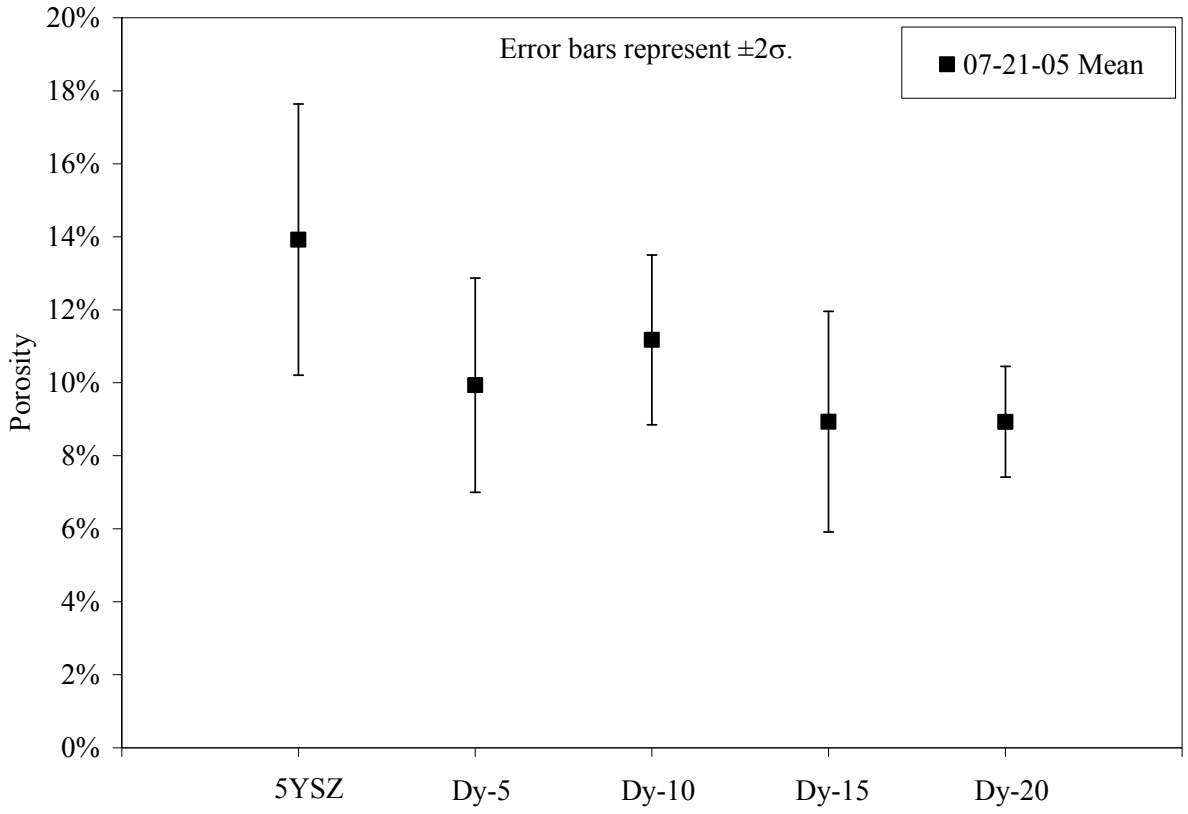

Figure 18: Measured porosity levels in as-sprayed coatings from batch 07-21-05

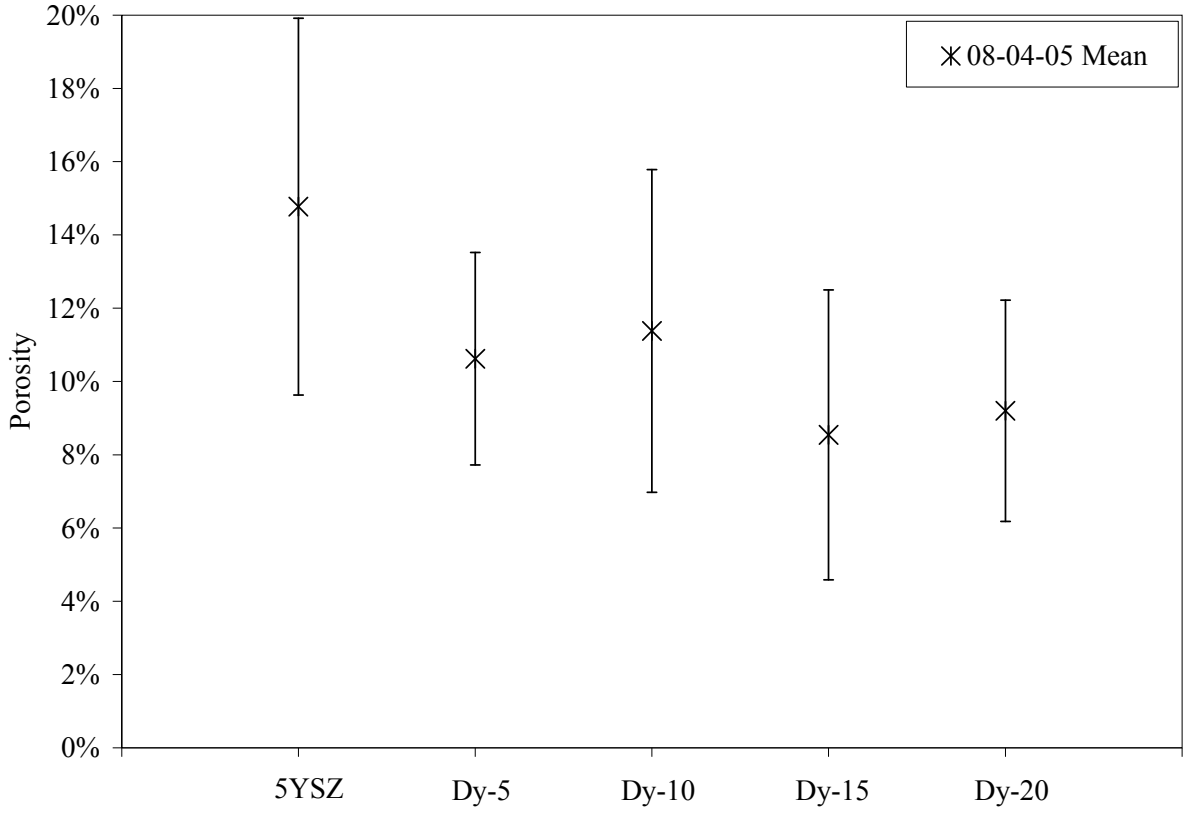

Figure 19: Measured porosity levels in as-sprayed coatings from batch 08-04-05

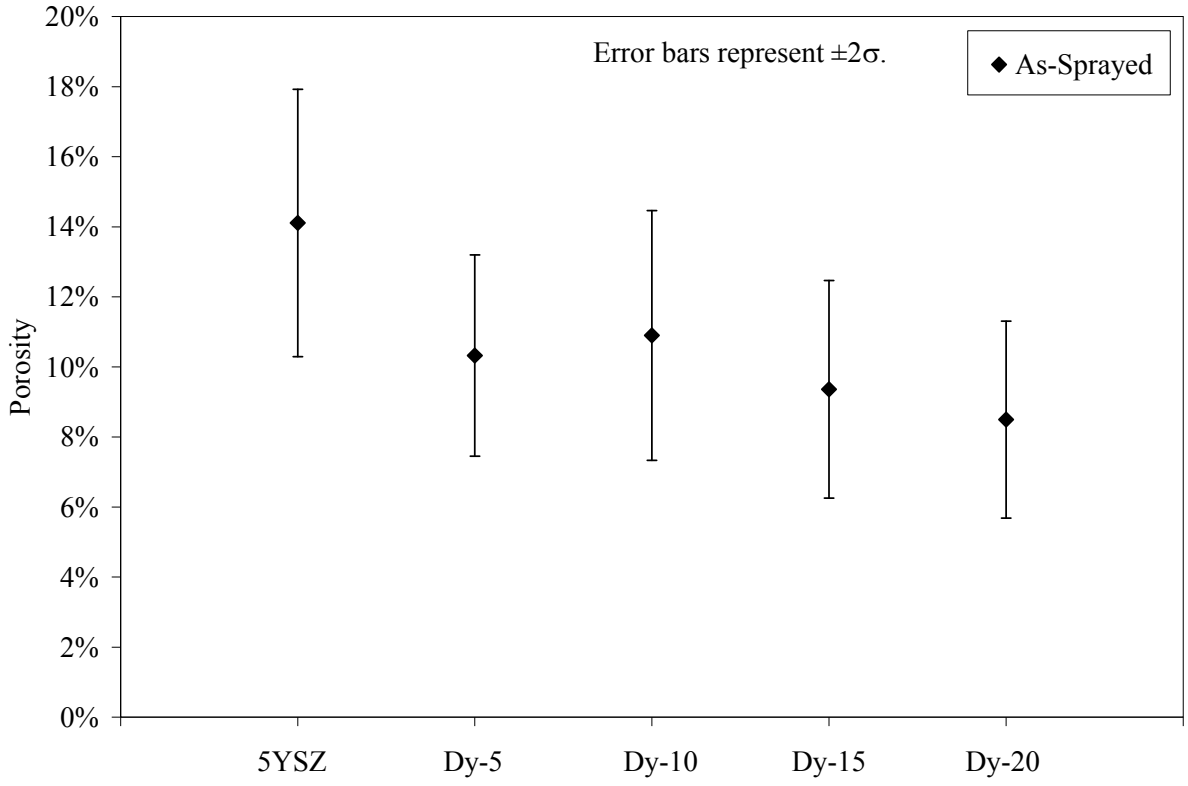

Figure 20: Overall measured porosity levels for as-sprayed coatings; averages and standard deviations were derived from the entire data set

4.3 Thermal Diffusivity and Specific Heat Data for As-sprayed Coatings

Measurement procedures as described in section 3.3 were executed by NRC-IMI in Quebec. The APS batch dates, measurement dates, and useable results are listed in Table 15. The sample coatings were not uniformly smooth and constant in thickness due to the APS process, thus a certain level of error was expected. Moreover, other defects such as transverse cracks were not entirely avoidable, thus some samples were found to be useless for diffusivity study at IMI. Transverse cracks (i.e. through-thickness) can cause measured diffusivity to be much higher than expected.

For the batches measured on 05-24-05, the samples were too thin and/or cracked transversely and no data for diffusivity was collected. For the batches measured on 10-14-05, the samples for DSC may have been contaminated with graphite and the c_p results exhibited no correlation to

dopant concentration. Due to time constraints in research schedule, no further samples were produced after 08-04-05.

Thermal diffusivity and specific heat measurement results are plotted in Figures 21-22. The relatively small number of data points and large variance certainly diminish the statistical significance of the absolute value of averages. However the visible trend, where a minimum is reached between 10-20 mol% total dopant concentration, is expected to influence the behaviour of thermal conductivity. Indeed the overall thermal conductivity exhibits the same trend, consistent with several published studies. The details are discussed in the next section.

The absolute value of averages (α and c_p) can now be tested against literature data to verify their usefulness. For dense nanocrystalline YSZ, Raghavan *et al* reported c_p values of 500-520 $J \bullet kg^{-1} \bullet K^{-1}$ at 100°C.[15] For dense YSZ co-doped with Ta_2O_5 or Nb_2O_5, where total dopant concentration was up to 20 mol%, Raghavan *et al* found that c_p varied between 435-515 $J \bullet kg^{-1} \bullet K^{-1}$ at 100°C, whereas α was in the range of 5.8-7.1x10^{-7} m^2/s.[49] Brandt *et al* reported c_p data in the range of 460-480 $J \bullet kg^{-1} \bullet K^{-1}$ for several APS YSZ at 300K.[26] Schwingel *et al* reported α values between 1.5-5.0x10^{-7} m^2/s for numerous YSZ samples produced by different APS equipment at different locations in western Europe.[50] R. E. Taylor reported α data for APS YSZ as 3.7x10^{-7} m^2/s.[51] Brandon and Taylor showed that for 6-12 wt% APS YSZ, α was between 3.0-4.2x10^{-7} m^2/s at 200-300°C.[52]

Therefore the average c_p values in Figure 21 are considered to be lower than literature data. Average thermal diffusivity values in Figure 22 are considered to be in the same range as literature data.

Table 15: Diffusivity and specific heat sample matrix

APS Batch Date	Measurement Date	Measurement Results	
		Diffusivity	Specific Heat
02-22-05	03-08-05	✓	✓
04-04-05	05-24-05	✗	✓
04-25-05	05-24-05	✗	✓
07-21-05	10-14-05	✓	✗
08-04-05	10-14-05	✓	✗

(Useable data is indicated with check mark)

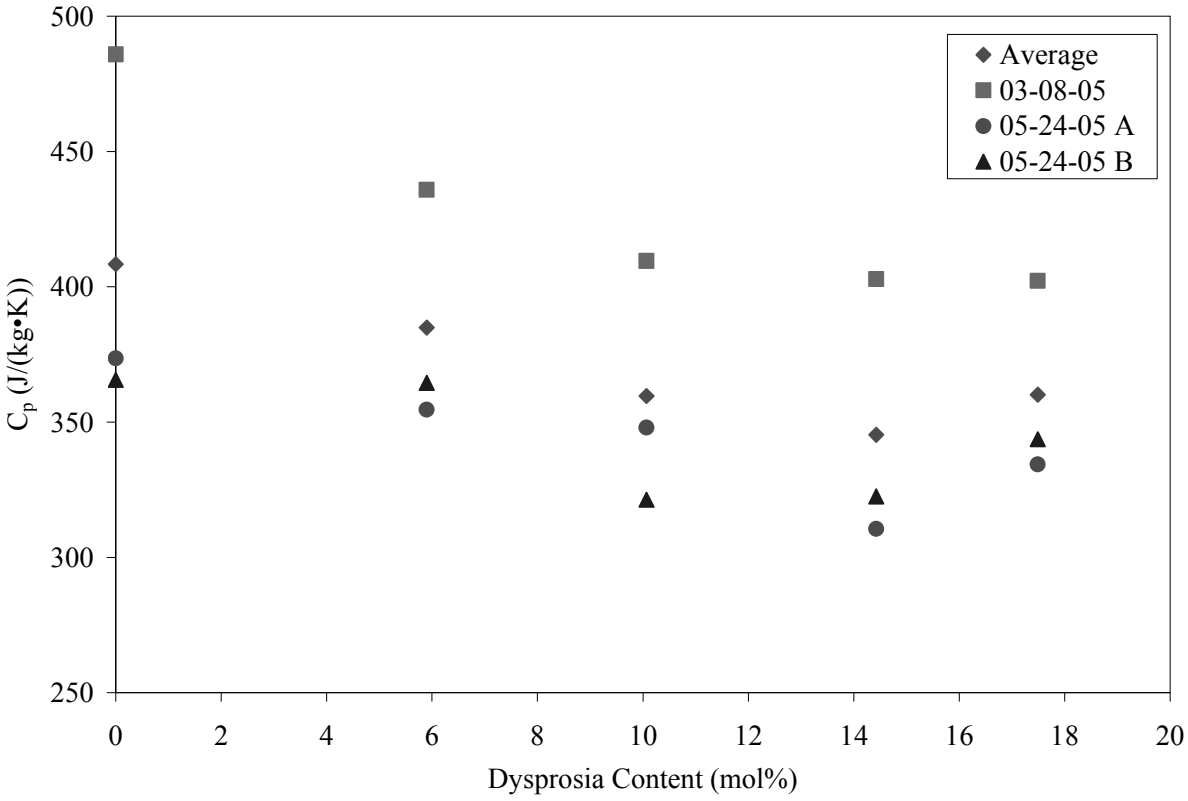

Figure 21: Specific heat measurement results for 5YSZ and Dy-YSZ

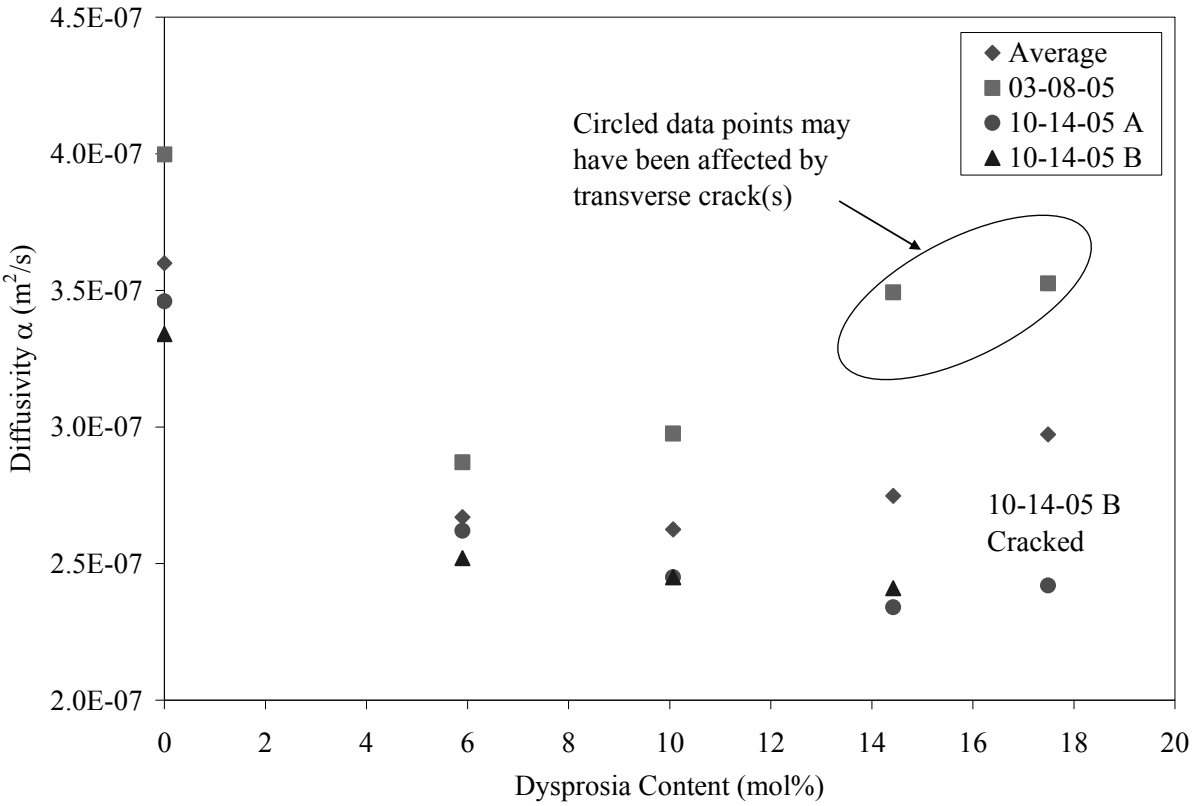

Figure 22: Thermal diffusivity measurement results for 5YSZ and Dy-YSZ

4.4 Thermal Conductivity Data and Model for As-sprayed Coatings

The measured average values of specific heat, thermal diffusivity, and coating porosity were combined along with estimated densities (Table 16) to arrive at thermal conductivities for each coating material via $\lambda = \alpha\rho c_p$. The densities were products of XRD and Rietveld refinement program where crystallographic unit cell volume and mass were estimated based on data fitting. It is clear that density of Dy-10 was underestimated, however 5YSZ density was within 20 kg/m^3 (0.3%) to that of 4.4 mol% YSZ single crystal reported by Bisson *et al*.[16] In Figure 23, it is clear that thermal conductivity of 5YSZ lied outside of the expected range of 0.8-1.0 $W \bullet m^{-1} \bullet K^{-1}$. Indeed all measured data points may have been underestimated due to the lower than expected c_p values. For example, if a typical value of 480 $J \bullet kg^{-1} \bullet K^{-1}$ was used for c_p then thermal conductivity of 5YSZ would be 0.90 $W \bullet m^{-1} \bullet K^{-1}$ and Dy-5 would be 0.77 $W \bullet m^{-1} \bullet K^{-1}$. The data in Figure 23 presents a minimum at around 10-15 mol% total dopant concentration (Dy + Y), considering that Dy-10 density should be higher than reported. This behaviour is consistent with single crystal data (Bisson *et al*), dense rare-earth doped zirconia (Wu *et al*), and APS coatings

(Zhu and Miller).[8,16,21] Thus it is very likely that this effect is directly related to trivalent dopant atoms and the creation of oxygen vacancies, both of which interfere with heat conduction by lattice waves. Higher dopant concentrations do not result in further lowering of thermal conductivity possibly due to long range ordering of oxygen vacancies. The model as described by equation 42 and its components was assembled with parameters shown in Table 17 in an attempt to verify theory against measured data. The data fitting parameters can be considered as equal to those used by Wu *et al*. Physical parameters for zirconia are average values for pure zirconia, where the Grüneisen anharmonicity parameter γ^2 and shear modulus μ were referenced from Wu *et al*. Most of the radiative component data, except coating thickness L, was referenced from P. G. Klemens.[34] The coating defect distribution and geometric parameters (ellipsoid axes a_3 and a_1) were best estimates derived from SEM micrographs. Actual measured average porosities from section 4.2, and measured compositions of yttria and dysprosia from section 3.1 were used in the model. In particular, the data fit parameters, universal constants, and physical parameters for zirconia from Table 17 were entered into equations 12, 15-23, and 24-25. The radiative component parameters from Table 17 were entered into equations 26-27. The defect distribution and geometric parameters from Table 17 were entered into equations 30-38.

Now the components within the model shall be verified against published literature data.

Intrinsic thermal conductivity of fully dense zirconia (porosity <1%) with no stabilizer was reported by Mevrel *et al*, Raghavan *et al*, and Bisson *et al*, to be in the range of 6.5-8.2 $W \bullet m^{-1} \bullet K^{-1}$.[15,16,17] The model predicted 7.48 $W \bullet m^{-1} \bullet K^{-1}$ and was within the range of published data.

Raghavan *et al* reported that thermal conductivity for dense 4.2-4.5 mol% YSZ was in the range of 2.0-2.2 $W \bullet m^{-1} \bullet K^{-1}$ at 100°C.[15,49] Schlichting *et al* reported 1.8 $W \bullet m^{-1} \bullet K^{-1}$ at room temperature for dense 4.5mol% YSZ.[13] The model predicted 2.53 $W \bullet m^{-1} \bullet K^{-1}$ for 4.5mol% YSZ at room temperature and 2.40 $W \bullet m^{-1} \bullet K^{-1}$ at 100°C (radiation effects were not included). Thus in this case the model overestimated published data. Doping with a more massive atom such as Gd (in gadolinia) instead of yttrium, Wu *et al* reported respective values for 7.5 and 15.5 mol% Gd stabilized zirconia as: 1.6 and 1.8 $W \bullet m^{-1} \bullet K^{-1}$ at room temperature, 1.7 and 1.6 $W \bullet m^{-1} \bullet K^{-1}$ at 300°C, and 1.7 and 1.5 $W \bullet m^{-1} \bullet K^{-1}$ at 700°C.[21] Utilizing only Dy atoms as dopant in the model with no radiation effects, the predictions for 7.5 and 15.5 mol% Dy stabilized zirconia were: 1.93

and 1.22 W•m^{-1}•K^{-1} at room temperature, 1.83 and 1.31 W•m^{-1}•K^{-1} at 300°C, and 1.88 and 1.42 W•m^{-1}•K^{-1} at 700°C. Here in every case the model overestimated the value for 7.5 mol% and underestimated the value for 15.5 mol%. This trend is similar to the model predictions presented by Wu *et al* in the same paper, where radiation also was not considered.

Now the combination of dopant effects, rounded porosity, and radiation will be considered. Raghavan *et al* reported comprehensive experimental data for near-dense and porous 3.25 mol% YSZ at temperatures up to 1000°C. For instance, thermal conductivities of 90% dense YSZ were 2.3 W•m^{-1}•K^{-1} at 100°C, 2.25 W•m^{-1}•K^{-1} at 400°C, and 2.45 W•m^{-1}•K^{-1} at 800°C. While 79% dense YSZ was recorded at 1.65 W•m^{-1}•K^{-1} at 100°C, 1.7 W•m^{-1}•K^{-1} at 400°C, and 1.75 W•m^{-1}•K^{-1} at 800°C. For 3.25 mol% YSZ with 10% round porosity, the model predicted 2.39 W•m^{-1}•K^{-1} at 100°C, 2.20 W•m^{-1}•K^{-1} at 400°C, and 2.21 W•m^{-1}•K^{-1} at 800°C. For 21% rounded porosity, the model predicted 1.96 W•m^{-1}•K^{-1} at 100°C, 1.80 W•m^{-1}•K^{-1} at 400°C, and 1.81 W/-mK at 800°C. The largest difference was about 19% for 79% dense YSZ at 100°C, all other values were within 10% of published data. Schlichting *et al* reported thermal conductivity data against temperature for 3 mol% YSZ with 6% porosity: 2.75-2.9 W•m^{-1}•K^{-1} at 100°C, 2.4-2.5 W•m^{-1}•K^{-1} at 400°C, and 2.1-2.3 W•m^{-1}•K^{-1} at 800°C.[13] For 3 mol% YSZ with 6% rounded porosity, the model predicted 2.63 W•m^{-1}•K^{-1} at 100°C, 2.40 W•m^{-1}•K^{-1} at 400°C, and 2.40 W•m^{-1}•K^{-1} at 800°C. Again, all predictions were within 10% of published data.

To consider the full model including non-rounded porosity such as interlamellar cracks, a comparison against literature data on APS TBC is needed. For 4.14 mol% YSZ sprayed with APS using AS powder, Kulkarni *et al* reported thermal conductivity value of 1.4 W•m^{-1}•K^{-1} at 12% porosity, and about 0.95 W•m^{-1}•K^{-1} at 19% porosity at room temperature.[25] Porosity in this paper included both interlamellar and globular pores. Assuming interlamellar crack vs. rounded porosity distribution of 70/30%, the full model predicted 1.45 W•m^{-1}•K^{-1} at 12% porosity and 1.04 W•m^{-1}•K^{-1} at 19% porosity. The difference from Kulkarni *et al* was less than 10%. Wang *et al* presented 0.9 W•m^{-1}•K^{-1} at room temperature for APS 3.4-4.5 mol% YSZ using AS powder. The FEM model used by Wang *et al* was based on Fourier's equation for heat flux, and the porosities were idealized spheroidal elements with different aspect ratios for cracks, voids, and pores. The FEM model prediction was about 1.7 W•m^{-1}•K^{-1} based on 15% total porosity in which the component for cracks was 2.3%, 3.8% for pores, and 8.9% for voids.[27] Utilizing the model in the current study, for 4.5 mol% YSZ at room temperature with 15% total porosity and

crack/pore ratio of 15.3/84.7%, the output data was 1.72 $W \cdot m^{-1} \cdot K^{-1}$. However if the input data for crack/pore ratio was a more reasonable 70/30%, then the model output improves to 1.22 $W \cdot m^{-1} \cdot K^{-1}$. In reality, the true effect of interlamellar cracks vs. porosity is difficult to ascertain. Nevertheless one can envision that the spaces between splats in APS coatings are more influential in reducing heat conduction since their major axes are perpendicular to the direction of heat flow. Moreover the number of layers of splats is large. Rounded porosity, due to its geometric shape, would not be as effective.

Full model output data is plotted in Figure 24 against measured data. For experimental values up to Dy-10 the trend is similar to model predictions. The magnitude of experimental values in this region was lower than expected, due to reasons as discussed at the beginning of this section. For dopant levels beyond Dy-10, the trend of model and experimental data become opposite since the model cannot account for any long range oxygen vacancy ordering effects. Note that at any given total dopant concentration, the model predicted lower thermal conductivities for using dysprosia plus yttria rather than yttria alone, and the improvement is significant at Dy-10. The model suggests that oxygen vacancies and point defects reduce the intrinsic thermal conductivity of zirconia by 30% or more. From literature data verification, it can be concluded that the model components are reasonably effective and the overall model is relatively accurate (considering 10-20% error) in predicting thermal conductivities for dysprosia-yttria-zirconia system up to 15 mol% total dopant. Therefore, further work is needed to improve both the accuracy and precision of measured thermal conductivity data.

Table 16: Densities as estimated by XRD (kg/m^3)

5YSZ	Dy-5	Dy-10	Dy-15	Dy-20
6024	6707	6709	7302	7473

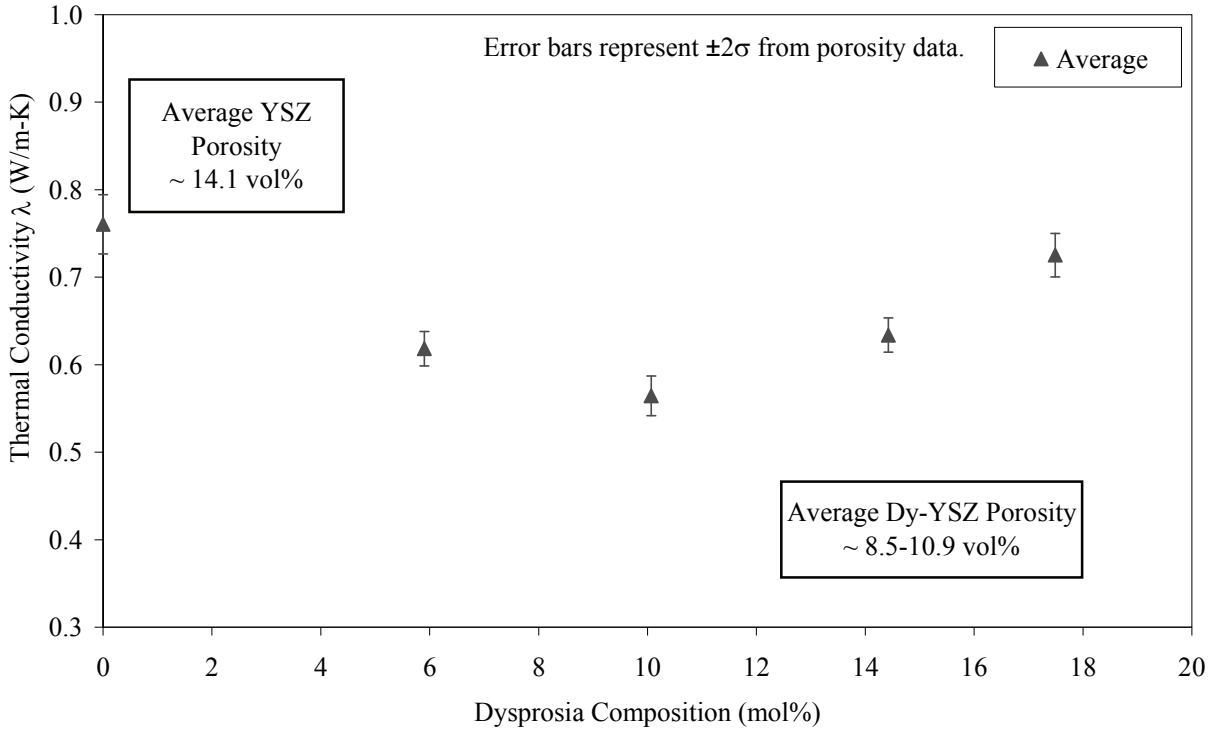

Figure 23: Thermal conductivity as calculated from measured data $\lambda = \alpha\rho c_p$; α taken from laser flash results, c_p taken from DSC results, ρ as estimated from XRD

Table 17: Thermal conductivity model parameters

Data Fit Parameters		Universal Constants		
χ (intrinsic)	**ψ (point defects)**	**k_b ($m^2 \cdot kg \cdot s^{-2} \cdot K^{-1}$)**	**σ ($W \cdot m^{-2} \cdot K^{-4}$)**	**c (m/s)**
0.51	1	1.381E-23	5.670E-08	2.998E+08

Physical Parameters for ZrO_2			Radiative Component Parameters			
a^3 (m^3)	**ρ (kg/m^3)**	**N ZrO_2**	**n (refractive)**	**Coating L (m)**	**J_4 ∞**	**h (J·s)**
1.167E-29	5.85E+03	3	2.7	4.25E-04	25.9758	6.626E-34
T_0 (K)	**γ^2 ZrO_2**	**μ (Pa)**	**Θ (K)**	**λ_{abs} (m)**	**f_a (Hz)**	
250	4	1.00E+11	2.88E+03	5.00E-06	6.00E+13	
Grain D (m)	**ν (m/s)**	**ω_D (Hz)**				
5.00E-07	4.136E+03	7.108E+13				

Defect Distribution and Geometric Parameters					
a_3 (m)	**a_1 (m)**	**Crack Fraction**	**Pore Fraction**		
5.00E-07	2.00E-05	0.7	0.3		
5YSZ	**Dy-5**	**Dy-10**	**Dy-15**	**Dy-20**	
14.11%	10.32%	10.90%	9.36%	8.50%	**Measured Average**
9.88%	7.23%	7.63%	6.55%	5.95%	**Interlamellar Crack Component**
4.23%	3.10%	3.27%	2.81%	2.55%	**Rounded Pore Component**

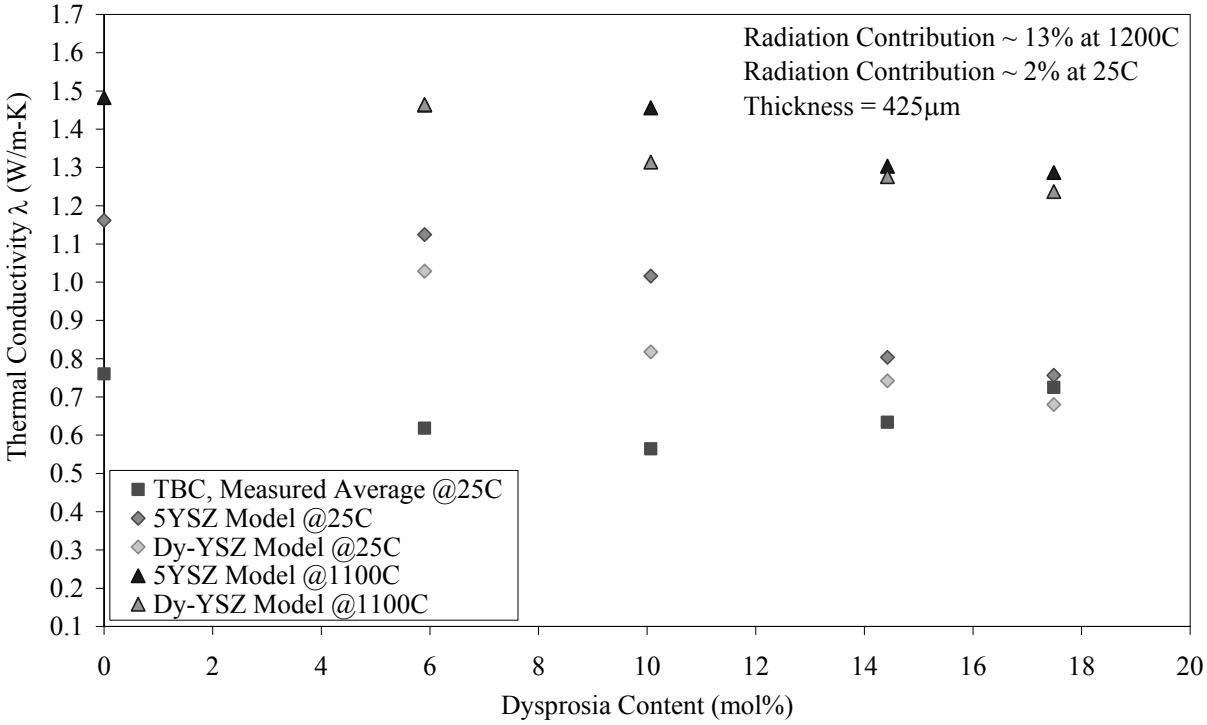

Figure 24: Thermal conductivity model plotted against measured data; model includes effects of point defects, grain boundaries, rounded porosity, interlamellar cracks, and radiation

4.5 Porosity Levels and Relative Densification in Thermally Cycled Coatings

Three (3) batches of each coating material were processed as per procedures in section 3.4 and Table 18 summarizes the number of cycles per trial. Visual inspection was performed at regular intervals (i.e. 1-2 times per day) to examine the quartz tubes for damage. Typically this took less than five (5) minutes, however in the 2nd and 3rd trials 1-3 quartz tubes had to be re-positioned or replaced per trial, thus lengthening trial time. In addition, in the 2nd trial the 5YSZ specimen fell out of thermal cycle apparatus due to quartz tube failure. Thus extra time had to be allocated for 5YSZ to complete (350) cycles, leading to an even longer trial time. Lastly, the 3rd trial was terminated prematurely at 274 cycles when considerable coating failure was noticed on Dy-10, Dy-15 and Dy-20 specimens.

Post-cycle specimens were mounted directly in Cold Cure epoxy, and the sections of interest were cut away by utilizing abrasive saw with coolant (Figure 25). The samples were polished

and again, image analysis per section 3.5 was performed. Representative post-cycle SEM micrographs are shown in Figures 26-27. Notice that porosity is generally rounded, and that interlamellar cracks either had begun or were nearly closed due to sintering activity. This was expected if one considers the residence time per cycle at 1085-1090°C to be five (5) minutes, then the total residence time were 29.1 hours (1st and 2nd trials) and 22.8 hours (3rd trial). Post-cycle mean values, standard deviations, and histograms are compared against those of as-sprayed coatings in Figures 28-36.

The standard deviation for post-cycle porosity data is mostly larger than as-sprayed data. This could be the result of sintering, which naturally tends to enhance the populations of cracks and pores at the two extremes in terms of size. This would occur at the expense of cracks and pores which lied near the centre of size distribution, in effect lengthening the two tails of distribution curve. Histogram comparison reveals clear indications, especially for 5YSZ and Dy-5, that the post-cycle coatings were significantly different from as-sprayed coatings. The significance can be statistically rated as high ($p = 0.01$ or 99% confidence) if one performs the Student's t-test as per equations 49-50 (two-sample assuming unequal variances, two tailed) followed by F-test for variance as per equations 51-52. t-test results showed that the differences in mean values were highly significant, and F-test results were not significant at $p = 0.01$ or 99% confidence, meaning that variance between data sets were not statistically significant (summarized in Table 19). If the post-cycle change in porosity level is normalized against initial level in as-sprayed coatings, then this relative densification can be plotted as in Figure 37. The values were 5YSZ: 35.7%, Dy-5: 30.0%, Dy-10: 26.0%, Dy-15: 23.6%. A clear trend emerges, where the increase in dysprosia content is likely a factor in the improvement of sintering resistance. The possible formation of lower melting point ternary eutectic(s), as speculated in section 4.2, should have resulted in poorer sintering resistance of Dy-YSZ. The fact that this was not the case may be contributed to increasing levels of oxygen vacancies, but the relative strengths and interactions between dysprosium ions, oxygen vacancies, and ternary eutectics in affecting sinter behaviour are unclear and further work is needed for clarification.

Table 18: Thermal cycle experiment matrix

APS Batch Date	Thermal Cycle Dates	Number of Cycles	Coating Thickness (μm)
09-20-05	09-20-05 to 09-27-05	350	~300
09-27-05	09-28-05 to 10-06-05	350	~200
10-12-05	10-12-05 to 10-19-05	274	~200

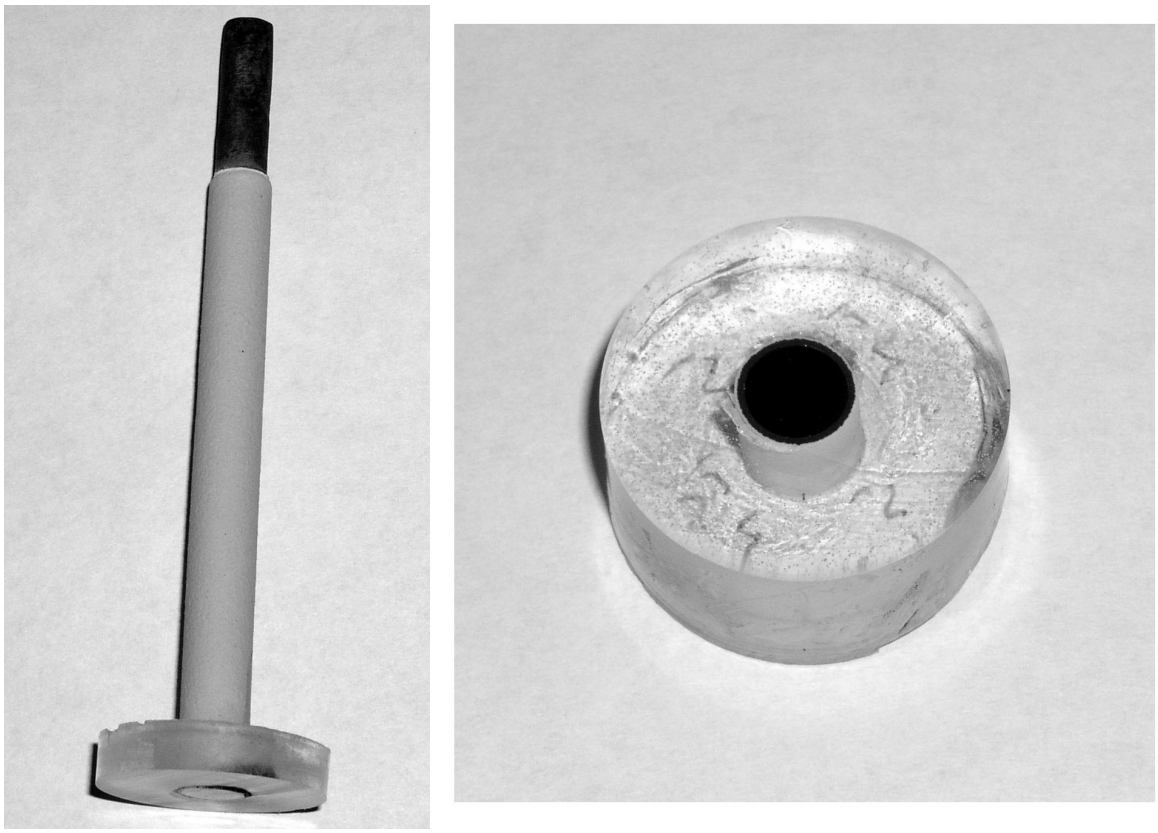

Figure 25: Post-cycle sample preparation for SEM analysis

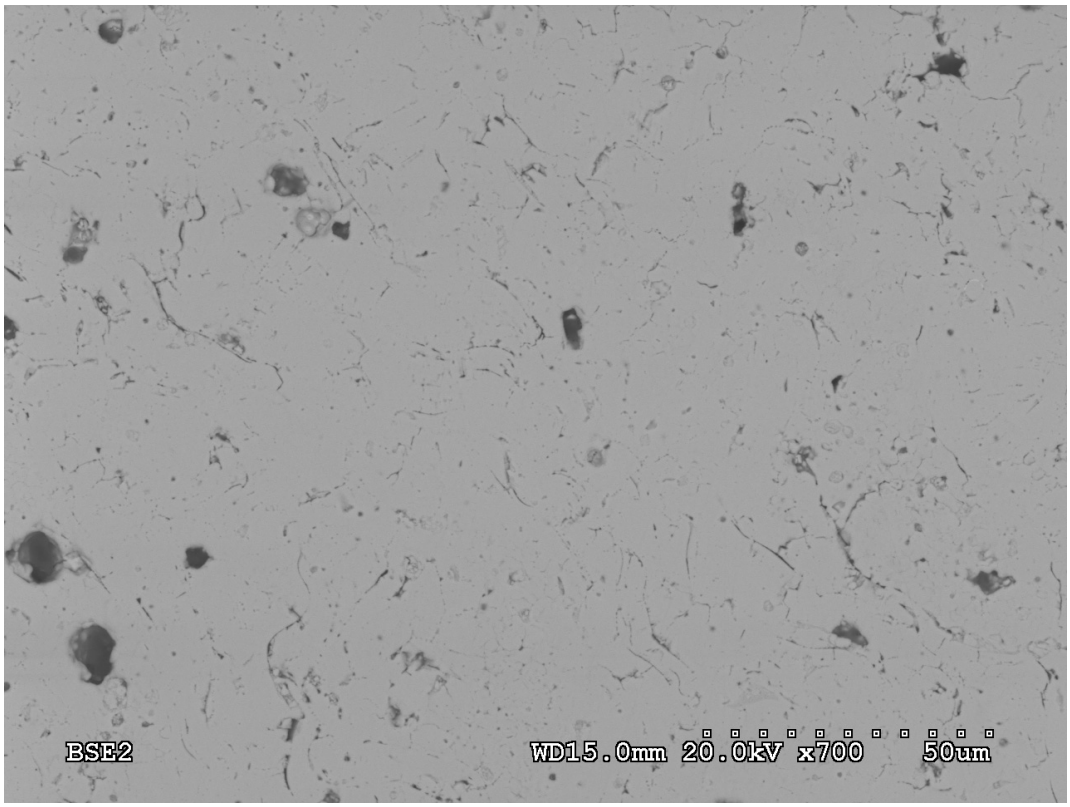

Figure 26: SEM micrograph of 5YSZ coating after thermal cycle (29.1 hours at 1085-1090°C)

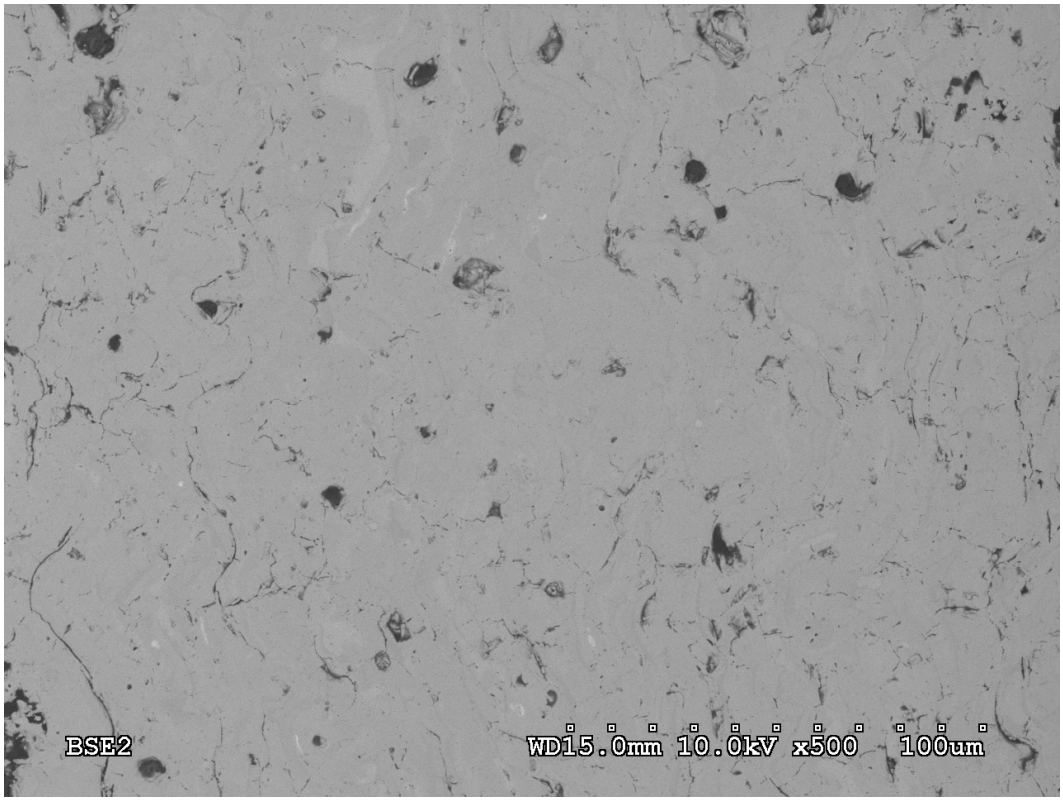

Figure 27: SEM micrograph of Dy-5 coating after thermal cycle (29.1 hours at 1085-1090°C)

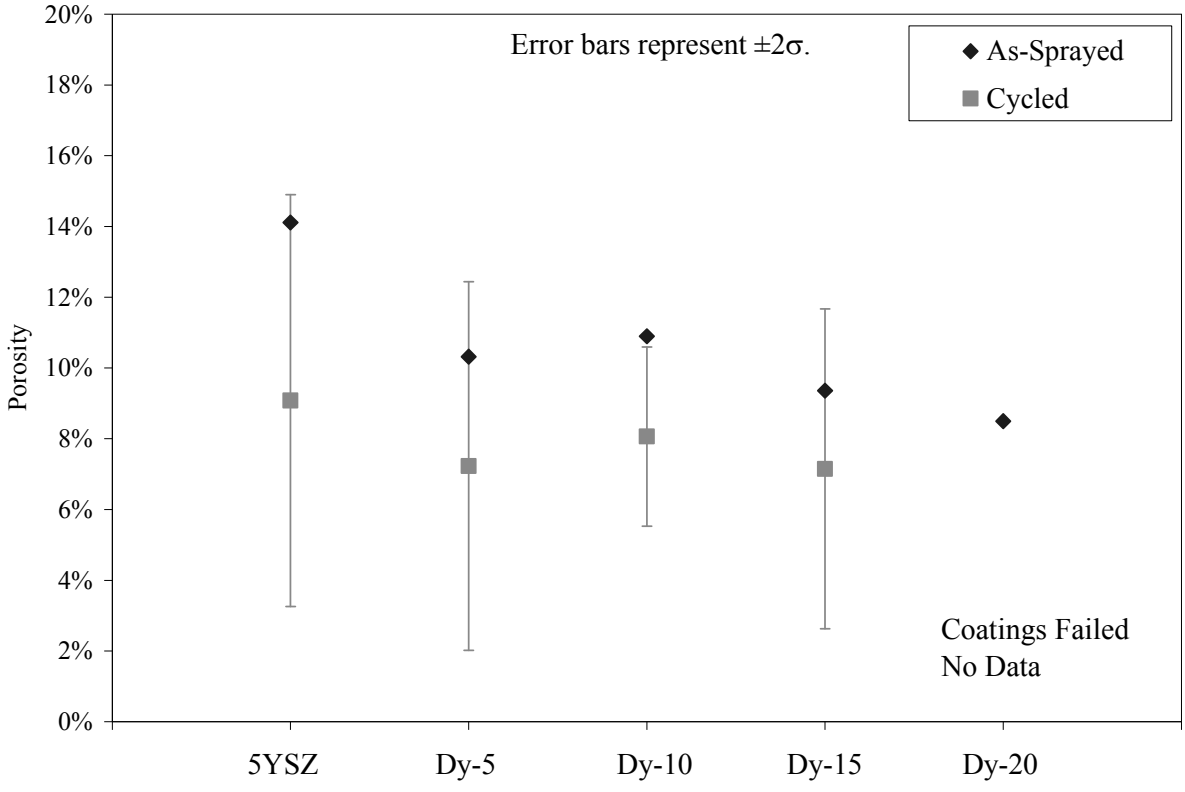

Figure 28: Overall measured porosity levels for thermally cycled coatings vs. as-sprayed coatings, error bars for as-sprayed data are not shown for clarity; averages and standard deviations were derived from the entire data set for each type of coating

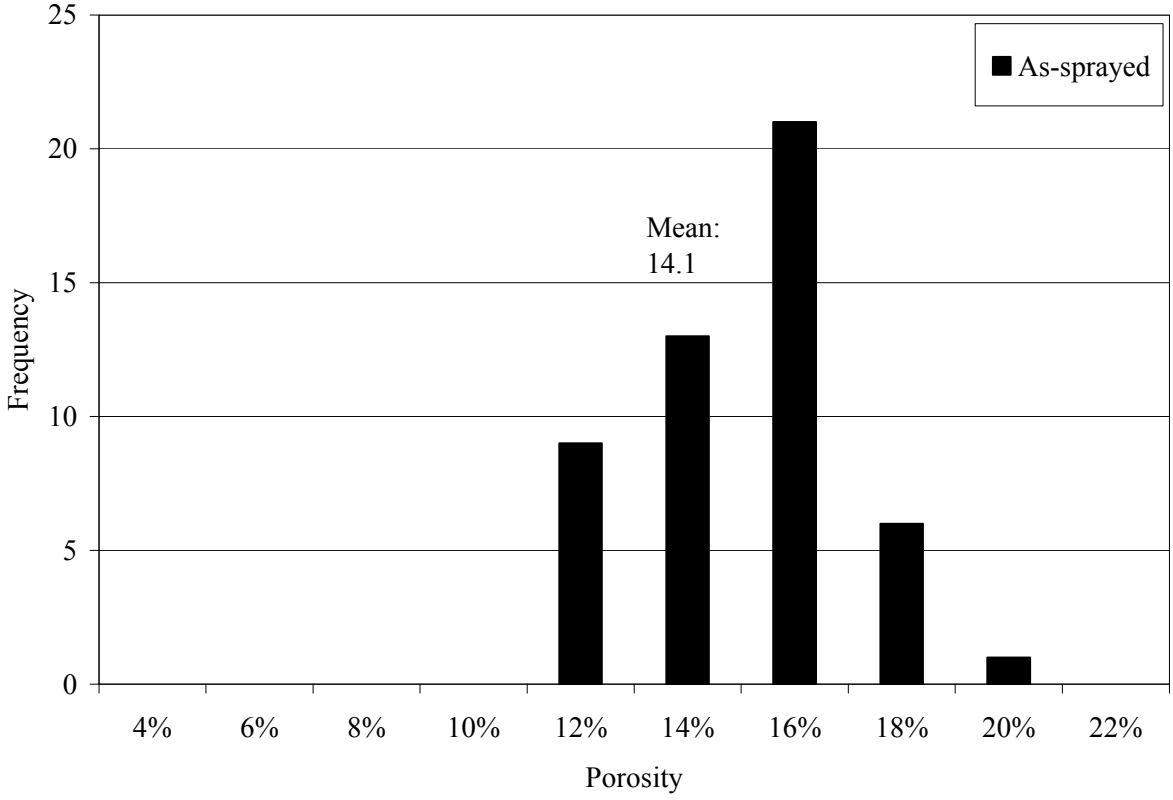

Figure 29: Porosity level histogram for 5YSZ as-sprayed coating; each column represents cumulative frequency in the preceding interval

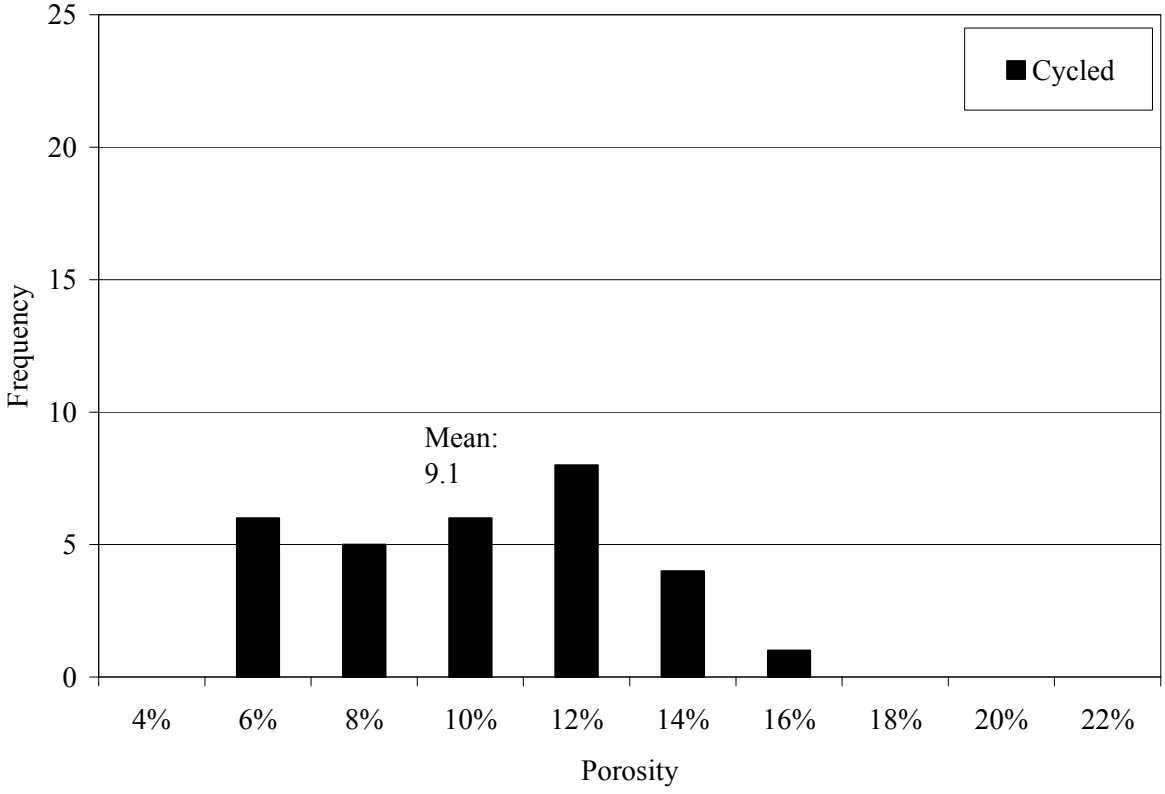

Figure 30: Porosity level histogram for 5YSZ cycled coating; each column represents cumulative frequency in the preceding interval

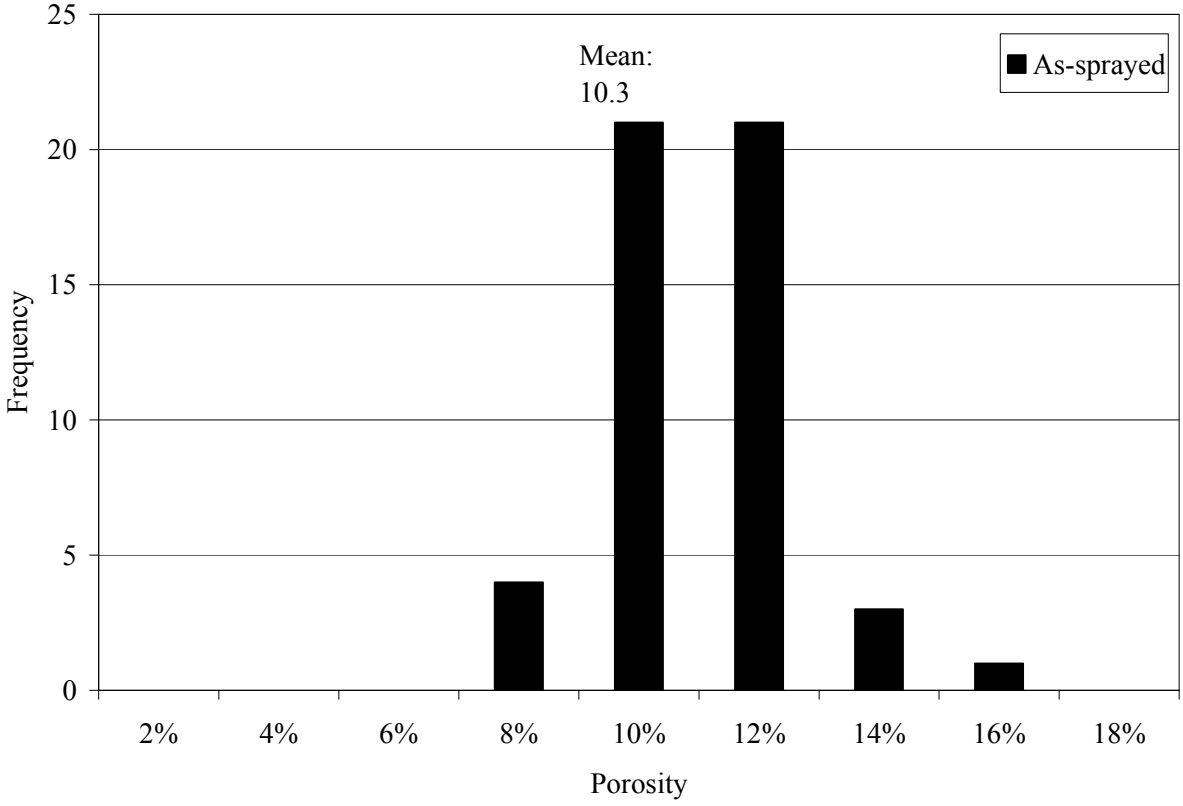

Figure 31: Porosity level histogram for Dy-5 as-sprayed coating; each column represents cumulative frequency in the preceding interval

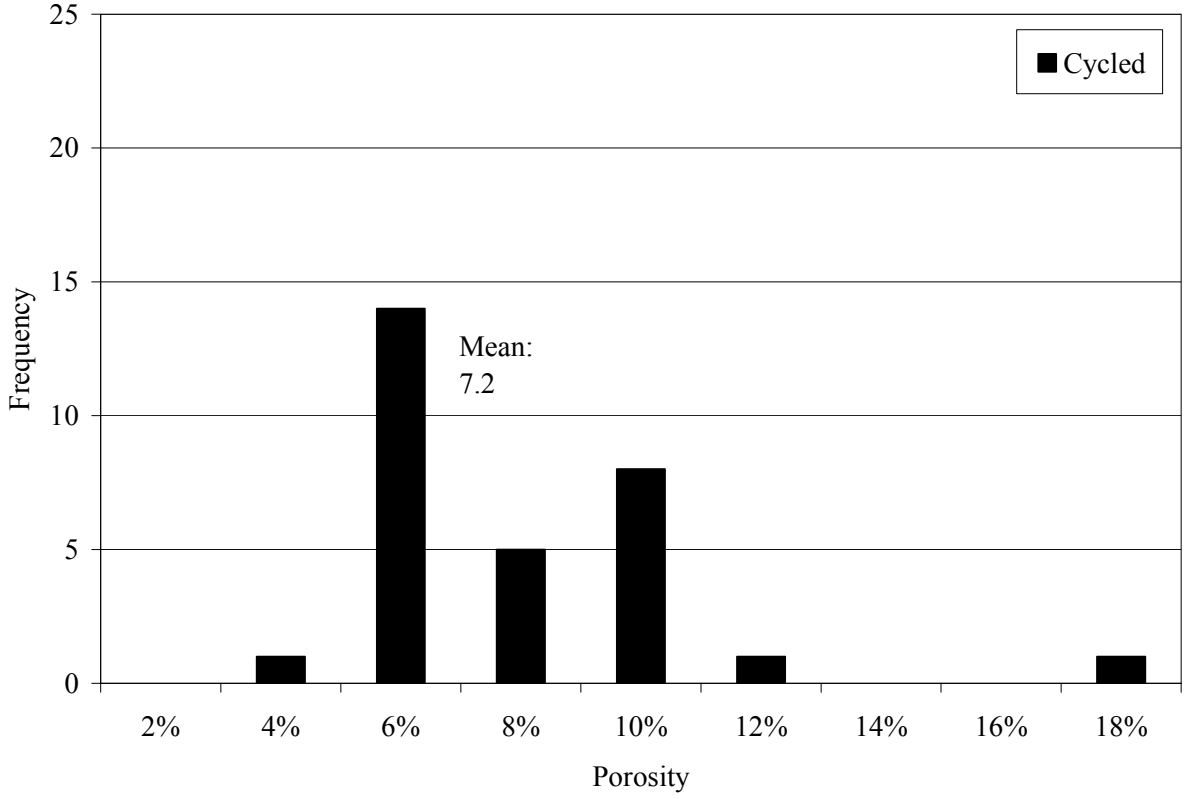

Figure 32: Porosity level histogram for Dy-5 cycled coating; each column represents cumulative frequency in the preceding interval

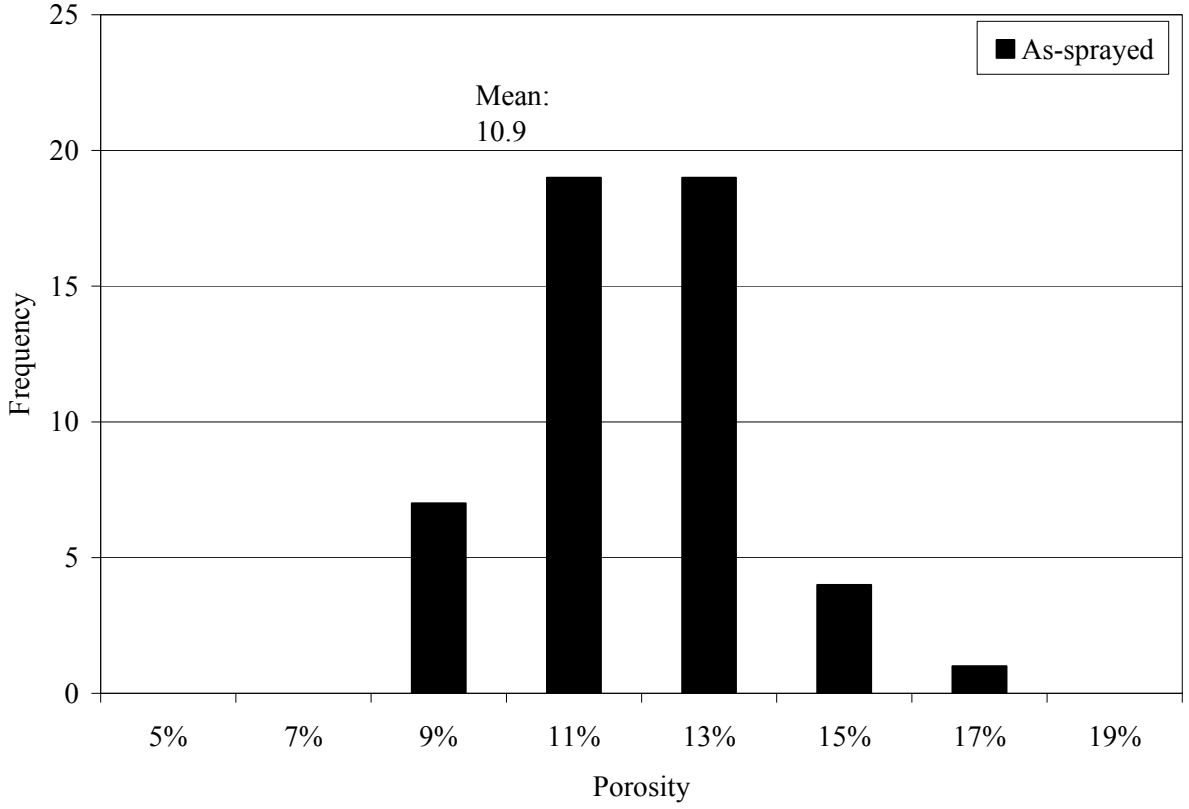

Figure 33: Porosity level histogram for Dy-10 as-sprayed coating; each column represents cumulative frequency in the preceding interval

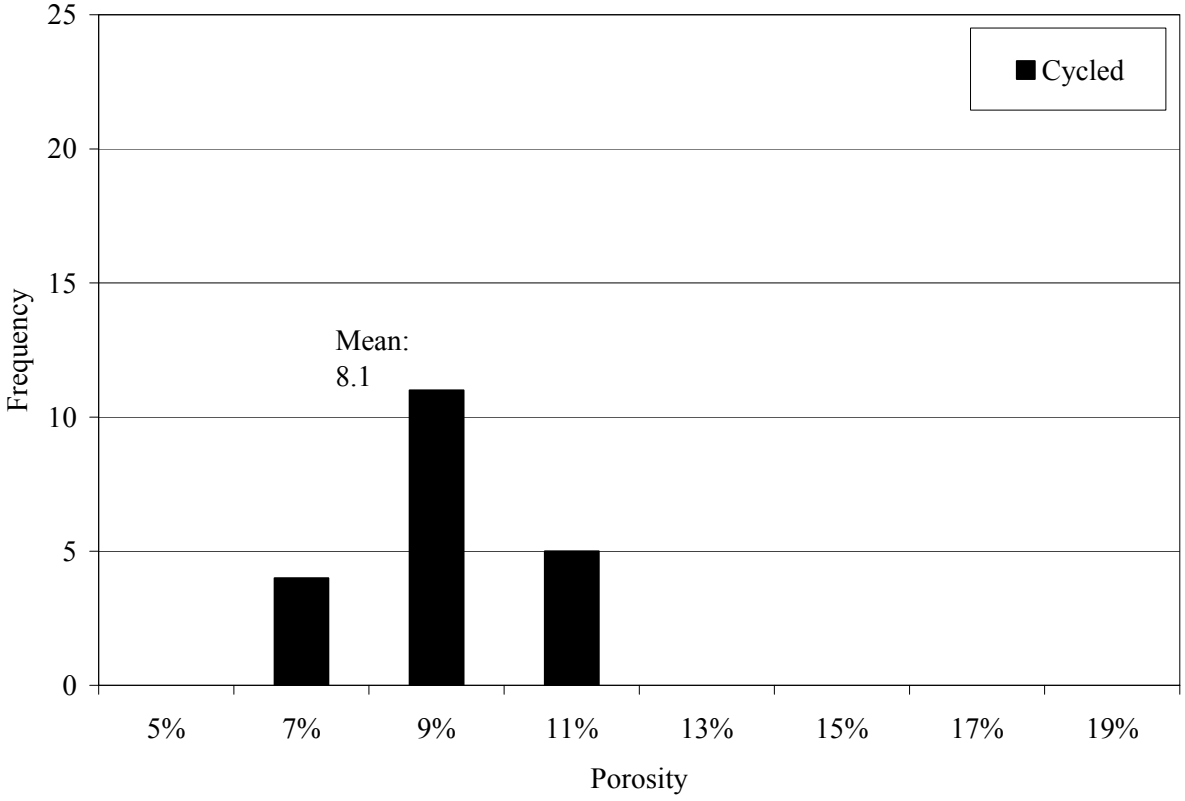

Figure 34: Porosity level histogram for Dy-10 cycled coating; each column represents cumulative frequency in the preceding interval

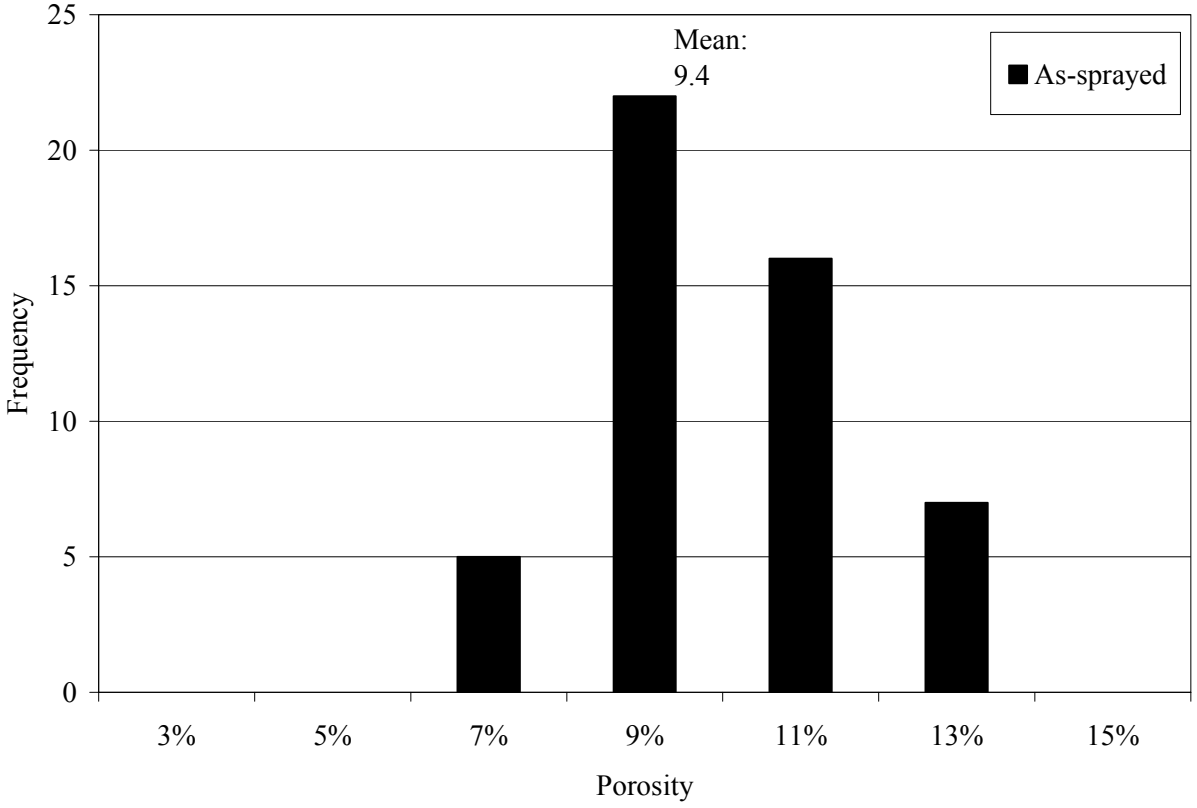

Figure 35: Porosity level histogram for Dy-15 as-sprayed coating; each column represents cumulative frequency in the preceding interval

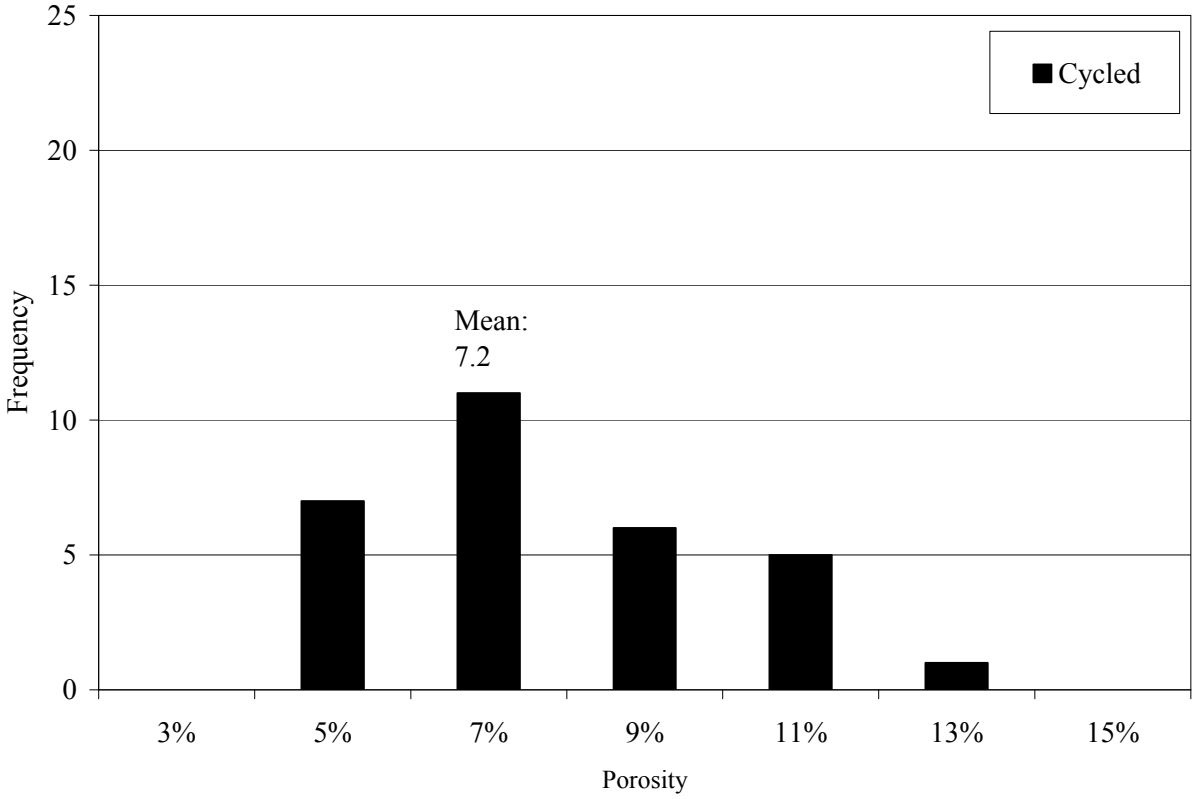

Figure 36: Porosity level histogram for Dy-15 cycled coating; each column represents cumulative frequency in the preceding interval

Table 19: Statistical analyses for as-sprayed and thermal cycled coating porosity data sets

Coating Grade	t-test		F-test	
	t Stat	t Critical (p=0.01)	F	F Critical (p=0.01)
5YSZ	8.38	2.70	0.43	0.47
Dy-5	6.34	2.71	0.33	0.47
Dy-10	7.37	2.69	1.97	2.79
Dy-15	4.50	2.70	0.46	0.47

(t-test null hypothesis: as-sprayed and cycled data means are equal; F-test null hypothesis: as-sprayed and cycled data variances are equal; t- or F-test value must exceed critical value in order to reject null hypothesis)

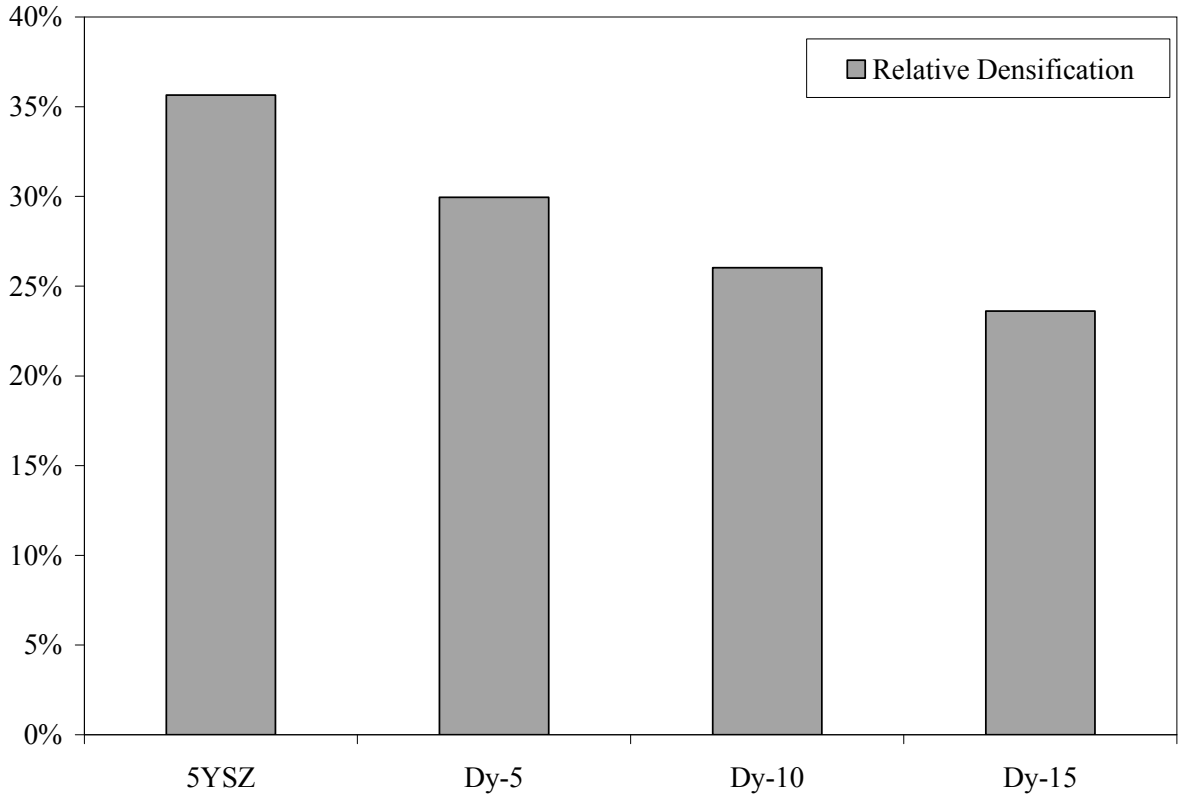

Figure 37: Relative densification of four coatings after thermal cycling (relative to as-sprayed structure)

4.6 Thermal Cycle Coating Performance

The three (3) trial specimens were also exhibited some trends in coating performance under cyclic thermal loading. Figures 38-40 illustrate the visual appearance of specimens immediately after completion of thermal cycling. Photos were taken of all areas with visually visible defects. In the 1st trial, Dy-5 was clearly the best performer, as all other coatings failed by spallation. Coating thickness was reduced for the 2nd trial, thus the end result was that 5YSZ, Dy-5, Dy-10, and Dy-15 performed similarly well with no spallation (discounting end effects). Dy-20 was the worst performer with one crack. For the last trial on CMSX-11B substrates, Dy-10, Dy-15, and Dy-20 all failed by spallation and the trial was stopped prematurely. At (274) cycles, Dy-5 appeared to have less cracking than 5YSZ, when end effects were ignored. As Figure 30 shows, 5YSZ coating contained three (3) major cracks at the lower portion of specimen, and two (2) minor cracks at the top portion. Dy-5 coating in this case had one (1) major crack at the centre and two (2) minor cracks at the lower portion of specimen. Note that in all cases, once the

specimens had dwelled at room temperature for >1 hour, Dy-15 and Dy-20 coatings always detached from bond coat and crumbled. The weakness of highly doped zirconia is consistent with results published by Jue *et al* where 2.6-8 mol% dense YSZ exhibited a decreasing trend in fracture strength and toughness with increasing yttria content.[53]

Based on these trials, it was concluded that Dy-5 and perhaps Dy-10 are worthy of further study. Dy-5 was indeed a better material than 5YSZ under cyclic thermal loading. These findings are similar to those for rare-earth doped YSZ as described by Zhu and Miller, where YSZ doped with Gd, Nd, Yb, etc. performed just as well as 4.55YSZ when the total dopant concentration was between 5-15 mol%.[8]

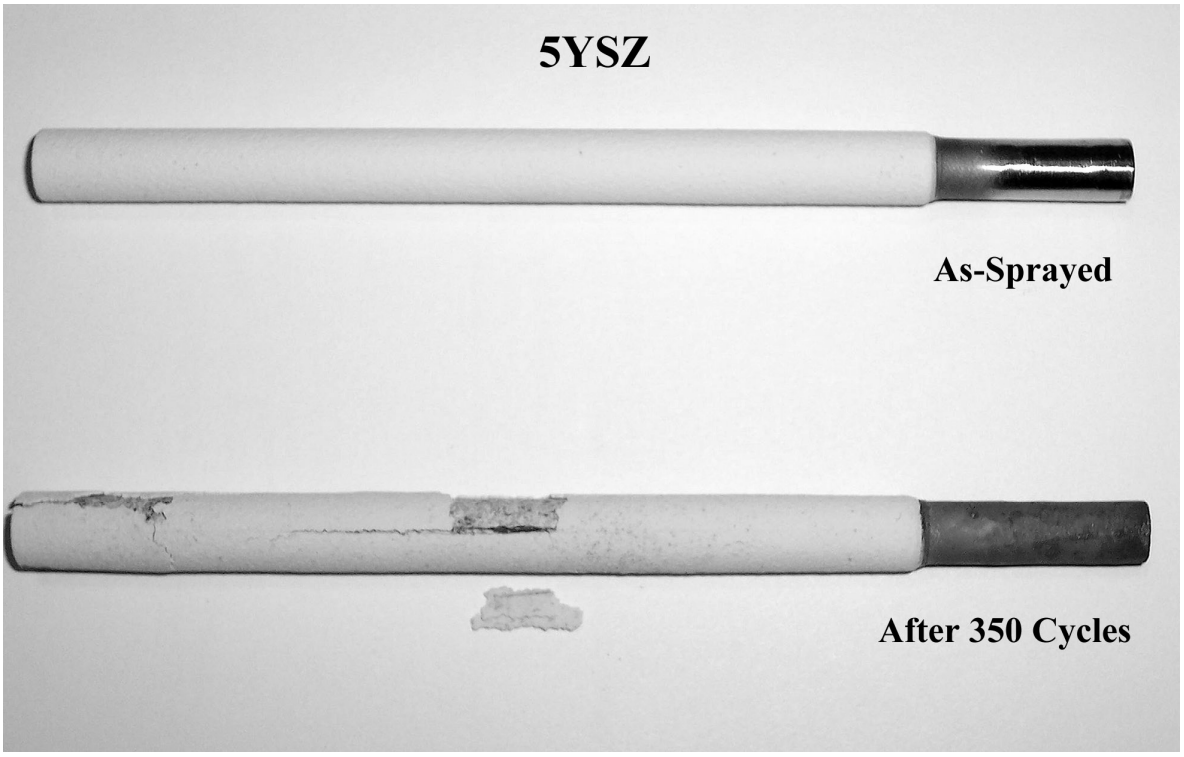


Dy-5
As-Sprayed
After 350 Cycles

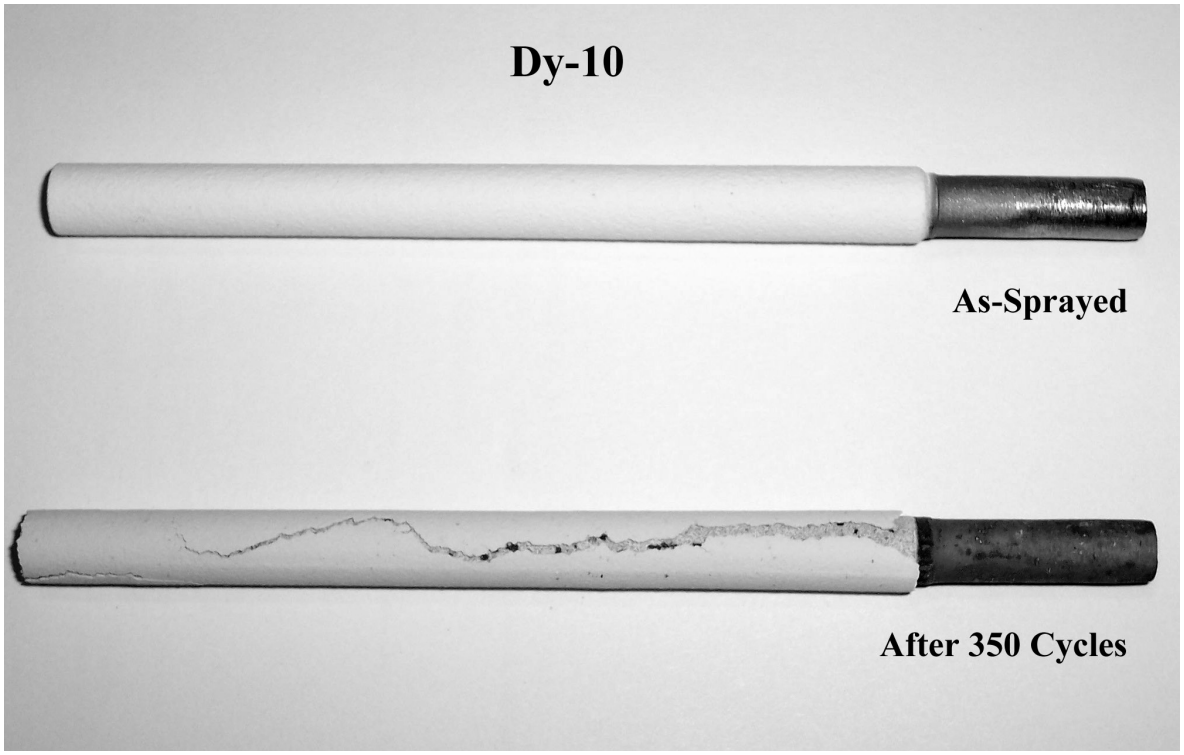
Dy-10
As-Sprayed
After 350 Cycles

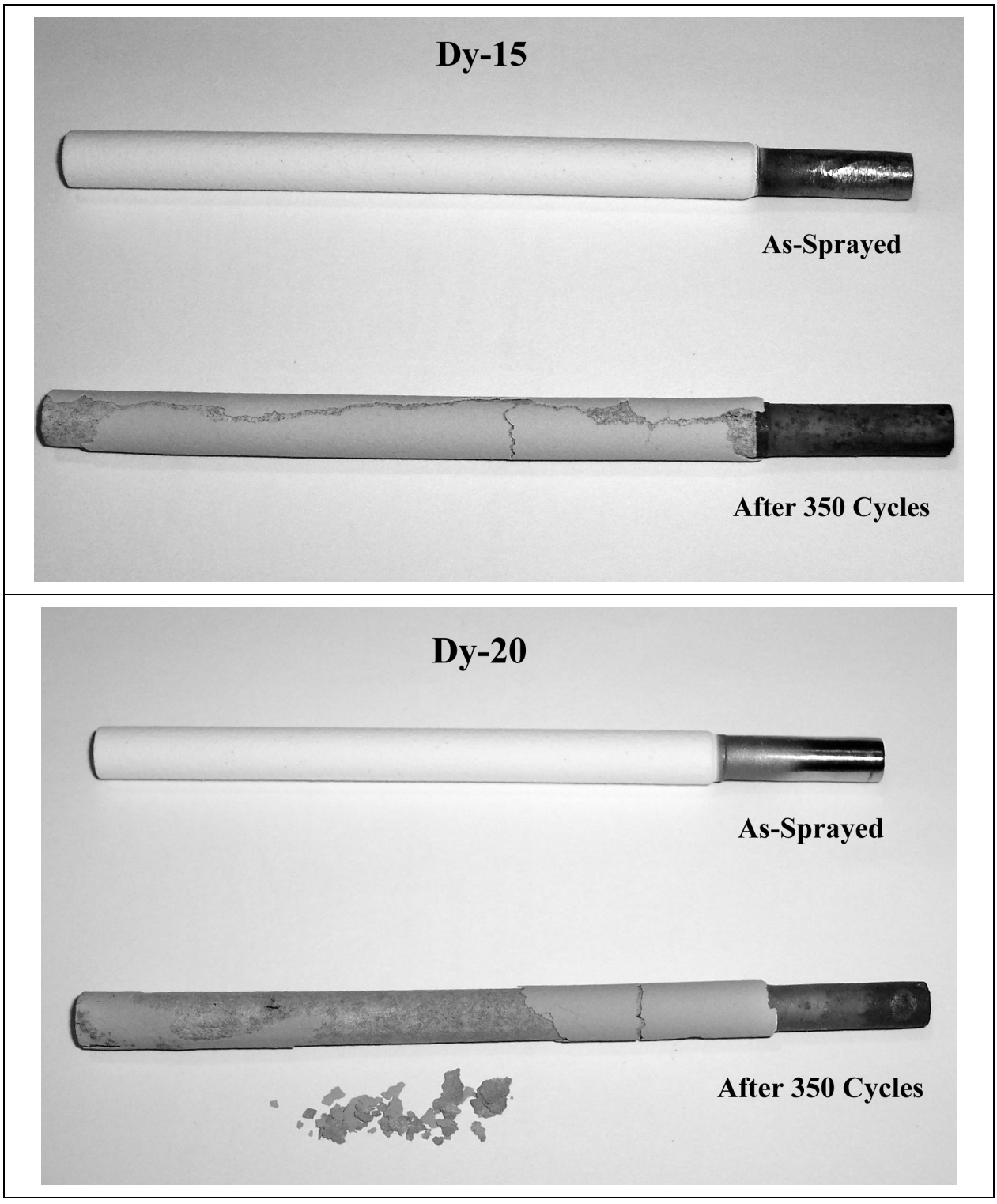

Figure 38: As-sprayed and thermal cycled rod specimens from 1st trial (Ni-based substrate); 350 cycles, coating thickness ~350 μm

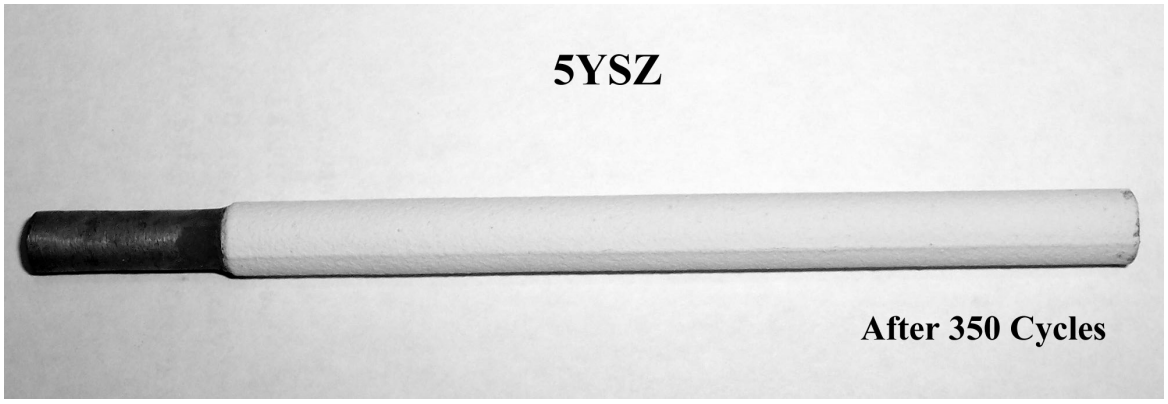
5YSZ
After 350 Cycles

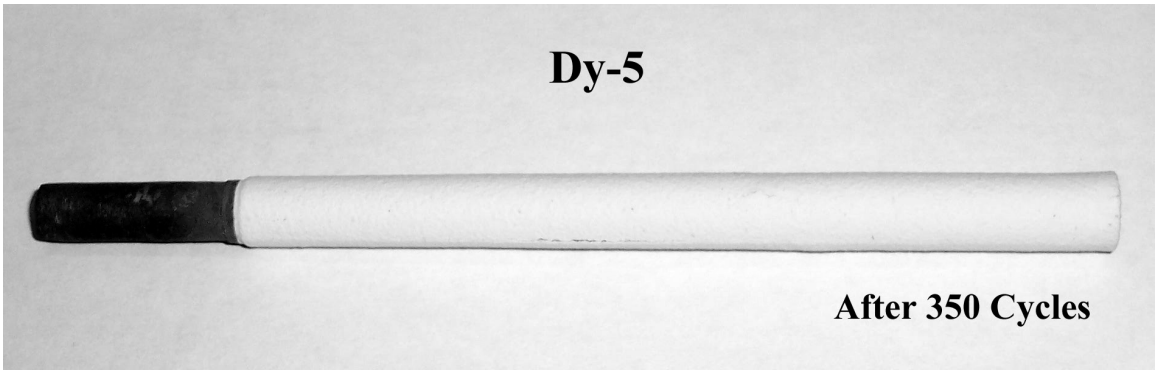
Dy-5
After 350 Cycles

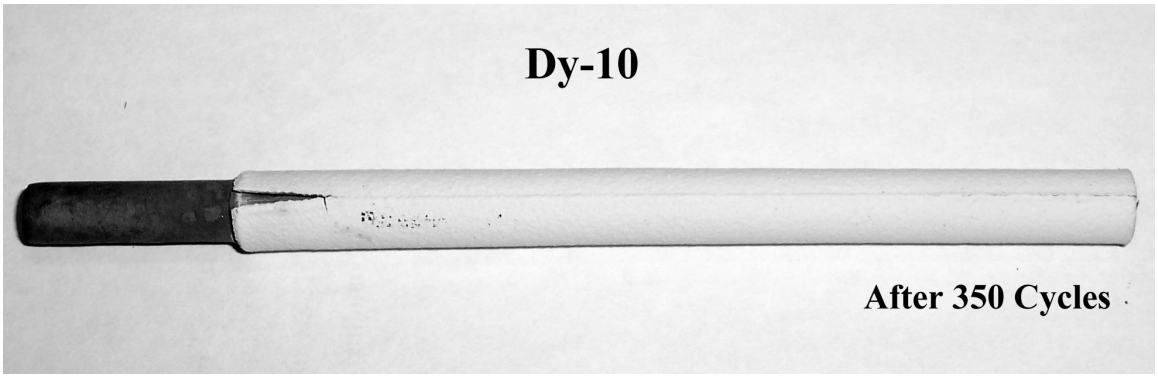
Dy-10
After 350 Cycles

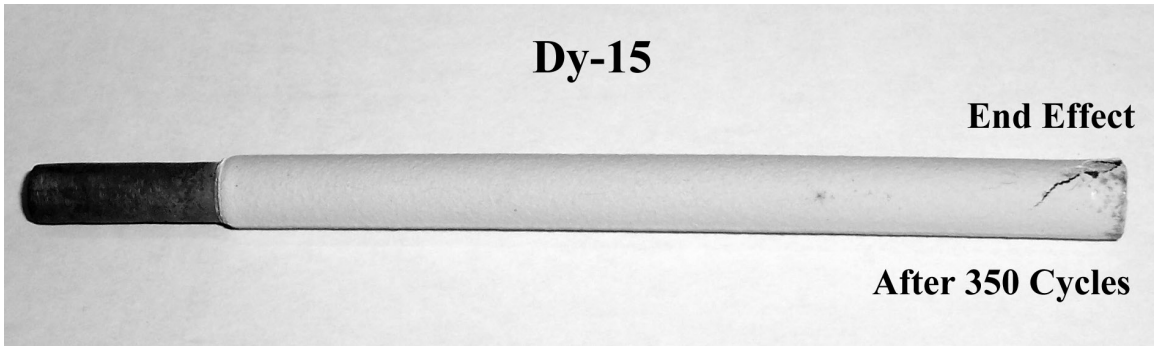
Dy-15
End Effect
After 350 Cycles

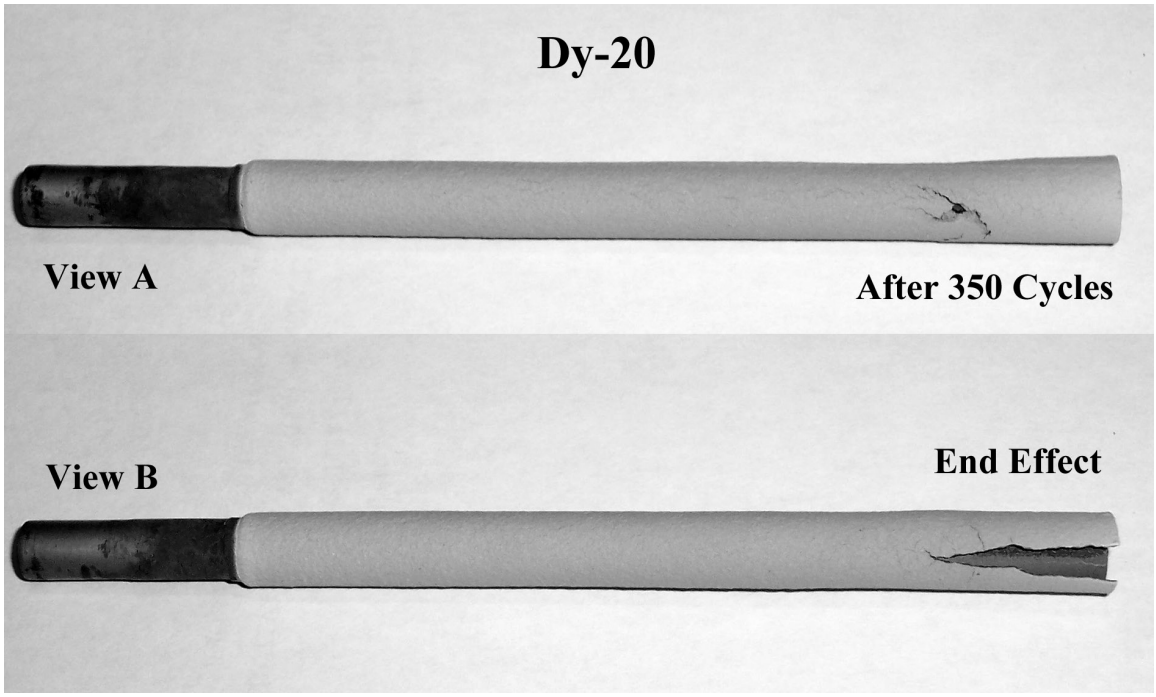

Figure 39: Thermal cycled rod specimens from 2nd trial (Ni-based substrate); 350 cycles, coating thickness ~200 μm

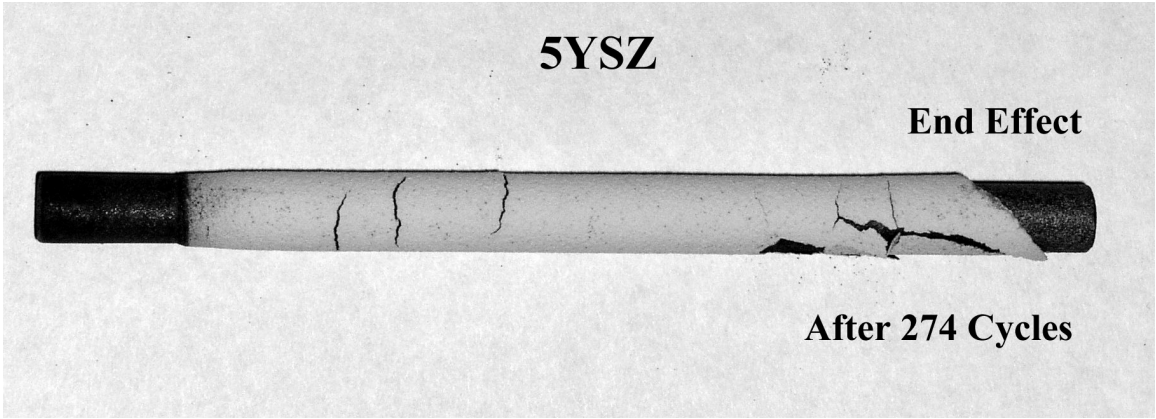

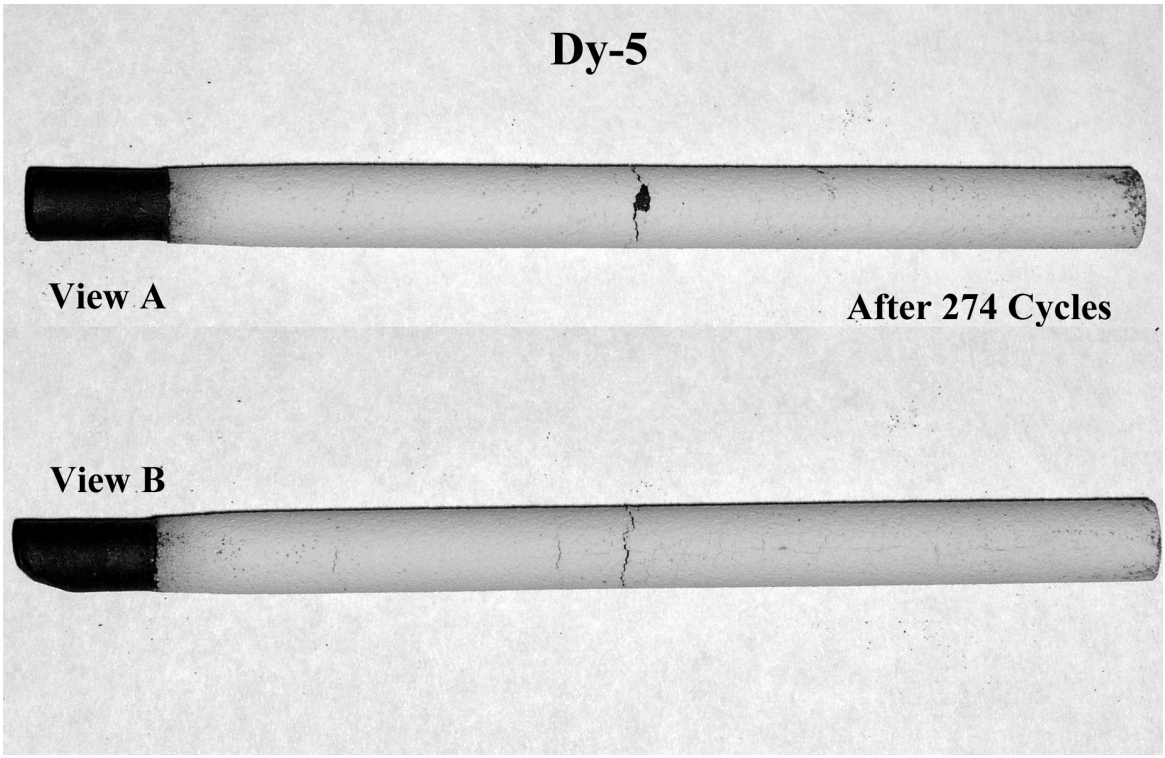
Dy-5
View A
After 274 Cycles
View B

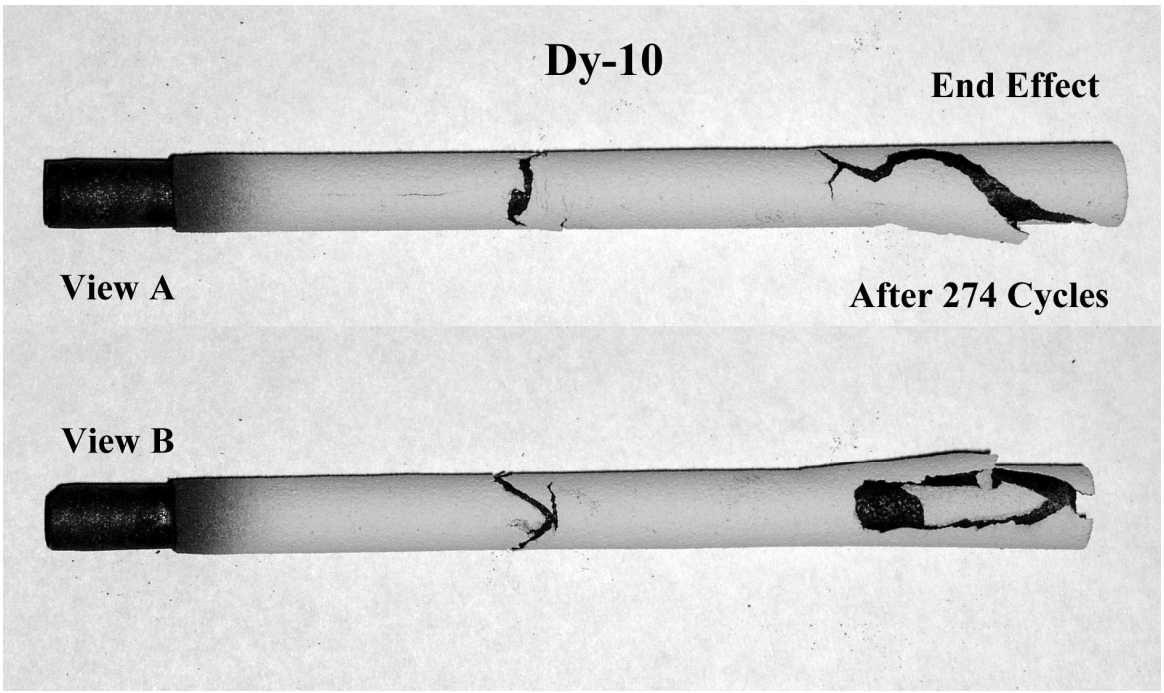
Dy-10
End Effect
View A
After 274 Cycles
View B

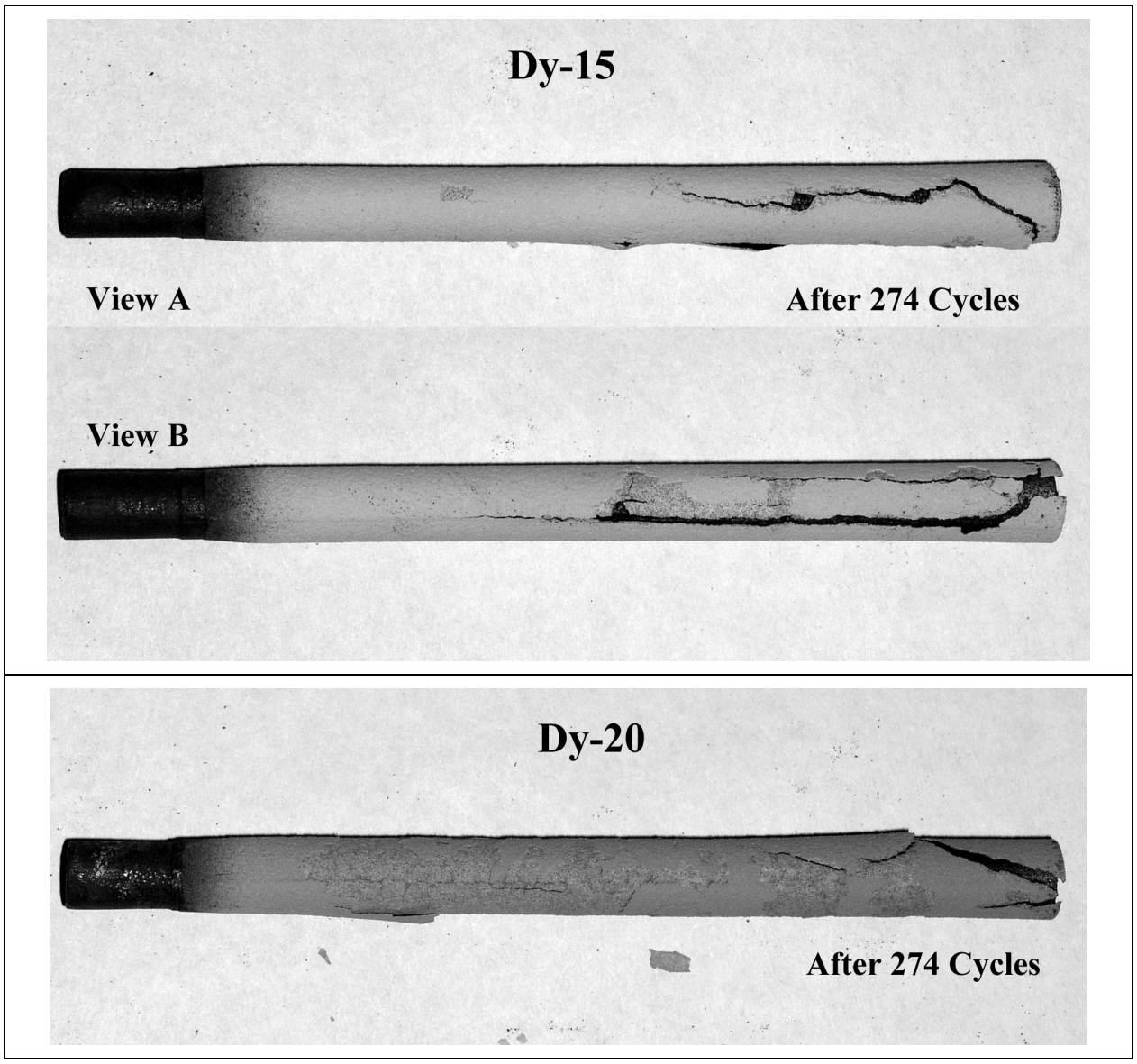

Figure 40: Thermal cycled rod specimens from 3rd trial (CMSX-11B substrate); 274 cycles, coating thickness ~200 μm

CHAPTER V – Conclusions and Recommendations for Future Work

The current study found that dysprosia-yttria-zirconia behaves similarly to other rare-earth doped zirconia (such as Gd, Nd, etc.) Thermal diffusivity, specific heat, porosity and density of APS 5YSZ and Dy-YSZ coatings were respectively measured by laser flash, DSC, image analysis, and XRD/Rietveld refinement. Coating thermal conductivities were then calculated using a simple equation. At 10-15 mol% of total dopant concentration, the reductions in thermal conductivity as compared to 5YSZ were about 19-22%, respectively. While the absolute values of calculated thermal conductivities were lower than other published data, the general trend was similar and a minimum was reached at about 10-15 mol% of total dopant concentration. A thermal conductivity model constructed from various published works was employed in an attempt to verify certain theories against experimental data. These theories included phonon heat conduction, scattering by point defects and grain boundaries, additional scattering by rounded pores and interlamellar cracks, as well as contributions from radiation effects. Utilizing parameters referenced from literature, the model output data was within range of experimental data by a factor of two. Lower than expected specific heat values and density for Dy-10 were probable causes of error. The components within the model were verified against literature data and were found to be relatively effective in making accurate predictions. Therefore, it can be concluded that trivalent dopants such as Dy stabilize the cubic phase of zirconia and generate oxygen vacancies with increasing dopant concentration. Indeed these vacancies could provide major contribution in the reduction of thermal conductivity to reach a minimum at about 10-15 mol% total dopant concentration. At higher concentrations it is believed that increase in thermal conductivity due to long range ordering of oxygen vacancies begin to overcome any further reduction, leading to an effective rise in thermal conductivity. Radiative contributions to thermal conductivity become significant at high temperatures such as 1200°C.

When APS coatings were thermally cycled between room temperature and 1100°C with residence time at 1085-1090°C for 22.8 or 29.1 hours, experimental data showed that there was a definite trend in sintering resistance. It appeared that increasing dysprosia content improved sintering resistance, where Dy-15 was 34% more resistant than 5YSZ. This would be consistent with theory whereby atoms with large atomic radii and mass assist in resisting sintering. However it was unresolved as to whether oxygen vacancies played a role. The thermal cycle experiment also revealed that the best coating performance belonged to Dy-5. In all trials, this

coating performed equally well or better than 5YSZ. Dy-15 and Dy-20 coatings were consistently prone to massive spallation, thus they would not be suitable for TBC applications.

The following recommendations are offered as further work to improve or expand upon the current study:

1. Revise coating chemistry matrix to include 5YSZ, 10YSZ, 15YSZ, 5Dy-5YSZ, and 10Dy-5YSZ. This setup would grant the ability to separate dopant atom and oxygen vacancy effects.
2. Increase thermal cycle high temperature limit to 1200°C.
3. Produce and measure more samples for specific heat and thermal diffusivity in order to improve current data set (e.g. 10 total data points per parameter and per material).
4. Consider measuring specific heat and thermal diffusivity at several temperature increments beyond room temperature, such as 400°C, 800°C, and 1100°C. This would offer new opportunities to verify theoretical model.
5. Utilize CO_2 laser flash equipment for thermal diffusivity measurements so that graphite coatings and related possible contamination in DSC are eliminated.
6. Measure free standing and post-cycle coating density by utilizing gas pycnometer and four-decimal digital scale instead of image analysis and Rietveld refinement.

REFERENCES

[1] A. H. Heuer and L. W. Hobbs, "Science and technology of zirconia", Columbus, Ohio : American Ceramic Society, 1981

[2] A. H. Heuer, "Science and Technology of Zirconia II", The American Ceramic Society, 1984

[3] S. Somiya, N. Yamamoto, H. Yanagida, "Science and technology of zirconia III", Westerville, Ohio : American Ceramic Society, 1988

[4] S. P. S. Badwal, M. J. Bannister, R. H. J. Hannink, "Science and Technology of Zirconia V", Lancaster, PA : Technomic Publishing Co., 1993

[5] J. R. Nicholls, "Advances in Coating Design for High-Performance Gas Turbines", MRS Bulletin, Vol. 28, No.9, 2003, pp. 659-670

[6] N. Q. Minh, "Ceramic Fuel Cells", Journal of the American Ceramic Society, Vol. 76, No.3, 1993, pp. 563-588

[7] D. Zhu, J. A. Nesbitt, T. R. McCue, C. A. Barrett, R. A. Miller, "Furnace Cyclic Behavior of Plasma-sprayed Zirconia-yttria and Multicomponent Rare Earth Oxide Doped Thermal Barrier Coatings", Ceramic Engineering and Science Proceedings, Vol. 23, No. 4, 2002, pp. 533-545

[8] D. Zhu and R. A. Miller, "Thermal Conductivity and Sintering Behavior of Advanced Thermal Barrier Coatings", Ceramic Engineering and Science Proceedings, Vol. 23, No.4, 2002, pp. 457-468

[9] J. Wu, X. Wei, N. P. Padture, P. G. Klemens, M. Gell, E. Garcia, P. Miranzo, M. I. Osendi, "Low-Thermal-Conductivity Rare-Earth Zirconates for Potential Thermal-Barrier-Coating Applications", Journal of the American Ceramic Society, Vol. 85, No. 12, 2002, pp. 3031-3035

[10] R. Gadow and M. Lischka, "Lanthanum Hexaaluminate – Novel Thermal Barrier Coatings for Gas Turbine Applications – Materials and Process Development", Surface and Coatings Technology, Vol. 151-152, 2002, pp. 392-399

[11] D. R. Clarke and C. G. Levi, "Materials design for the next generation thermal barrier coatings", Annual Review of Material Research, Vol. 33, 2003, pp. 383-417

[12] E. S. Lukin, "Modern High-Density Oxide Ceramics with Controlled Microstructure. Pt. 2. Substantiation of the Choice of Modifying Additives that Affect the Degree of Sintering", Refractories and Industrial Ceramics, Vol. 37, No.3-4, 1996, pp. 109-119

[13] K. W. Schlichting, N. P. Padture, P. G. Klemens, "Thermal conductivity of dense and porous yttria-stabilized zirconia", Journal of Materials Science, Vol. 36, 2001, pp. 3003-3010

[14] K. W. Schlichting, N. P. Padture, P. G. Klemens, "Thermal conductivity of ZrO_2 containing Y_2O_3: Effects of porosity", 25th International Thermal Conductivity Conference (Michigan), 1999, pp. 162-170

[15] S. Raghavan, H. Wang, R. B. Dinwiddie, W. D. Porter, M. J. Mayo, "The effect of grain size, porosity and yttria content on the thermal conductivity of nanocrystalline zirconia", Scripta Materialia, Vol. 39, No. 8, 1998, pp. 1119-1125

[16] J. F. Bisson, D. Fournier, M. Poulain, O. Lavigne, R. Mévrel, "Thermal conductivity of yttria-zirconia single crystals, determined with spatially resolved infrared thermography", Journal of the American Ceramic Society, Vol. 83, No. 8, 2000, pp. 1993-1998

[17] R. Mévrel, J. C. Laizet, A. Azzopardi, B. Leclercq, M. Poulain, O. Lavigne, D. Demange, "Thermal diffusivity and conductivity of $Zr_{1-x}Y_xO_{2-x/2}$ (x=0.084 and 0.179) single crystals", Journal of the European Ceramic Society, Vol. 24, 2004, pp. 3081-3089

[18] G. Suresh, G. Seenivasan, M. V. Krishnaiah, P. S. Murti, "Investigation of the Thermal Conductivity of Selected Compounds of Gadolinium and Lanthanum", Journal of Nuclear Materials, Vol. 249, 1997, pp. 259-261

[19] H. Lehmann, D. Pitzer, G. Pracht, R. Vassen, D. Stover, "Thermal Conductivity and Thermal Expansion Coefficients of the Lanthanum Rare-Earth-Element Zirconate System", Journal of the American Ceramic Society, Vol. 86, No.8, 2003, pp. 1338-1344

[20] R. Vassen, X. Cao, F. Tietz, D. Basu, D. Stöver, "Zirconiates as new materials for thermal barrier coatings", Journal of the American Ceramic Society, Vol. 83, No. 8, 2000, pp. 2023-2028

[21] J. Wu, N. P. Padture, P. G. Klemens, M. Gell, E. Garcia, P. Miranzo, and M. I. Osendi, "Thermal conductivity of ceramics in the ZrO_2-$GdO_{1.5}$ system", J. Mater. Res. Vol. 17, No. 12, Dec. 2002, pp. 3193-3200

[22] J. R. Nicholls, K. J. Lawson, A. Johnstone, and D. S. Rickerby, "Methods to reduce the thermal conductivity of EB-PVD TBCs", Surface and Coatings Technology, Vol. 151-152, 2002, pp. 383-391

[23] Rolls-Royce PLC, "Metallic article having a thermal barrier coating and a method of application thereof", United States Patent 6,025,078, February 15, 2000

[24] R. Siegel and C. M. Spuckler, "Analysis of thermal radiation effects on temperatures in turbine engine thermal barrier coatings", Materials Science and Engineering A245, 1998, pp. 150-159

[25] A. A. Kulkarni, S. Sampath, A. Goland, H. Herman, "Porosity-thermal conductivity relationships in plasma sprayed zirconia coatings", Proceedings of the 1st International Thermal Spray Conference, 2000, Montreal, Quebec, Canada, pp. 1061-1066

[26] R. Brandt, L. Pawlowski, G. Neuer, P. Fauchais, "Specific heat and thermal conductivity of plasma sprayed yttria-stabilized zirconia and NiAl, NiCr, NiCrAl, NiCrAlY, NiCoCrAlY coatings", High Temperatures-High Pressures, Vol. 18, 1986, pp. 65-77

[27] Z. Wang, A. Kulkarni, S. Deshpande, T. Nakamura, H. Herman, "Effects of pores and interfaces on effective properties of plasma sprayed zirconia coatings", Acta Materialia, Vol. 51, 2003, pp. 5319-5334

[28] C. Friedrich, R. Gadow, T. Schirmer, Proceedings of the 1st International Thermal Spray Conference, 2000, pp. 1219-1226

[29] R. Hamacha, P. Fauchais, F. Nardou, "Influence of Dopant on the Thermal Properties of Two Plasma-Sprayed Zirconia Coatings. I. Relationship Between Powder Characteristics and Coating Properties", Journal of Thermal Spray Technology, Vol. 5, No.4, 1996, pp. 431-438

[30] M. Matsumoto, K. Aoyama, H. Matsubara, K. Takayama, T. Banno, Y. Kagiya, Y. Sugita, "Thermal conductivity and phase stability of plasma sprayed ZrO_2-Y_2O_3-La_2O_3 coatings", Surface & Coatings Technology, Vol. 194, 2005, pp. 31-35

[31] F. A. Akopov, "Influence of Thermal Ageing on the Structure and Electrophysical Properties of Ceramic Materials of the ZrO_2-Y_2O_3-Nd_2O_3 System", Inorganic Materials, Vol. 17, No.10, 1981, pp. 1405-1407

[32] P. G. Klemens and M. Gell, "Thermal conductivity of thermal barrier coatings", Material Science and Engineering A245, 1998, pp. 143-149

[33] P. G. Klemens, "Theory of Thermal Conduction in Thin Ceramic Films", International Journal of Thermophysics, Vol. 22, No. 1, 2001, pp. 265-275

[34] P. G. Klemens, "Thermal conductivity of zirconia", 23rd International Thermal Conductivity Conference (Nashville), 1996, pp. 209-219

[35] W. M. Rogers and R. L. Powell, "Tables of Transport Integrals", NBS Circular 595, 1958

[36] J.C. Maxwell, "A Treatise on Electricity and Magnetism", Clarendon Press, Oxford, UK, 1904

[37] H. Hatta and M. Taya, "Effective thermal conductivity of a misoriented short fibre composite", Journal of Applied Physics, Vol. 58, No. 7, Oct. 1985, pp. 2478-2486

[38] M. Raudsepp and E. Pani, "Application of Rietveld analysis to environmental mineralogy", Mineralogical Association of Canada, Short Course Series, Vol. 31, Chap. 8, 2003, pp. 165-180

[39] K. Shinzato and T. Baba, "A laser flash apparatus for thermal diffusivity and specific heat capacity measurements", Journal of Thermal Analysis and Calorimetry, Vol. 64, 2001, pp. 413-422

[40] G. Penco, D. Barni, P. Michelato, C. Pagani, "Thermal properties measurements using laser flash technique at cryogenic temperature", Proceedings of the 2001 Particle Accelerator Conference Chicago, pp. 1231-1233

[41] W. J. Parker, R. J. Jenkins, C. P. Butler, G. L. Abbot, "Flash method of determining thermal diffusivity, heat capacity and thermal conductivity", Journal of Applied Physics, Vol. 32, 1964, pp. 1679-1684

[42] P. Simon and Z. Cibulkova, "Measurement of heat capacity by differential scanning calorimetry", Proceedings of the Thermophysical Society – Working Group of the Slovak Physical Society, 2002, pp. 77-80

[43] G. Bertrand, P. Roy, C. Filiatre, C. Coddet, "Spray-dried ceramic powders: A quantitative correlation between slurry characteristics and shapes of the granules", Chemical Engineering Science, Vol. 60, 2005, pp. 95-102

[44] P. Roy, G. Bertrand, C. Coddet, "Spray drying and sintering of zirconia based hollow powders", Powder Technology, Vol. 157, 2005, pp. 20-26

[45] Y. Du, Z. Jin, P. Huang, "Thermodynamic assessment of the ZrO_2-$YO_{1.5}$ system", Journal of the American Ceramic Society, Vol. 74, No. 7, 1991, pp. 1569-1577

[46] J. I. Eldridge, C. M. Spuckler, K. W. Street, J. R. Markham, "Infrared radiative properties of yttria-stabilized zirconia thermal barrier coatings", Ceramic Engineering and Science Proceedings, Vol. 23, No. 4, 2002, pp. 417-430

[47] H. G. Scott, "Phase relationships in the zirconia-yttria system", Journal of Materials Science, Vol. 10, No. 9, 1975, pp. 1527-1535

[48] C. Pascual and P. Duran, "Phase relations and ordering in the dysprosia-zirconia system", Journal of Materials Science, Vol. 15, No. 7, 1980, pp. 1701-1708

[49] S. Raghavan, H. Wang, W. D. Porter, R. B. Dinwiddie, M. J. Mayo, "Thermal properties of zirconia co-doped with trivalent and pentavalent oxides", Acta Materialia, Vol. 49, 2001, pp. 169-179

[50] D. Schwingle, R. Taylor, T. Haubold, J. Wigren, C. Gaulco, F. Ladru, E. Lugscheider, V. Gourlaouen, "Thermophysical and mechanical properties of PYZ thick thermal barrier coatings", Proceedings of the 15th International Thermal Spray Conference, 25-29 May 1998, Nice, France, pp. 623-628

[51] R. E. Taylor, "Thermal conductivity determinations of thermal barrier coatings", Materials Science and Engineering, Vol. A245, 1998, pp. 160-167

[52] J. R. Brandon and R. Taylor, "Thermal properties of ceria and yttria partially stabilized zirconia thermal barrier coatings", Surface & Coatings Technology, Vol. 39-40, 1989, pp. 143-151

[53] J. F. Jue, R. Nageswaran, A. Virkar, "Characterization of yttria and rare earth-oxide doped zirconia materials for high temperature applications", Elevated Temperature Coatings: Science and Technology I, 1995, pp. 125-134